A Type of Novel Energy Harvesting Device

Jiewen Deng

St Anne's College

A dissertation submitted for the degree of MSc by Research
in the Department of Engineering Science
at the University of Oxford
Hilary Term, 2013

To my parents.

ABSTRACT

A Type of Novel Energy Harvesting Device

Jiewen Deng, St Anne's College, Oxford
A dissertation submitted for the degree of MSc by Research
in the Department of Engineering Science at University of Oxford
Hilary Term, 2013

Pervasive networks of wireless sensors and communication nodes have been developed during past decades and most of them are powered by fixed-energy sources, e.g., wiring power and batteries. However, these traditional energy sources are impractical for powering wireless devices due to their inherent limitations, e.g., the high setup cost of wiring power and the finite life span of batteries. In view of these facts, more attentions have been drawn on vibration energy sources existing in ambient environment where sensors operate. Dozens of different types of vibration energy scavenging devices have been developed, which are mainly consisted of mechanical systems coupled with transduction mechanisms. The linear mechanical system has been used in most of existing vibration generators. The main drawback of such system is that it has a rather narrow bandwidth, meaning that the device can only effectively harvest vibration energy when the resonance frequency of the system coincides with the excitation frequency. Various methods have been proposed recently to overcome the drawback including utilising mechanical systems with non-linear mechanisms in order to increase the bandwidth of vibration energy scavenging devices.

The dissertation is intended to find a practically effective non-linear mechanical system with desirable dynamic behaviours for vibration energy scavenging devices. To do so, we first examined three non-linear mechanisms numerically to find the most desirable one based on the corresponding typical mechanical systems. The Numerical Simulation (NS) method built in Matlab has been used to explore the static and dynamic characteristics of these systems with hardening and softening mechanisms firstly. It has been found that these systems with hardening and softening mechanisms whose frequency response curves lean sideways can expand the operation bandwidths.

However, the former has comparatively low output displacements whereas unstable dynamic responses are often associated with the latter after the forcing amplitude exceeds the critical value. To overcome the new hurdles, we have examined a typical mechanical system with a snap-through mechanism using the NS method. It exhibits the characteristics of a system with a softening mechanism when the forcing amplitude is comparatively small, and those of a system with a hardening mechanism when the forcing amplitude increases. Despite the advantages of the typical system, it has been found to be impossible to attach the transduction mechanism to the typical system in order to harvest power.

This has led to the development of a new mechanical system which consists of a central shim with four identical beams bonded by two blocks and magnetic buttons. By numerical simulation and experiments, we are able to show that the new design can be a system with either hardening mechanism or snap-through mechanism with a suitable selection of the column height. Due to the magnetic force from the magnetic buttons, the new design with a snap-through mechanism shows significant advantages in expanding the bandwidth and raising the dynamic displacement. However, the design leads to distortion of the two blocks in vibration, which makes the piezoelectric transduction mechanism unable to be coupled with it efficiently. As a result an improved design has been proposed in which a cross shim is used to replace the rectangular shim in the first design, which can be coupled with the piezoelectric transduction mechanism effectively to form a complete piezoelectric non-linear vibration energy scavenging device. Based on the results of numerical simulation and experiments, it is shown that the new device with a snap-through mechanism can generate enough voltage and power to power an existing wireless senor and has a wide off-resonance frequency bandwidth. Therefore, the new device with a snap-through mechanism could be an alternative design to overcome the drawbacks of existing linear and non-linear vibration generators in certain conditions.

ACKNOWLEGEMENTS

The work described in this dissertation was conducted by the author in the Department of Engineering Science at the University of Oxford. I received great help from a lot of people during my time there, without whom I would not have completed my study.

Most and foremost, I would like to express my deepest gratitude to my supervisor, Dr. Zhong You, for his guidance, patience and encouragement throughout the period of my study at University of Oxford. His broad knowledge in the area of vibration energy scavenging, unique views to different problems, and sparkling imaginations benefited me enormously during every meeting with him.

My special appreciation also goes to Prof. Tony Blakeborough, meetings with whom greatly broadened and enhanced my understanding of the area of structural dynamics, which contributed a lot to my research project.

I would also like to thank Dr. Malcom McCulloch in the Department of Engineering Science and Mr Xin You for their help on working principles of piezoelectricity, Dr. Rob Roach for his help on supplying the experiment equipments, Mr. Bob Sawala for his help on constructing the concrete plate used in experiments, Mr. Clive Baker for his suggestions on various machining related issues, and the Workshop in the Department of Engineering Science for machining a lot of moulds for me.

I am thankful to my colleagues in the Civil Engineering Group, particularly Dr. Xiang Zhou, Dr. Weina Wu, Dr. Jiayao Ma, and my friends, Dr Xu Song, Mr Mengyin Xie and Mr Xiao Shu, to whom provided a fun and conductive place to study and live.

I would also like to thank St Anne’s College and the Department of Engineering Science for financially supporting me to attend the SPIE conference in US.

Finally but most importantly, I would like to dedicate this work to my parents and the whole family for their tremendous support and encouragement, without whom this dissertation may have not be possible.

CONTENTS

ABSTRACT.......... ii

ACKNOWLEGEMENTS.......... iv

CONTENTS.......... v

LIST OF FIGURES.......... viii

LIST OF TABLES.......... xi

NOTATIONS.......... xii

CHAPTER 1 INTRODUCTION.......... 1

- 1.1 Powering Wireless Sensors and Communication Nodes.......... 1
- 1.2 Energy Scavenging Technologies.......... 2
  - 1.2.1 Solar Energy.......... 2
  - 1.2.2 Vibration Energy.......... 3
  - 1.2.3 Acoustic Noise.......... 3
  - 1.2.4 Temperature Variations.......... 3
- 1.3 Objective.......... 4
- 1.4 Layout of Dissertation.......... 5

CHAPTER 2 LITERATURE REVIEW.......... 7

- 2.1 Vibration Sources.......... 7
- 2.2 Generic Vibration-to-Electricity Conversion Model.......... 7
- 2.3 Transduction Mechanisms.......... 12
  - 2.3.1 Electromagnetic Transduction Mechanism.......... 12
  - 2.3.2 Electrostatic Transduction Mechanism.......... 13

2.3.3 Piezoelectric Transduction Mechanism 14

2.3.4 Comparison of Energy Densities of Transduction Mechanisms.............17

2.3.5 Summary of Transduction Mechanisms 20

2.4 Existing Piezoelectric Vibration Energy Scavenging Devices 21

2.4.1 Linear Piezoelectric Vibration Energy Scavenging Devices 22

2.4.2 Limitations of Existing Linear Piezoelectric Vibration Energy Scavenging Devices 23

2.4.3 Improvements to Linear Piezoelectric Vibration Energy Scavenging Devices..24

CHAPTER 3 NON-LINEAR MECHANISMS 26

3.1 Hardening and Softening Mechanisms 26

3.1.1 Typical mechanical system with hardening mechanism..........................26

3.1.2 Typical mechanical system with softening mechanism...........................29

3.1.3 Mathematical Modeling 30

3.1.4 Static Analysis 32

3.1.5 Dynamic Analysis..33

3.1.6 Specific Dynamic Behaviours..37

3.1.7 Comparison among the Linear System and Systems with Hardening and Softening Mechanisms...38

3.1.8 Limitations 39

3.2 Snap-through mechanism...44

3.2.1 Typical mechanical system with snap-through mechanism.....................44

3.2.2 Statics Analysis...46

3.2.3 Dynamic Analysis...48

3.2.4 Practical Constraints of the Typical Mechanical System 54

3.3 Summary 55

CHAPTER 4 NEW NON-LINEAR MECHANICAL SYSTEMS........................66

4.1 Design I........................66

4.1.1 Model........................66

4.1.2 Static Analysis........................68

4.1.3 Dynamic Analysis and Experiments........................74

4.1.4 Advantages of the Devices and Practical Constraints........................81

4.2 Design II........................83

4.2.1 Model........................83

4.2.2 The Device........................84

4.2.3 Static Analysis........................85

4.2.4 The Coupling Model........................87

4.2.5 Dynamic Analysis and Experiments........................91

4.3 Summary........................99

CHAPTER 5 CONCLUSIONS AND FUTURE WORK........................103

5.1 Conclusions........................103

5.2 Future Work........................108

5.2.1 Investigations of the Effect of the Chaotic Response on Vibration Energy Scavenging........................108

5.2.2 Physical Modeling and Experiments........................109

5.2.3 Optimizations........................109

REFERENCE........................110

LIST OF FIGURES

2.1 Generic vibration-to-electricity model....................8

2.2 Power output vs. mechanical and electrical damping ratios when $m=0.05$ Kg, $\omega_n=\omega=100$ Hz and $A=5$ m/s^2 11

2.3 Power output vs. input frequency and electrical damping ratio when $m=0.05$ Kg, $\omega_n=100$ Hz, $A=5$ m/s^2 and $\varsigma_e=\varsigma_m$....................11

2.4 Power output vs. resonant and input frequencies when $m=0.05$ Kg, $A=5$ m/s^2 and $\varsigma_e=\varsigma_m=0.05$ 12

2.5 Power output vs. input frequency and mass of the system when $A=5$ m/s^2, $\omega_n=100$ Hz and $\varsigma_e=\varsigma_m=0.05$ 12

2.6 Illustration of 33 mode and 31 mode working models of piezoelectric materials. 20

2.7 (a) Bimorph cantilever beam generator by Roundy and Wright [17], (b) tapered cantilever beam generator by Glynne-Jones *et al.* [22]. 23

2.8 (a) Resonance tuning generator with compressive axial load by Leland and Wright [27], (b) resonance tuning generator with permanent magnets by Challa *et al.* [28],and (c) Smart Sand with fixed-fixed beams by Marinkovic and Koser [29] 25

3.1 (a) A fixed-fixed beam T1; (b) its deformed shape when F_B acts on its right end. 26

3.2 A pendulum, where m is the mass, L_P is the length of the rod and θ is the inclination of the rod....................29

3.3 (a) Force vs. deflection and (b) stiffness vs. deflection of systems with hardening mechanism with $\alpha_1=0.0025$ (blue), $\alpha_1=0.005$ (green) and $\alpha_1=0.0075$ (red).......33

3.4 (a) Force vs. deflection and (b) stiffness vs. deflection of systems with softening mechanism with $\alpha_1=0.0025$ (blue), $\alpha_1=0.005$ (green) and $\alpha_1=0.0075$ (red).........33

3.5 FRCs of systems with: (a) hardening mechanism, and (b) softening mechanism with coefficients' set 1 (red), set 2 (blue) and set 3 (green) as shown in Table 3.1. 35

3.6 FRCs of systems with: (a) hardening mechanism, and (b) softening mechanism with coefficients' set 4 (red), set 5 (blue) and set 6 (green) as shown in Table 3.1. 36

3.7 FRCs of systems with: (a) hardening mechanism, and (b) softening mechanism with coefficients' set 7 (red), set 8 (blue) and set 9 (green) as shown in Table 3.1. 37

3.8 A typical FRC of the system with a hardening mechanism....................38

3.9 FRCs comparison of the linear system – red, systems with hardening (green), and softening (blue) mechanisms for $\varsigma = 0.012$, $\alpha = 0.005$ and $\hat{F} = 0.125$ 39

3.10 Potential energy-deflection of the system with softening mechanism with $\varsigma = 0.012$ and $\alpha = 0.005$, where the grey areas stand for the unstable regions 44

3.11 T3, where k_S is stiffness of the spring, y_S the vertical deflection from the reference point Y_{ref} 46

3.12 (a) Force vs. deflection and (b) stiffness vs. deflection of $T3_1$ (blue), $T3_2$ (green) and $T3_3$ (red). 48

3.13 Potential energy vs. deflection curves: (a) $T3_1$, (b) $T3_2$ and (c) $T3_3$...................50

3.14 FRCs of $T3_1$ (blue) and $T3_2$ (green) when $\hat{F} = 0.05$. (a) $\varsigma = 0.04$, (b) $\varsigma = 0.06$ and (c) $\varsigma = 0.08$ 57

3.15 FRCs of $T3_1$ (blue) and $T3_2$ (green) when $\hat{F} = 0.125$. (a) $\varsigma = 0.04$, (b) $\varsigma = 0.06$ and (c) $\varsigma = 0.08$ 58

3.16 FRCs of $T3_1$ (blue) and $T3_2$ (green) when $\hat{F} = 0.2$. (a) $\varsigma = 0.04$, (b) $\varsigma = 0.06$ and (c) $\varsigma = 0.08$ 59

3.17 Time-based displacement responses (1st column) and the phase diagrams (2nd column) of $T3_1$ when $\hat{F} = 0.05$ and $\varsigma = 0.06$. (a, b) $\Omega = 0.5$, (c, d) $\Omega = 0.9$, (e, f) $\Omega = 1$ and (g, h) $\Omega = 1.5$. 60

3.18 Time-based displacement responses (1st column) and the phase diagrams (2nd column) of $T3_1$ when $\hat{F} = 0.125$ and $\varsigma = 0.06$. (a, b) $\Omega = 0.5$, (c, d) $\Omega = 0.9$, (e, f) $\Omega = 1$ and (g, h) $\Omega = 1.5$. 61

3.19 Time-based displacement responses (1st column) and the phase diagrams (2nd column) of $T3_1$ when $\hat{F} = 0.2$ and $\varsigma = 0.06$. (a, b) $\Omega = 0.5$, (c, d) $\Omega = 0.9$, (e, f) $\Omega = 1$ and (g, h) $\Omega = 1.5$. 62

3.20 Time-based displacement responses (1st column) and the phase diagrams (2nd column) of $T3_2$ when $\hat{F} = 0.05$ and $\varsigma = 0.06$. (a, b) $\Omega = 0.5$, (c, d) $\Omega = 0.7$, (e, f) $\Omega = 0.8$ and (g, h) $\Omega = 1.5$ 63

3.21 Time-based displacement responses (1st column) and the phase diagrams (2nd column) of $T3_2$ when $\hat{F} = 0.125$ and $\varsigma = 0.06$. (a, b) $\Omega = 0.5$, (c, d) $\Omega = 0.7$, (e, f) $\Omega = 0.8$ and (g, h) $\Omega = 1.5$ 64

3.22 Time-based displacement responses (1st column) and the phase diagrams (2nd column) of $T3_2$ when $\hat{F} = 0.2$ and $\varsigma = 0.06$. (a, b) $\Omega = 0.5$, (c, d) $\Omega = 0.7$, (e, f) $\Omega = 0.8$ and (g, h) $\Omega = 1.5$ 65

4.1 The 3D model of N1: (a) isometric view of N1 and (b) arrangement of magnets. 67

4.2 Design of (a) the central shim, and (b) the top and bottom alloy blocks forming the lumped mass in N1. Unit: mm. 67

4.3 Force vs. deflection diagrams of the doubly clamped beam. (a) Eq. (4.1) and Abaqus simulation, (b) Eq. (4.1), Eq. (4.2) and Eq. (4.3). In the diagrams, Eq. (4.1) (red), Eq. (4.2) (blue), Eq. (4.3) (green), and Abaqus FEA (black). 69

4.4 The simplified model of N1 70

4.5 Force vs. distance diagrams of two attractive magnets basing on Eq. (4.5) (red) and FEMM (balck). 71

4.6 (a) Force vs. deflection and (b) stiffness vs. deflection of $N1_1$ (red), and $N1_2$ (green). 74

4.7 Experimental apparatus 75

4.8 FRCs of $N1_1$ (red), and $N1_2$ (green). (a) $A_c = 1$ m/s^2, (b) $A_c = 5$ m/s^2. 77

4.9 FRCs of: (a, b) $N1_1$ and (c, d) $N1_2$, when $A_c = 1$ m/s^2 for a and c, $A_c = 5$ m/s^2 for b and d. Simulation data (blue) and experiment data (red). 79

4.10 Spartial displacement of N1 with $z = 2$ mm by Abaqus: (a) x-direction, (b) y-dirction and (c) z-dirction. 81

4.11 First six eigenmodes of N1 free of magnetic force by Abaqus 82

4.12 The 3D model of N2: (a) isometric view of N2 and (b) arrangement of magnets. 83

4.13 Design of (a) the central shim, and (b) the top and bottom alloy blocks forming the lumped mass in N2. Unit: mm. 84

4.14 Arrangement of the beryllium copper doubly clamped beam, conductive glue and piezoelectric plate. Unit: mm. 84

4.15 Simulations of strain along the piezoelectric plate. $z = 0.5$ mm (red), $z = 1$ mm (green) and $z = 2$ mm (blue) 86

4.16 (a) Force vs. deflection and (b) stiffness vs. deflection of ND_1 (red) and ND_2 (green). 86

4.17 Piezoelectric mechanical and electrical domains coupling model 87

4.18 Experimental apparatus 92

4.19 Voltage vs. frequency of ND_1: (a) $A_c = 1$ m/s^2, (b) $A_c = 5$ m/s^2 and (c) $A_c = 9$ m/s^2. 97

4.20 Voltage and power output of ND_1 with various load resistances when: (a, b) 99

and $\omega = 45$ Hz, and (c, d) $A_c = 9$ m/s^2 and $\omega = 43$ Hz. 99

LIST OF TABLES

1.1 Power density comparison of energy scavenging and energy storage technologies. 4

2.1 List of vibration sources with the peak acceleration and corresponding frequency. 7

2.2 Coefficients of common piezoelectric materials..20

2.3 Summary of the comparison of the three transduction mechanisms. 21

3.1 Coefficients' sets used by the dynamic simulation of systems with hardening and softening mechanisms..34

3.2 Displacement values at the critical points and cross points of $T3_1$, $T3_2$ and $T3_3$. 50

4.1 Physical properties of materials...68

4.2 Displacement values of the critical point and cross point of $N1_1$. 74

4.3 Dimensional parameters and physical and electrical properties of the selected piezoelectric plate 85

NOTATIONS

Roman Symbols

A	Acceleration of input vibration
A_1	Amplitude of the first harmonic term
$A_{1\max}$	Maximum magnitude of the amplitude of the first harmonic term
A_B	Cross-section area of a fixed-fixed beam
A_c	Constant acceleration
A_{DCB}	Cross-section area of a doubly clamped beam
A_n	Amplitude of harmonic terms
A_{T1}	$\dfrac{12E_B I_B}{L_B^3}$
A_{T2}	mg
B_{mag}	Strength of a magnetic field
B_r	Residual flux density
B_{T1}	$\dfrac{A_B E_B \pi}{16L_B^3}$
B_{T2}	$\dfrac{mg}{6}$
c	Damping coefficient
c_e	Electrically induced damping coefficient
c_m	Mechanical damping coefficient
C_P	Piezoelectric capacitance
C_{sta}	Capacitance
$[d]$	Three by six matrix of piezoelectric strain coefficients
$\{D\}$	Three-dimensional electric displacement vector

D_3	Electric displacement in 31 mode
$d_{31,33}$	Piezoelectric strain coefficient
d_{I1}	Thickness of the beryllium copper shim in the first new design
d_{I2}	Depth of the aluminum alloy block in the first new design
d_{I3}	Thickness of the magnetic buttons in the first new design
d_{I3R}	Thickness of ring magnets
d_{I4}	Distance between two magnets when the first new design is at rest
d_{II1}	Thickness of the beryllium copper shim in the second new design
d_{II2}	Depth of the aluminum alloy block in the second new design
d_{II3}	Thickness of the magnetic buttons in the second new design
d_{piezo}	Piezoelectric strain coefficient for general applications
d_{sta}	Distance between two plates in a capacitor
$\left[d^t\right]$	Six by three matrix converse piezoelectric effect
d_{TM}	Distance between two magnets
$d_{TM1,TM2}$	Distance between two magnets when the first new design is deflected
$\{E\}$	Three-dimensional electric field strength vector
E_3	Electric field strength in 31 mode
E_b	Young's modulus of a beryllium copper shim
E_B	Young's modulus of a fixed-fixed beam
E_{piezo}	Electric field strength in a piezoelectric material for general applications
E_{PS}	Elastic potential energy of the typical system with snap-through mechanism
$\widehat{E_S}$	Non-dimensional potential energy of the typical system with snap-through mechanism

$\widehat{E_{soft}}$	Non-dimensional potential energy of the typical system with softening mechanism
E_{sta}	Electric field strength in a capacitive device
F	Excitation force
$\widehat{F}$	Non-dimensional excitation force
F_B	Vertical load at one of the ends of a fixed-fixed beam
F_{EDCB}	Restoring force of a doubly clamped beam
F_{EDCB1}	Restoring force of a doubly clamped beam due to tension
F_{EDCB2}	Restoring force of a doubly clamped beam due to bending
F_{IE}	Restoring force of four doubly clamped beams
F_{IM}	Resultant magnetic force in the first new design
F_{IN}	Input force in a piezoelectric coupling model
F_p	Feedback force in a piezoelectric coupling model
$\widehat{F_R}$	Non-dimensional restoring force of a Duffing oscillator
$\widehat{F_{R2}}$	Non-dimensional restoring force dominated by negative stiffness
F_{RES}	Resultant force in the first new design
F_S	Restoring force in the typical system with snap-through mechanism
$\widehat{F_S}$	Non-dimensional restoring force in the typical system with snap-through mechanism
F_{TVACM}	Magnetic force between two vertically aligned cylindrical magnets
$F_{TVACM1,TVACM2}$	Attractive magnetic force in the first new design
$g_{31,33}$	Piezoelectric voltage constant
h_{column}	Height of a column
I_B	Second moment area of a fixed-fixed beam
I_{DCB}	Second moment area of a doubly clamped beam

k	Spring constant
$\widehat{K}$	Non-dimensional stiffness of a Duffing oscillator
k_1	Linear spring constant
k_2	Non-linear spring constant
$k_{31,33}$	Electromechanical coupling factor
$k_{31-effective}$	Effective electromechanical coupling factor
k_S	Stiffness of springs in the typical system with snap-through mechanism
$\widehat{K_S}$	Non-dimensional stiffness of springs in the typical system with snap-through mechanism
$k_{stiffness}\left(z\right)$	Spring constant in a piezoelectric coupling model
l_b	Horizontal from the left end of a fixed-fixed beam
L_B	Length of a fixed-fixed beam
l_{column}	Length of a column
L_D	Length of a deflected fixed-fixed beam
L_{DCB}	Length of a doubly clamped beam
l_{mag}	Length of one coil
L_P	Length of the rod in a pendulum
l_{piezo}	Length of a piezoelectric plate
L_S	Original length of a spring in the typical system with snap-through mechanism
L_{SH}	Horizontal length of a spring in the typical system with snap-through mechanism
l_{sta}	Length of the plate in a capacitor
m	Mass
M_B	Bending moment of a fixed-fixed beam
N	Positive integer and ≥ 1
n_c	Number of oscillation cycles

N_{mag}	Number of turns in a coil
n_{piezo}	Number of piezoelectric plates
P_e	Electric power
$P_{\max 1, \max 2}$	Maximum potential energy f the typical system with softening mechanism
P_{piezo}	Power transferred to a external resistance load
$P_{S-A, S-B, S-C}$	Equilibrium point of the typical system with snap-through mechanism
P_{S-CRI}	Critical point where the typical system with snap-through mechanism becomes unstable
P_{S-CRO}	Cross point where the typical system with snap-through mechanism crosses the potential energy well
Q_{sta}	Charge on a capacitor
R_L	External load resistance in a piezoelectric coupling model
R_{opt}	Optimal load resistance
$\{S\}$	Six-dimensional strain vector
S_1	Strain in 31 mode
s_{11}^E	Compliance in 31 mode
$\left[s^E\right]$	Six by six compliance matrix evaluated at constant electric field
t	Oscillation time
$\{T\}$	Six-dimensional stress vector
T_1	Stress in 31 mode
t_{piezo}	Thickness of a piezoelectric plate
u_{mag}	Energy density of an electromagnetic converter
u_{piezo}	Energy density of a piezoelectric material
u_{sta}	Energy density of a capacitive device
v_{mag}	Velocity of relative motions

V_{mag}	Open circuit voltage across a coil
V_{peak}	Peak value of half wave in AC voltage
V_{rms}	Root-mean-square voltage
V_{sta}	Voltage generated by a capacitor
w_{column}	Width of a column
w_{piezo}	Width of a piezoelectric plate
w_{sta}	Width of the plate in a capacitor
x, $x^{'}$, $x^{''}$	Non-dimensional relative displacement, velocity and acceleration
$\left\|x_{\max 1}\right\|$	Maximum displacement when the typical system with softening mechanism keeps stable
$\left\|x_{\max 2}\right\|$	Maximum displacement when the typical system with softening mechanism increases infinitely
$x_{S-A,S-B,S-C}$	Corresponding displacement of equilibrium points of the typical system with snap-through mechanism
$\left\|x_{S-CRI-ST}\right\|$	Displacement where stiffness becomes negative
$\left\|x_{S-CRI-1,S-CRI-2}\right\|$	Displacement of critical points of the typical system with snap-through mechanism
$\left\|x_{S-CRO-1,S-CRO-2}\right\|$	Displacement of cross points of the typical system with snap-through mechanism
x_S	Non-dimensional displacement of the typical system with snap-through mechanism
y	Excitation displacement
Y	Maximum excitation displacement
y_b	Shape of a fixed-fixed beam
Y_{piezo}	Young’s modulus of a piezoelectric material
Y_{ref}	Reference point in the typical system with snap-through mechanism
y_s	Vertical deflection from the reference point of the typical system with snap-through mechanism

z , $\dot{z}$, $\ddot{z}$	Relative displacement, velocity and acceleration
z_0	Characteristic length of a non-linear system
$\left\|z_{N1-CRI-1,N1-CRI-2}\right\|$	Displacement of critical points of the first new design
$\left\|z_{N1-CRO-1,N1-CRO-2}\right\|$	Displacement of cross points of the first new design

Greek Symbols

α	Non-dimensional non-linear spring constant
$\alpha_{1,2,3}$	Non-dimensional non-linear spring constant
δ_{piezo}	Strain in a piezoelectric material for general applications
Δ	Real root
$\left[\varepsilon^T\right]$	Three by three dielectric constant matrix evaluated at constant stress
ε_{piezo}	Dielectric constant in a piezoelectric material for general applications
ε_{sta}	Dielectric constant between two plates in a capacitor
ε_0	Dielectric constant of free space, 8.85×10^{-15} F/m
ε_{33}^T	Dielectric constant in 31 mode
$\varepsilon_{33}^T/\varepsilon_0$	Relative permittivity
ς	Non-dimensional damping ratio
ς_e	Electrically induced damping ratio
ς_m	Mechanical damping ratio
ς_T	Overall damping ratio
θ	Inclination of the rod in a pendulum
θ_n	Phase angle of harmonic terms
θ_1	Phase angle of the first harmonic term
λ	Non-linear coefficient of the typical system with snap-through mechanism
μ_{mag}	Magnetic permeability

μ_0	Permeability of intervening medium
π	circumference ratio
ρ_a	Density of aluminum alloy blocks
ρ_b	Density of beryllium copper shims
ρ_m	Density of magnets
σ_{piezo}	Stress in a piezoelectric material for general applications
$\sigma_{piezo-yield}$	Yield stress of piezoelectric materials
σ_b	Yield stress of beryllium copper shims
τ	Non-dimensional oscillation time
ϕ	Phase angle
φ	Inclination of springs in the typical system with snap-through mechanism
Φ	Diameter of magnetic buttons in the first new design
Φ_{II}	Diameter of magnetic buttons in the second new design
Φ_r	Sunk hole diameter of ring magnets in the first new design
Φ_R	Diameter of ring magnets in the first new design
ω	Excitation frequency
ω_{closed}	Fundamental frequency of the new device in a closed circuit
ω_n	Natural frequency
ω_{open}	Fundamental frequency of the new device in a open circuit
Ω	Non-dimensional excitation frequency
$\Omega_{1,2}$	Peak frequency of a non-linear system
Ω_{Fun}	Resonance starting frequency of a non-linear system

Other Symbols

FRC	Frequency response curve
N1	First new mechanical system design
$\mathrm{N1}_{1,2}$	First new mechanical system design having column height 12 mm and 15 mm, respectively

N2	Second new mechanical system design
ND	New piezoelectric non-linear vibration energy scavenging device
$ND_{1,2}$	New device having column height 7 mm and 12 mm, respectively
NS	Numerical simulation
rms	Root mean square
T1	Typical mechanical system with hardening mechanism
T2	Typical mechanical system with softening mechanism
T3	Typical mechanical system with snap-through mechanism
$T3_{1,2,3}$	Typical mechanical system with snap-through mechanism with non-linear coefficient 0.1, 0.5 and 1, respectively

CHAPTER 1 INTRODUCTION

1.1 Powering Wireless Sensors and Communication Nodes

Pervasive networks of wireless sensors and communication nodes are widely used in areas including structural health monitoring and environment control. It has been predicted that low power embedded electronic devices will become a common part of the environment and perform functions in applications ranging from entertainment to factory automation [1-5].

The total power requirement of a wireless sensor can be less than 1 μW in active mode, and much less in sleep mode, due to low power circuit design, the advanced Integrated Circuit (IC) manufacturing and networking technology [6]. In addition, the sensor network can operate in a multi-hop fashion in which multiple low power and low cost nodes replace a long transmission distance network (over 10 meters) [1, 7].

Wiring power and batteries are generally adopted to power massive nodes in a dense network. However, wiring power is not an economical option due to its high setup cost, whereas batteries have limited operational lifespan. For instance, the non-rechargeable lithium battery can provide up to 800 WH/L or 2.88 $\mathrm{J/mm^3}$. Therefore, a 1×10^3 $\mathrm{mm^3}$ battery lasts about 8000 hours or 333 days when powering an electronic device consuming 100 μW (an aggressive goal) [1]. It needs to be replaced within one year. Therefore, developing alternative powering methods for wireless sensors and communication nodes becomes a pressing need.

1.2 Energy Scavenging Technologies

Technologies that enable a wireless electronic device to generate its own power have been considered as a desirable way to solve the problem. The fundamental principle is that a wireless electronic device converts energy sources in ambient environment into electricity to power itself. As a result, the lifespan of the wireless electronic device is only limited by the failure of its own components [1]. A number of energy scavenging technologies have been developed to harvest corresponding ambient energy from solar light, vibration, acoustic noise or temperature variation. A comparison of the power densities of these technologies is given in Table 1.1, which also includes batteries and other energy storage technologies. The upper half (in white) of Table 1.1 shows the power densities of the energy scavenging technologies where the power density remains constant with the increase in lifetime. In contrast, the power density of the energy storage technologies showed in the lower half (in gray) decreases with time.

1.2.1 Solar Energy

Solar energy is plentiful outdoors during the daytime. The power density is 15 μW/mm^3 in direct sunlight at midday, and falls off by a factor of 100 on a cloudy day (see Table 1.1). The indoor power density drops dramatically to around 6×10^{-3} μW/mm^3. The silicon solar cell is the most frequently used device to convert solar energy into electrical energy. The energy conversion efficiency of a single crystal silicon cell can range from 12% to 25%.

1.2.2 Vibration Energy

As shown in Table 1.1, about 0.2 μW/mm^3 can be generated from vibration energy sources existing in a typical built environment according to theoretical and experimental data [1], which is sufficient to power wireless sensors and communication nodes. Reviews of applications of vibration energy are given in references [8 – 12]. A typical vibration energy scavenging device consists of two main parts, i.e., the mechanical system (or the mechanical structure) and the transduction mechanism (or the transducer). The latter is used to produce electrical energy from motions of the mechanical system due to vibrations. The conversion efficiency of vibration energy is low in existing vibration energy scavenging devices. A more detailed review of the working principle and the drawbacks of existing vibration energy scavenging devices will be given in Chapter 2.

1.2.3 Acoustic Noise

The power density generated from acoustic noise is 3×10^{-6} μW/mm^3 at 75 Db and 9.6×10^{-4} μW/mm^3 at 100 Db (see Table 1.1), which is far too low to power a wireless electrical device, except in certain environment with supreme high noise levels.

1.2.4 Temperature Variations

The natural temperature variations over a 24 hours period could also be a source for electrical energy harvesting from the environment. A combination of theoretical studies and experiments shows that an average of 0.01 μW/mm^3 can be generated by an enclosed volume containing an ideal gas with an average variation of 7 $^\circ$C [1]. However, the achievement is based on the assumption that no power losses in the conversion process.

Table 1.1 Power density comparison of energy scavenging and energy storage technologies [1].

	Power Density (μW/mm^3) 1 Year Lifetime	**Power Density (μW/mm^3) 10 Year Lifetime**
Solar (Outdoor)	15 – direct sun 0.15 – cloudy day	15– direct sun 0.15 – cloudy day
Solar (Indoor)	6×10^{-3} – office desk	6×10^{-3} – office desk
Vibrations	0.2	0.2
Acoustic Noise	3×10^{-6} at 75 Db 9.6×10^{-4} at 100 Db	3×10^{-6} at 75 Db 9.6×10^{-4} at 100 Db
Daily Temp. Variation	0.01	0.01
Batteries (Non-rechargeable Lithium)	45×10^{-3}	3.5×10^{-3}
Batteries (Rechargeable Lithium)	7×10^{-3}	0
Hydrocarbon fuel (Micro Heat Engine)	0.333	0.033
Fuel Cells (Methanol)	0.28	0.028
Nuclear Isotopes (Uranium)	6×10^{3}	0.6×10^{3}

1.3 Objective

The brief introduction above indicates that energy scavenging technologies based on solar and vibration energies are most attractive. Both solutions meet the power density requirement of existing wireless sensors. However, the power density of solar energy is affected by ambient environment. In an indoor environment, the power density decreases to 6×10^{-3} μW/mm^3 which is insufficient to power a wireless electrical device [1]. Unlike solar energy, the power density of vibration energy is normally unaffected by ambient environment variation. Therefore vibration energy can be considered as the optimal ambient energy to be integrated into scavenging technologies to power existing wireless sensors and communication nodes. The focus of the dissertation is on the development of a novel vibration energy scavenging device with higher conversion efficiency than that of existing devices with the suitable selection of external conditions.

1.4 Layout of Dissertation

Chapter 2 firstly reviews various existing types of vibration sources. Subsequently, a generic vibration energy to electrical energy conversion model is given which can be used to predict the power output. Furthermore, comparisons of the energy density of three transduction mechanisms are outlined. Finally, a particular type of vibration energy scavenging device, namely the piezoelectric device, is reviewed including its advantages and inherent limitations that can affect the vibration to electricity conversion efficiency.

Chapter 3 intends to find an effective non-linear mechanism with desirable dynamic behaviors for the mechanical system in the forthcoming vibration energy scavenging device. To do so, static and dynamic behaviors of three non-linear mechanisms are analyzed based on the corresponding typical mechanical systems. Softening and hardening mechanisms are firstly investigated. Their strengths and limitations are discussed, that leads to the static and dynamic analysis of the snap-through mechanism. The practical constrains of the typical mechanical systems for the three mechanisms are analyzed subsequently. Based on this analysis, the snap-through mechanism is chosen as the optimal non-linear mechanism for the mechanical system design.

A new mechanical system design based on a snap-through mechanism is outlined in Chapter 4. A series of mechanical experimental results are reported which validate the new design. The practical constraints of the new design are pointed out, followed by an improved design to overcome its drawbacks. Furthermore, a novel vibration energy scavenging device based on the improved design and the piezoelectric transduction mechanism is fabricated. A series of electrical experimental results are given to demonstrate the advantage of the new device.

The main achievements of the current research and suggestions for future work are summarized in Chapter 5, which conclude the dissertation.

CHAPTER 2 LITERATURE REVIEW

2.1 Vibration Sources

Vibration occurs commonly in household appliances, e.g., fridges and microwave ovens, as well as in large structures, e.g., buildings and bridges. Table 2.1 shows various vibration sources, including their peak accelerations and corresponding frequencies. Vibration sources ranging from $0.05\ \text{m/s}^2$ to $10\ \text{m/s}^2$ in peak acceleration and 5 Hz to 240 Hz in frequency are commonly considered as the operational vibration range for the vibration energy scavenging device design.

Table 2.1 List of vibration sources with the peak acceleration and corresponding frequency [1].

Vibration Source	Peak Acceleration (m/s^2)	Frequency of Peak (Hz)
Base of 5 HP 3-axis machine tool with $36''$ bed	10	70
Kitchen blender casing	6.4	121
Clothes dryer	3.5	121
Car instrument panel	3	13
Small microwave oven	2.25	121
HVAC vents in office building	0.2 – 1.5	60
Bread maker	1.03	121
External windows (size $2\ \text{ft} \times 3\ \text{ft}$) next to a busy street	0.7	100
Washing Machine	0.5	109
Fridge	0.1	240
Second story floor of a wood frame office building	0.2	100
Bridge response under moving vehicle with driving velocity 20 km/h	0.05	5

2.2 Generic Vibration-to-Electricity Conversion Model

A typical vibration energy scavenging device consists of two main parts, the mechanical system and the transduction mechanism. The former is a mechanical structure which turns ambient vibration into self-motion, whereas the later harvests electrical energy from motion of the mechanical system. The electromagnetic (inductive), electrostatic (capacitive) and piezoelectric transduction mechanisms are commonly used transduction mechanisms.

Williams and Yates proposed a generic vibration-to-electricity conversion model [13], which is a mass-spring-dampers linear mechanical system enclosed in a frame without the constraint of transduction mechanisms as shown in Fig. 2.1 [13].

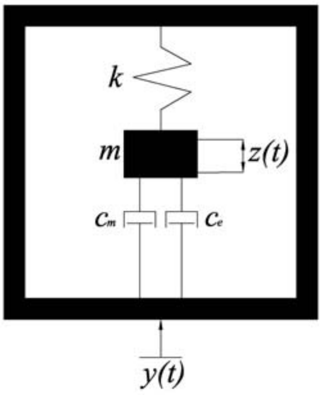

Figure 2.1 Generic vibration-to-electricity model

The motion equation of the model is

$$m\ddot{z}+\left(c_m+c_e\right)\dot{z}+kz=-m\ddot{y}\,, \tag{2.1}$$

where z is the relative displacement between the frame and the mass, m the mass, c_m the mechanical damping coefficient, c_e the electrically induced damping coefficient, k the spring constant, '.' the differential with respect to oscillation time t and y the external sinusoidal vibration displacement,

$$y(t) = Y\sin(\omega t) \tag{2.2}$$

in which Y is the maximum excitation displacement and ω is the excitation frequency.

The standard steady-state solution for z is given by

$$z = \frac{\omega^2}{\sqrt{\left(\frac{k}{m} - \omega^2\right)^2 + \left(\frac{(c_m + c_e)\omega}{m}\right)^2}} Y\sin(\omega t - \phi), \tag{2.3}$$

where ϕ, the phase angle, is given by

$$\phi = \tan^{-1}\left(\frac{(c_m + c_e)\omega}{k - \omega^2 m}\right). \tag{2.4}$$

The power removed from the mechanical system is equal to the power harvested by the electrical damper, i.e., c_e. The electrically induced force is $c_e \dot{z}$. And the electric power is given by

$$P_e = c_e \int_0^{\dot{z}} \dot{z} d\dot{z} = \frac{1}{2} c_e \dot{z}^2 . \tag{2.5}$$

Differentiating Eq. (2.3) with respect to t, substituting $\dot{z}$ into Eq. (2.5) and rearranging terms yield the following expression for P_e,

$$p_e = \frac{m\varsigma_e\omega_n\omega^2\left(\frac{\omega}{\omega_n}\right)^3 Y^2}{\left(2\varsigma_T\frac{\omega}{\omega_n}\right)^2 + \left(1-\left(\frac{\omega}{\omega_n}\right)^2\right)^2}, \tag{2.6}$$

where ω_n, the natural frequency of the mass spring system, is $\sqrt{\frac{k}{m}}$, ς_e, the electrically induced damping ratio, $\frac{c_e}{2m\omega_n}$, ς_m, the mechanical damping ratio, $\frac{c_m}{2m\omega_n}$, and ς_T, the overall damping ratio, $\frac{c_e + c_m}{2m\omega_n}$ or $\varsigma_e + \varsigma_m$.

Assuming the natural frequency of the mass-spring-dampers system matches the excitation frequency, i.e., $\omega_n = \omega$, Eq. (2.6) is reduced to

$$P_e = \frac{m\varsigma_e\omega^3 Y^2}{4\varsigma_T^2}, \tag{2.7}$$

or

$$P_e = \frac{m\varsigma_e A^2}{4\omega\varsigma_T^2}, \tag{2.8}$$

where A is the maximum acceleration of input vibration, and equals $\omega^2 Y$.

To understand the effect of the mass m, the damping ratios including the electrically induced damping ratio ς_e and the mechanical damping ratio ς_m, the excitation frequency ω and the acceleration of vibration sources A on the output power P_e, Figs.

2.2 – 2.5 are plotted based on Eq. (2.8). In addition, according to Roundy [1], the acceleration of vibration sources in ambient environment is generally either constant or decreasing with frequency. Therefore, the acceleration A is chosen as 5 m/s^2. Some important conclusions can be drawn from Figs. 2.2 – 2.5.

- ς_m should be as low as possible as shown in Figs. 2.2 and 2.3.
- The output power is inversely proportional to the natural frequency, and is maximized when the excitation frequency is equal to the natural frequency as shown in Fig. 2.4.
- The output power is linearly proportional to mass as shown in Fig. 2.5.

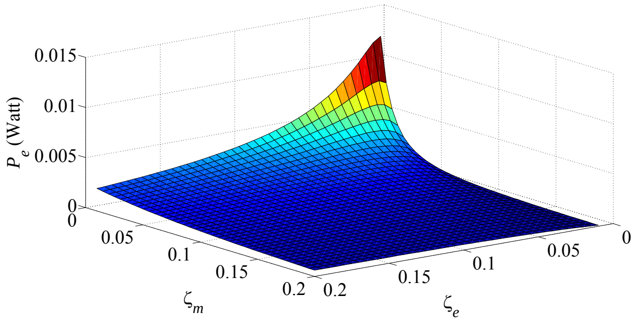

Figure 2.2: Power output vs. mechanical and electrical damping ratios when m=0.05 Kg, ω_n=ω=100 Hz **and** A=5 m/s^2.

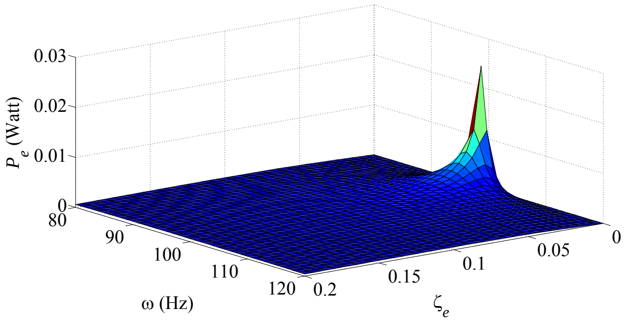

Figure 2.3: Power output vs. input frequency and electrical damping ratio when m=0.05 Kg, $\omega_n = 100$ Hz, $A = 5$ m/s^2 **and** $\varsigma_e = \varsigma_m$.

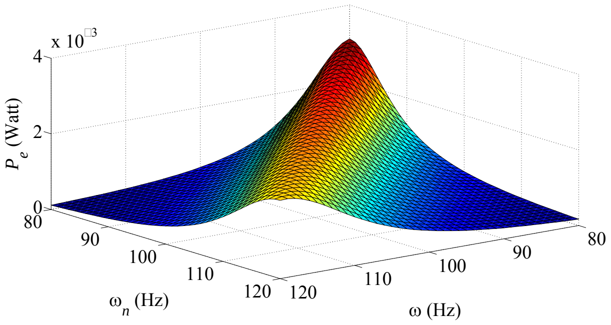

Figure 2.4: Power output vs. resonant and input frequencies when m=0.05 Kg, A=5 m/s^2 **and** $\varsigma_e = \varsigma_m = 0.05$**.**

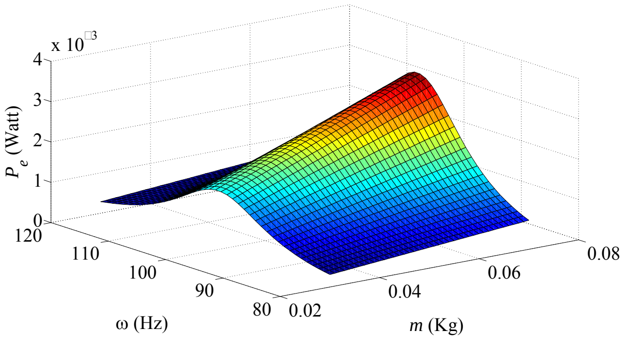

Figure 2.5: Power output vs. input frequency and mass of the system when $\mathrm{A} = 5\ \mathrm{m/s^2}$**,** $\omega_n = 100\ \mathrm{Hz}$ **and** $\varsigma_e = \varsigma_m = 0.05$**.**

2.3 Transduction Mechanisms

2.3.1 Electromagnetic Transduction Mechanism

Electromagnetic induction is the generation of electric current in a conductor which is located in a magnetic field. The conductor is typically formed as a coil. The change of the magnetic field or the relative movement between the coil and magnetic field induces a current which flows in the coil. The open circuit voltage across the coil in the later case depends on the strength of the magnetic field, the number of turns of the coil, the length of a coil and the velocity of the relative movement, and is given by

$$V_{mag} = N_{mag} B_{mag} l_{mag} v_{mag}, \tag{2.9}$$

where N_{mag} is the number of turns in the coil, B_{mag} the strength of the magnetic field, l_{mag} the length of one coil and v_{mag} the velocity of the relative motion.

There are two significant advantages of the electromagnetic transduction mechanism in the vibration energy scavenging. First, in comparison with the electrostatic transduction mechanism which will be reviewed next, no start-up voltage is needed. Second, the device based on the electromagnetic transduction mechanism can be designed to avoid any mechanical contact, which extends the durability of the device and reduces mechanical damping. A main drawback is the low voltage level, typically at 0.1 V maximum, for a device whose volume is 1×10^3 mm^3[1].

2.3.2 Electrostatic Transduction Mechanism

A capacitor consists of two conductors which are electrically isolated from each other normally by air, vacuum or an insulator. A start-up DC voltage is connected to a capacitor initially and then disconnected, leading to a pair of equal but opposite charges on both conductors [14]. The energy stored in the capacitor changes when the conductors have relative motion, which provides the mechanism for the conversion from mechanical energy to electrical energy. The voltage generated by a capacitor is

$$V_{sta} = Q_{sta} / C_{sta}, \tag{2.10}$$

where Q_{sta} is the charge on the capacitor, and C_{sta}, the capacitance, is

$$C_{sta} = \frac{\varepsilon_{sta} l_{sta} w_{sta}}{d_{sta}}, \tag{2.11}$$

in which ε_{sta} is the dielectric constant (or permittivity) between the plates, l_{sta} the length of the plate, w_{sta} the width of the plate and d_{sta} the distance between the plates.

Substituting Eq. (2.11) into Eq. (2.10) and rearranging terms yields

$$V_{sta} = \frac{Q_{sta} d_{sta}}{\varepsilon_{sta} l_{sta} w_{sta}}. \tag{2.12}$$

The most significant strength of the electrostatic transduction mechanism is that it is easier to be integrated with microelectronics than the electromagnetic and piezoelectric transduction mechanisms which will be reviewed next, with the assistance of MEMS technology. Furthermore, it can generate 2 volts or more directly for a device with a volume of 1×10^3 mm^3 [1]. However, the electrostatic transduction mechanism has two disadvantages. First, a DC voltage source is required to start up the conversion process. Secondly, in order to prevent the capacitor electrodes from contacting each other, which could lead to short-circuiting, a mechanical displacement protector has to be included.

2.3.3 Piezoelectric Transduction Mechanism

Common piezoelectric materials include zirconate titanate piezoceramics (PZT-5H (soft) and PZT-5A (hard)), barium titanate (BatiO$_3$) and polyvinylidence fluoride (PVDF). They usually come in the form of thin films (less than 0.1 mm). Because the spontaneous separation of charge within certain crystal structures under right conditions produces an electric dipole, an electric field can be generated when a piezoelectric material is stressed or unstressed [1, 14 and 15]. The variety of the piezoelectric material, the direction of the input force, the orientation of the polarization and the arrangement of the electrode are key factors to determine the function mode of the piezoelectric material [16]. The established electromechanical coupling equations for a piezoelectric material are

$$\{S\} = \left[s^E\right]\{T\} + \left[d^t\right]\{E\}, \tag{2.13}$$

and

$$\{D\} = \left[d\right]\{T\} + \left[\varepsilon^T\right]\{E\}, \tag{2.14}$$

where $\{S\}$ is the six-dimensional strain vector, $\{T\}$ the six-dimensional stress vector, $\{D\}$ the three-dimensional electric displacement vector, $\{E\}$ the three-dimensional electric field strength vector, $\left[s^E\right]$ the six by six compliance matrix evaluated at constant electric field, $\left[d\right]$ the three by six matrix of piezoelectric strain coefficients, $\left[d^t\right]$ the six by three matrix converse piezoelectric effect, and $\left[\varepsilon^T\right]$ the three by three dielectric constant matrix evaluated at constant stress [17].

Figure 2.6 shows two different function modes of piezoelectric materials. Labels 1, 2 and 3 represent three orthogonal directions. A piezoelectric material can be used in either 33 or 31 mode, both of which are poled in direction 3. In 33 mode, both of the voltage and the mechanical stress act in direction 3. In 31 mode case the voltage acts in direction 3 whereas the mechanical stress acts in direction 1. Table 2.2 shows some important coefficients of common piezoelectric materials in both modes. g_{31} and g_{33} are the piezoelectric voltage constants, i.e., the electric field generated per unit of mechanical stress, and can be defined as [14]

$$g_{31} = d_{31} / \varepsilon_{33}^{T}, \tag{2.15}$$

$$g_{33} = d_{33} / \varepsilon_{33}^{T}. \tag{2.16}$$

k_{31} and k_{33} are the electromechanical coupling factors and are equal to electrical energy converted over mechanical energy input, and can be defined as [14]

$$k_{31}^{2} = d_{31}^{2} / \left(s_{11}^{E} \varepsilon_{33}^{T} \right), \tag{2.17}$$

$$k_{33}^{2} = d_{33}^{2} / \left(s_{33}^{E} \varepsilon_{33}^{T} \right). \tag{2.18}$$

Note that the strain coefficient, voltage constant and coupling factor of 33 mode are higher than those of 31 mode. However, high mechanical stiffness in direction 3 of a piezoelectric film makes the material straining difficult, leading to little energy being harvested in 33 mode when subjected to a small force [19]. Therefore, 31 mode has always been selected as the preferred function mode in existing piezoelectric vibration energy scavenging devices.

For 31 mode, Eqs. (2.13) and (2.14) can be expressed as

$$S_{1} = s_{11}^{E} T_{1} + d_{31} E_{3}, \tag{2.19}$$

$$D_{3} = d_{31} T_{1} + \varepsilon_{33}^{T} E_{3}. \tag{2.20}$$

Replacing S_1, s_{11}^E and T_1 by the common notations δ_{piezo}, $1/Y_{piezo}$ and σ_{piezo} where Y_{piezo} is the Young's Modulus of piezoelectric materials and substituting into Eqs. (2.19) and (2.20) yields

$$\delta_{piezo} = \sigma_{piezo} / Y_{piezo} + d_{31}E_3, \tag{2.21}$$

$$D_3 = d_{31}\sigma_{piezo} + \varepsilon_{33}^T E_3. \tag{2.22}$$

Like the electrostatic transduction mechanism, the piezoelectric transduction mechanism can directly generate appropriate voltages in the range of one to several volts and currents in the range of tens to hundreds microAmps when the volume of the device is 1×10^3 mm^3 [1]. However, unlike the electrostatic transduction mechanism, no mechanical displacement protector is necessary in a suitably designed vibration energy scavenging device based on the piezoelectric transduction mechanism. In addition, the piezoelectric transduction mechanism can initiate the conversion process without a voltage source. A drawback of the piezoelectric transduction mechanism is that the electromechanical coupling ratio is reduced when it is integrated into MEMS systems and subjected to an asymmetry strain along the piezoelectric film [20].

2.3.4 Comparison of Energy Densities of Transduction Mechanisms

Energy density is an important parameter when comparing the three transduction mechanisms.

The electromagnetic transduction mechanism

The maximum energy density of an electromagnetic converter is given by [1]

$$u_{mag} = \frac{B_{mag}^2}{2\mu_{mag}}, \tag{2.23}$$

where B_{mag} is the magnetic field strength and μ_{mag} is the magnetic permeability.

Maluf [21] adopted 0.1 Tesla as the maximum strength of the magnetic field. Therefore, according to Eq. (2.23) the energy density is 4×10^{-3} mJ/mm^3 when the magnetic permeability of free space is 1.26×10^{-9} H/mm. If an extremely strong magnetic field, e.g., 1 Tesla, is chosen as the theoretical maximum magnetic field, the energy density can reach 0.4 mJ/mm^3.

The electrostatic transduction mechanism

For a capacitive device, the energy density is [1],

$$u_{sta} = \frac{\varepsilon_{sta}\left|E_{sta}\right|^2}{2}, \tag{2.24}$$

in which ε_{sta} is the dielectric constant and $E_{sta} = -\frac{V_{sta}}{d_{sta}}$ is the electric field strength.

Assuming a realistic 30 volts over a 1 μm gap of an electrostatic capacitor, i.e., $E_{sta} = 0.03$ MV/mm, the energy density would be 4×10^{-3} mJ/mm^3 with the dielectric constant of free space $\varepsilon_0 = 8.85 \times 10^{-15}$ F/mm. Furthermore, according to Paschen's curve [1], the maximum electric field that gas in the air at atmospheric pressure can withstand is 0.1 $\mathrm{MV/mm}$. Therefore, the theoretical maximum energy density of a capacitive device can be 0.044 $\mathrm{mJ/mm^3}$.

The piezoelectric transduction mechanism

Equation (2.22) can be reduced to Eq. (2.25) by assuming a piezoelectric material working in an open circuit and replacing d_{31}, E_3 and ε_3^T by d_{piezo}, E_{piezo} and ε_{piezo} for general applications, as

$$\varepsilon_{piezo} E_{piezo} = -d_{piezo} \sigma_{piezo} . \tag{2.25}$$

A piezoelectric material can also be considered as a capacitive device. Therefore, multiplying each side by $E_{piezo}/2$, Eq. (2.25) becomes

$$\frac{\varepsilon_{piezo} E^2_{piezo}}{2} = \frac{d^2_{piezo} \sigma^2_{piezo}}{2\varepsilon_{piezo}} . \tag{2.26}$$

The energy density of a piezoelectric material is

$$u_{piezo} = \frac{d^2_{piezo} \sigma^2_{piezo}}{2\varepsilon_{piezo}} . \tag{2.27}$$

For a specific piezoelectric material, the maximum energy density can be achieved when the stress across the material reaches its yield strength $\sigma_{piezo-yield}$. The maximum energy density of a common piezoelectric material, e.g., PZT-5H, is 0.035 $\mathrm{mJ/mm^3}$. In practice, a margin factor of 2 will be implied [1], reducing the energy density to 0.0175 mJ/mm^3. Moreover, the theoretical maximum energy density can be raised to 0.335 mJ/mm^3 by choosing a single crystal piezoelectric material, such as PZN-PT.

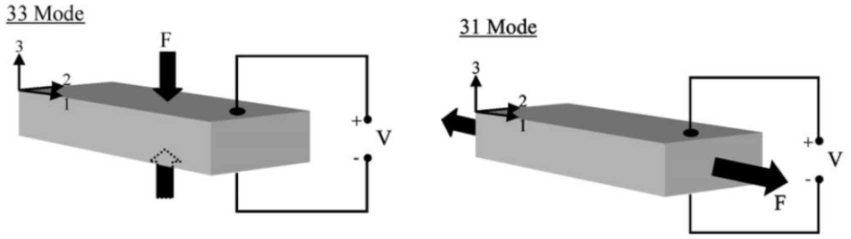

Figure 2.6: Illustration of 33 mode and 31 mode working models of piezoelectric materials.

Table 2.2: Coefficients of common piezoelectric materials [18].

Property	PZT-5H	PZT-5A	$BaTiO_3$	PVDF
$d_{33}\ (10^{-12}\mathrm{CN}^{-1})$	593	374	149	-33
$d_{31}\ (10^{-12}\mathrm{CN}^{-1})$	-274	-171	78	23
$g_{33}\ (10^{-3}\mathrm{VmN}^{-1})$	19.7	24.8	14.1	330
$g_{31}\ (10^{-3}\mathrm{VmN}^{-1})$	-9.1	-11.4	5	216
k_{33}	0.75	0.71	0.48	0.15
k_{31}	0.39	0.31	0.21	0.12
Relative permittivity $(\varepsilon_{33}/\varepsilon_0)$	3400	1700	1700	12

2.3.5 Summary of Transduction Mechanisms

Three transduction mechanisms adopted by existing vibration energy scavenging devices have been reviewed here. Table 2.3 summarizes the primary advantages and disadvantages of each type of transduction mechanisms, which can be a basis for selecting a suitable transduction mechanism for a vibration energy scavenging device.

Note that the electromagnetic transduction mechanism cannot satisfy the voltage requirement of existing wireless sensors and nodes. In addition, a separate voltage is needed to start up the conversion process of the electrostatic transduction mechanism, which is impractical for on-site applications. The piezoelectric transduction mechanism exhibits all strengths of the electromagnetic transduction mechanism and also provides suitable voltages and currents for existing wireless sensors and nodes. Therefore, the piezoelectric transduction mechanism is chosen as the primary transduction mechanism for the research reported in this dissertation, even though it has a relative low coupling ratio in micro-fabrication process and when it is subjected to asymmetry strain.

Table 2.3: Summary of the comparison of the three transduction mechanisms.

Transduction Mechanism	Advantages	Disadvantages	Practical Maximum Energy Density (mJ/mm^3)	Theoretical Maximum Energy Density (mJ/mm^3)
Piezoelectric	1. No start-up voltage source needed. 2. No displacement protector needed. 3. Voltages of one to several volts.	Relative low coupling ratio in MEMS system and when subjected asymmetry strain.	17.5×10^{-3}	335×10^{-3}
Electrostatic	1. Easier to integrate with microelectronics. 2. Voltages of two to several volts.	1. Start-up voltage source needed. 2. Displacement protector needed.	4×10^{-3}	44×10^{-3}
Electromagnetic	1. No start-up voltage source needed. 2. No displacement protector needed.	Low voltage generated.	4×10^{-3}	400×10^{-3}

2.4 Existing Piezoelectric Vibration Energy Scavenging Devices

Currently used vibration energy scavenging devices with the piezoelectric transduction mechanism can be classified into linear and nonlinear categories in accordance with the type of the mechanisms used by the mechanical system.

2.4.1 Linear Piezoelectric Vibration Energy Scavenging Devices

A bimorph cantilever beam with an additional mass at the end is a common mechanical system design among linear piezoelectric vibration energy scavenging devices due to its comparatively low resonant frequency, low structural volume and high level of strain in the piezoelectric layer.

Roundy and Wright [17] presented such a linear piezoelectric vibration energy scavenging device with varying dimensions and a fixed total volume of 1×10^3 mm^3 (see Fig. 2.7(a)). A prototype was fabricated with two layers of PZT-5A and a steel center shim. Experimental results showed that the maximum 375 μW and 190 μW power could be transferred to an optimal load and a capacitive load, respectively, with the driving vibration of $2.5\ \text{m/s}^2$ at 120 Hz.

The cantilever beam can also be tapered in order to obtain a symmetrical strain along the piezoelectric film, which was firstly proposed by Glynne-Jones *et al.* [22, 23]. In their model, the piezoelectric material composited by the PZT-5H powder was printed onto both sides of a hardened AISI 316 stainless steel as shown in Fig. 2.7 (b). It could generate up to 3 μW electric power into a $333\ \text{k}\Omega$ load resistance when the excitation frequency met the natural frequency of the generator, which was $80.1\ \text{Hz}$. More information about the others can be found in Refs [24-26].

2.4.2 Limitations of Existing Linear Piezoelectric Vibration Energy Scavenging Devices

Existing linear piezoelectric vibration energy scavenging devices generate the maximum power when the natural frequency coincides with the excitation frequency. The bandwidth of a linear system is approximately $2\varsigma\omega_n$ [30]. For instance, if the natural frequency of a linear system is 20 Hz with damping ratio 0.025, the bandwidth will be 1 Hz which is called the half-power bandwidth of a linear system [30]. In other words, the amount of energy harvested by the generator is optimal when the excitation frequency ranges from 19.5 Hz to 20.5 Hz. The energy harvested decreases dramatically otherwise. Because the excitation frequency of vibration source cannot be predicted accurately, widening the bandwidth of linear piezoelectric vibration energy scavenging devices to improve the vibration to electrical energy coupling efficiency has become the primary research objective.

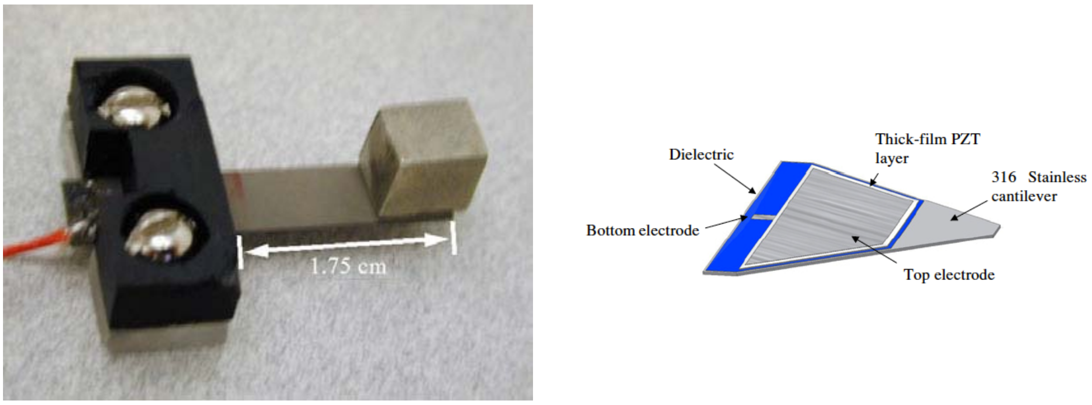

(a) **(b)**

Figure 2.7: (a) Bimorph cantilever beam generator by Roundy and Wright [17], (b) tapered cantilever beam generator by Glynne-Jones *et al.* [22].

2.4.3 Improvements to Linear Piezoelectric Vibration Energy Scavenging Devices

Methods for improving the efficiency of vibration energy harvesting mainly involve altering the natural frequency of a linear mechanical system and adopting a non-linear mechanical system.

Leland and Wright [27] proposed a resonance tuning method of a piezoelectric vibration energy scavenging generator by a compressive axial load at both ends of a simply supported piezoelectric bimorph shown in Fig. 2.8 (a). Experimental results showed that the resonance frequency of the vibration generator under a compressive axial load could be reduced up to $24\ \%$. A sample generator mounted with a 7.1 g proof mass could generate $300\ \mu\mathrm{W}$ to $400\ \mu\mathrm{W}$ power with a constant driving acceleration of $9.8\ \mathrm{m/s^2}$ at the operation frequency from 200 Hz to 250 Hz.

Challa *et al.* [28] adopted four permanent magnets generating attractive force and repulsive force to alter the resonant frequency of a piezoelectric cantilever beam by adjusting distances between the magnets (see Fig. 2.8 (b)). It was reported that the resonance frequency could be shifted by 22 Hz to 23 Hz with power generated between 240 and $280\ \mu\mathrm{W}$ under a driving acceleration of $0.8\ \mathrm{m/s^2}$.

Marinkovic and Koser [29] proposed a wide bandwidth vibration energy scavenger known as Smart Sand. They adopted fixed-fixed beams as the mechanical system which was non-linear in nature (see Fig. 2.8 (c)). Smart Sand could extend the operation bandwidth (or off-resonant bandwidth) to more than 100 Hz.

Although the operation bandwidth has been broadened at the first two vibration energy scavenging devices, the problem in narrow bandwidth still cannot be solved completely due to the fact that the resonant frequency of both designs was altered by an external power, which is difficult to implement in practical applications. Smart Sand can extend the bandwidth without an external power due to the adoption of a non-linear mechanical system. However, the output displacements or power of the device are lower than those of linear vibration energy scavenging devices of equal volume in an identical vibration source. The reason for that will be explored in details in Chapter 3.

In view of the drawbacks of existing piezoelectric vibration energy scavenging devices discussed above, it is important to find an alternative non-linear mechanical system with desirable dynamic characteristics for vibration energy scavenging devices.

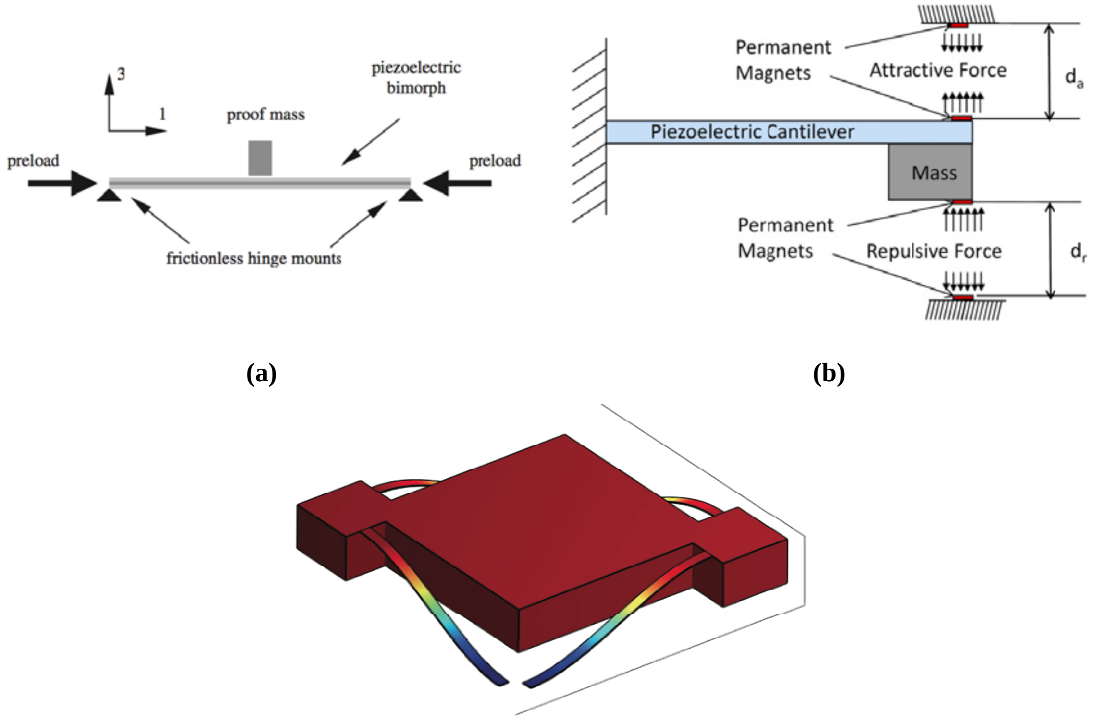

(a) (b)

(c)

Figure 2.8: (a) Resonance tuning generator with compressive axial load by Leland and Wright [27], (b) resonance tuning generator with permanent magnets by Challa *et al.* [28],and (c) Smart Sand with fixed-fixed beams by Marinkovic and Koser [29]

CHAPTER 3   NON-LINEAR MECHANISMS

The reviews in Chapter 2 suggest that non-linear mechanisms could be a solution to the problems in existing linear piezoelectric vibration energy scavenging devices. Therefore, a number of non-linear mechanisms including hardening, softening and snap-through will be investigated in this chapter in order to determine the most suitable one for the vibration energy scavenging devices.

3.1 Hardening and Softening Mechanisms

3.1.1 Typical mechanical system with hardening mechanism

Figure 3.1 shows a fixed-fixed rectangular beam subjected to a vertical concentrated load F_B at one of the fixed ends. This structural design is referred to as T1 hereafter. Assume that the shape of T1 can be represented by half of a cosine shape [36]

$$y_b = \frac{z}{2} - \frac{z}{2}\cos\frac{\pi l_b}{L_B}, \tag{3.1}$$

where y_b represents the shape of the fixed-fixed beam, z the deflection of the beam of length L_B at its right end, and l_b the horizontal from the left end.

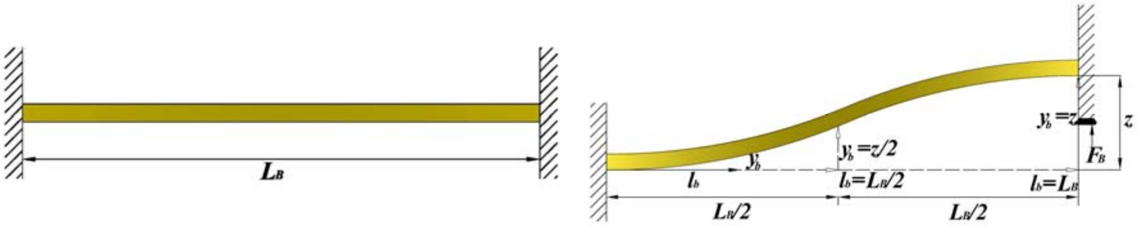

(a)　　(b)

Figure 3.1: (a) A fixed-fixed beam T1; (b) its deformed shape when F_B acts on its right end.

The deflected length of the fixed-fixed beam is

$$L_D = \int_0^{L_B} \sqrt{1 + y_b'^2}\, dl_b \doteq \int_0^{L_B} \left(1 + \frac{y_b'^2}{2}\right) dl_b = L_B + \Delta L_B\,, \tag{3.2}$$

where $\Delta L_B = \frac{1}{2}\int_0^{L_B} y_b'^2 dl_b$.

According to Eq. (3.1),

$$y_b' = \frac{\pi z}{2L_B}\sin\frac{\pi l_b}{L_B}\,, \tag{3.3}$$

and

$$y_b'^2 = \frac{\pi^2 z^2}{8L_B^2}\left(1 - \cos\frac{2\pi l_b}{L_B}\right). \tag{3.4}$$

Substituting Eq. (3.4) into Eq. (3.2) and rearranging terms result in the following expression:

$$L_D = L_B + \Delta L_B = L_B + \frac{\pi^2 z^2}{16L_B}. \tag{3.5}$$

Furthermore, the induced axial tension can be given as

$$T_B = A_B E_B \frac{\Delta L_B}{L_B} = \frac{A_B E_B \pi}{16L_B^2} z^2, \tag{3.6}$$

where A_B is the cross-section area of the fixed-fixed beam T1, and E_B the Young's modulus, assuming the beam behaves linear elastically.

The bending moment can be found as

$$M_B = \frac{6E_B I_B}{L_B^2} z, \tag{3.7}$$

where I_B is the second moment area of the beam.

Therefore, the concentrated load F_B is given by

$$F_B = \frac{2M_B}{L_B} + \frac{T_B z}{L_B} = \frac{12E_B I_B}{L_B^3} z + \frac{A_B E_B \pi}{16L_B^3} z^3. \tag{3.8}$$

Equation (3.8) shows that the second moment area and the cross-section area are the critical factors which determine the force-deflection relationship of T1. It can be seen that a suitable selection of geometrical parameters of the beam section can lead to a non-linear relationship between the force and deflection. Equation (3.8) can be rewritten as

$$F_B = A_{T1} z + B_{T1} z^3. \tag{3.9}$$

in which coefficients $A_{T1} = \frac{12E_B I_B}{L_B^3}$ and $B_{T1} = \frac{A_B E_B \pi}{16L_B^3}$.

Generally T1 is considered as a typical mechanical system with a hardening mechanism which has the restoring force in the form of Eq. (3.9) [35].

3.1.2 Typical mechanical system with softening mechanism

Figure 3.2 shows a pendulum consisting of a mass m and a hinged weightless rod of length L_P and inclination θ. It is referred to as T2 hereafter [40]. The restoring force of the pendulum is

$$F_P = mg\sin\theta, \tag{3.10}$$

where $-\frac{\pi}{2} \le \theta \le \frac{\pi}{2}$.

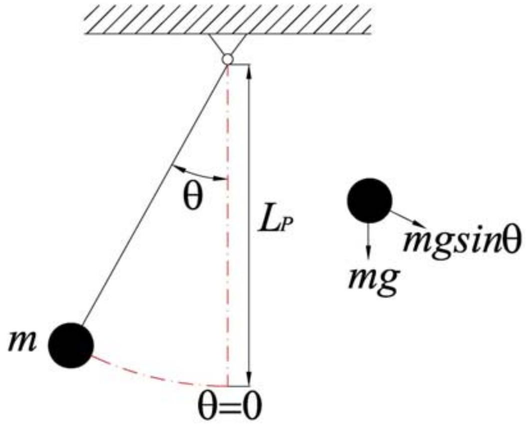

Figure 3.2: A pendulum, where m is the mass, L_P is the length of the rod and θ is the inclination of the rod.

The Taylor expansion for $\sin\theta$ when θ is small is

$$\sin\theta = \sum_{n=0}^{\infty} \frac{\left(-1\right)^n}{\left(2n+1\right)!}\theta^{2n+1} = \theta - \frac{\theta^3}{3!} + \frac{\theta^5}{5!} - \cdots. \tag{3.11}$$

Let us keep the first and third order items of Eq. (3.11) if θ is small, and therefore, Eq. (3.10) becomes

$$F_P = mg\theta - \frac{mg}{6}\theta^3 \tag{3.12}$$

Equation (3.12) can be rewritten as

$$F_P = A_{T2}\theta - B_{T2}\theta^3. \tag{3.13}$$

in which coefficients $A_{T2} = mg$ and $B_{T2} = \frac{mg}{6}$.

T2 is considered as a typical mechanical system with a softening mechanism which has the restoring force in the form of Eq. (3.13) [35].

3.1.3 Mathematical Modeling

The governing motion equation of a base-excited Duffing oscillator can be used to model certain non-linear systems in which overall stiffness does not obey Hooke's law, and is written as [50 and 51]

$$m\ddot{z} + c\dot{z} + F_r = F\cos(\omega t), \tag{3.14}$$

where z is the relative displacement, c the damping coefficient, F_r the restoring force of a Duffing oscillator, F the excitation force, ω the excitation frequency, t the oscillation time and '•' differentiation with respect to t.

Based on Eqs. (3.9) and (3.13), the restoring force of mechanical systems with hardening and softening mechanisms can be given in a general form as

$$F_r = k_1 z \pm k_2 z^3, \tag{3.15}$$

where k_1 (>0) is the linear spring constant, and k_2 (>0) the non-linear spring constant. It is called the hardening Duffing oscillator when $F_r = k_1 z + k_2 z^3$, and the softening Duffing oscillator when $F_r = k_1 z - k_2 z^3$. Most of existing non-linear vibration energy scavenging devices use the mechanical system with the hardening mechanism [29, 31 and 32].

Substituting Eq. (3.15) into Eq. (3.14) yields

$$m\ddot{z} + c\dot{z} + k_1 z \pm k_2 z^3 = F\cos(\omega t). \tag{3.16}$$

It is helpful to make Eq. (3.16) dimensionless, resulting in

$$x'' + 2\varsigma x' + x \pm \alpha x^3 = \widehat{F}\cos(\Omega\tau), \tag{3.17}$$

where $\varsigma = \frac{c}{2m\omega_n}$, $\omega_n = \sqrt{\frac{k_1}{m}}$, $\alpha = \frac{k_2 z_0^2}{k_1}$, $\Omega = \frac{\omega}{\omega_n}$, $\tau = \omega_n t$, $\widehat{F} = \frac{F}{m\omega_n^2 z_0}$, $x'' = \frac{\ddot{z}}{\omega_n^2 z_0}$, $x' = \frac{\dot{z}}{\omega_n z_0}$, $x = \frac{z}{z_0}$, z_0 is the characteristic length of the system, ω_n the natural frequency of the system when $k_2 = 0$ and ' ' ' differentiation with respect to the non-dimensional oscillation time τ.

The non-dimensional restoring force is therefore

$$\widehat{F_R} = x \pm \alpha x^3. \tag{3.18}$$

And non-dimensional stiffness $\widehat{K}$ can be obtained as

$$\widehat{K} = \frac{d\widehat{F_R}}{dx} = 1 \pm 3\alpha x^2 . \qquad (3.19)$$

3.1.4 Static Analysis

In a linear system the restoring force $\widehat{F_R} = x$ [51]. The deflection of a linear system is linearly proportional to the restoring force. Furthermore, its stiffness, $\widehat{K}$, keeps constant and is equal to 1. Therefore, in order to compare non-linear systems with the linear one, the force vs. deflection and stiffness vs. deflection relationships of the systems with hardening and softening mechanisms are considered, and plotted in Figs. 3.3 and 3.4, respectively, in which α is taken as $\alpha_1 = 0.0025$, $\alpha_2 = 0.005$ and $\alpha_3 = 0.0075$.

It can be seen in Fig. 3.3 that the restoring force and stiffness of the systems with a hardening mechanism increase with the deflection. When subjected to an identical deflection, the system with α_3 has the largest restoring force. Furthermore, stiffness is always greater than 1 which is the non-dimensional spring constant of the linear system.

The restoring force of the systems with softening mechanism increases firstly with the deflection and starts decreasing when it passes its maxima (see Fig. 3.4(a)). In contrast to the system with a hardening mechanism, with the identical deflection, the system with softening mechanism has the smallest restoring force when $\alpha = \alpha_3$. Moreover, stiffness keeps decreasing and switches sign from positive to negative when the deflection exceeds the point where the restoring force reaches its maxima (see Fig. 3.4(b)).

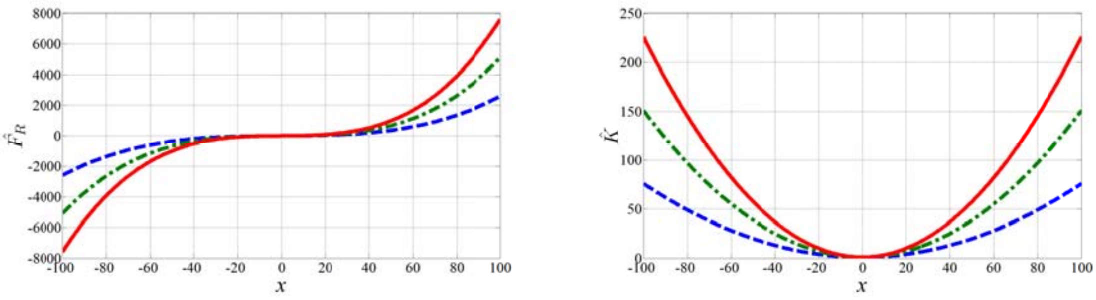

(a) **(b)**

Figure 3.3: (a) Force vs. deflection and (b) stiffness vs. deflection of systems with hardening mechanism with $\alpha_1 = 0.0025$ (blue), $\alpha_1 = 0.005$ (green) and $\alpha_1 = 0.0075$ (red).

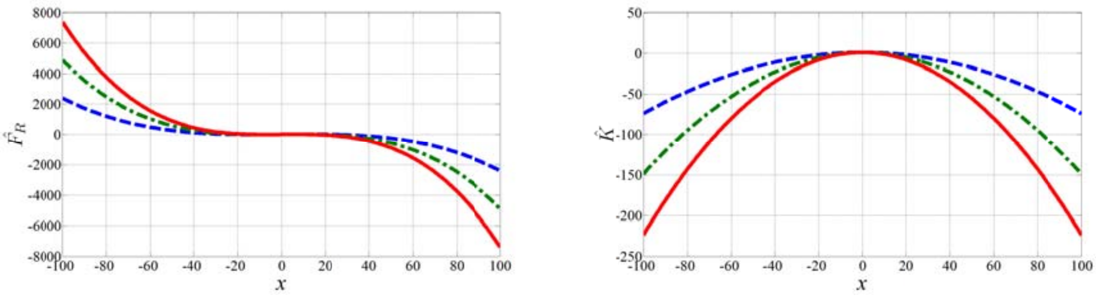

(a) **(b)**

Figure 3.4: (a) Force vs. deflection and (b) stiffness vs. deflection of systems with softening mechanism with $\alpha_1 = 0.0025$ (blue), $\alpha_1 = 0.005$ (green) and $\alpha_1 = 0.0075$ (red).

3.1.5 Dynamic Analysis

As reviewed in Chapter 2, the output power or displacement of a linear system is maximized when the excitation frequency matches the natural frequency, and drops significantly when the excitation frequency is away from the natural frequency. Are the non-linear systems different? Here we shall find out.

Simulation method

The numerical simulation (NS) method built in Matlab [33] was used to analyze the dynamic characteristics of systems with hardening and softening mechanisms. In the analysis, the excitation frequency varied from $\Omega = 0.8$ to $\Omega = 1.2$ with a step increment of 0.0001. For a given frequency, the 4th order Runge-Kutta method was adopted to solve Eq. (3.17) at every $\Omega\tau = 2n_c\pi$, where n_c was the number of oscillation cycles and up to 1000. The part with transient effects was abandoned. Peak displacements among last 100 values of solutions were saved. This process was repeated with increasing frequencies.

Dynamic analysis

A total of nine sets of coefficients ς, α and $\widehat{F}$ were considered, which are shown in Table 3.1. The frequency response curves (FRCs) of systems with hardening and softening mechanisms were obtained by using the NS method (see Figs. 3.5 – 3.7).

Table 3.1: Coefficients' sets used by the dynamic simulation of systems with hardening and softening mechanisms

Group	Set	ς	α	$\widehat{F}$
Fixed α and $\widehat{F}$	**1**	0.008	0.005	0.05
	2	0.012	0.005	0.125
	3	0.016	0.005	0.2
Fixed ς and $\widehat{F}$	**4**	0.012	0.0025	0.125
	5	0.012	0.005	0.125
	6	0.012	0.0075	0.125
Fixed ς and α	**7**	0.012	0.005	0.05
	8	0.012	0.005	0.125
	9	0.012	0.005	0.2

The effect of the damping ratio

Figure 3.5 shows the effect of the damping ratio ς when other coefficients remain fixed. The maximum displacement responses rise with the decrease in the damping ratio due to the fact that less input vibration energy is consumed by damping, and vice versa.

It can also be observed that the FRCs of systems with a hardening mechanism lean to the right of the linear resonance frequency, $\Omega = 1$. The FRCs lean to the left for the softening mechanism as shown in Figs. 3.5(a) and 3.5(b). Other dynamic behaviours of systems with hardening and softening mechanisms, including the jump-up and jump-down phenomenons, etc., will be introduced in detail in Section 3.1.6.

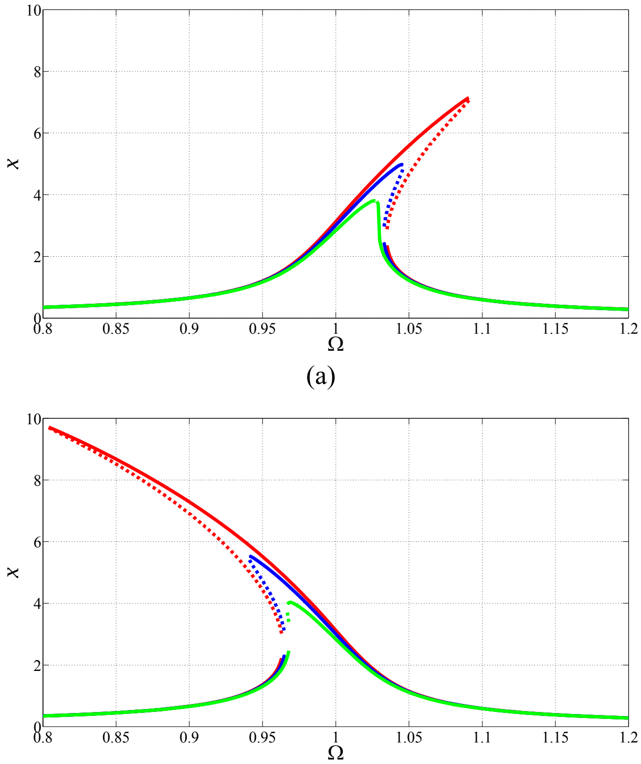

(a)

(b)

Figure 3.5: FRCs of systems with: (a) hardening mechanism, and (b) softening mechanism with coefficients' set 1 (red), set 2 (blue) and set 3 (green) as shown in Table 3.1.

The effect of non-linear spring constant

Figure 3.6 shows the effect of the non-linear spring constant α when other coefficients are fixed. It can be observed that FRCs of systems with a hardening mechanism lean over to the right more with the increase in α. However, the peak displacement in each FRC becomes smaller (see Fig. 3.6(a)), due to increasing overall stiffness shown in Fig. 3.3(b). The FRCs of the systems with a softening mechanism lean to the left. But by contrast, the peak displacement of systems with a softening mechanism increases with α because of decreasing overall stiffness (see Figs. 3.4(b) and 3.6(b)).

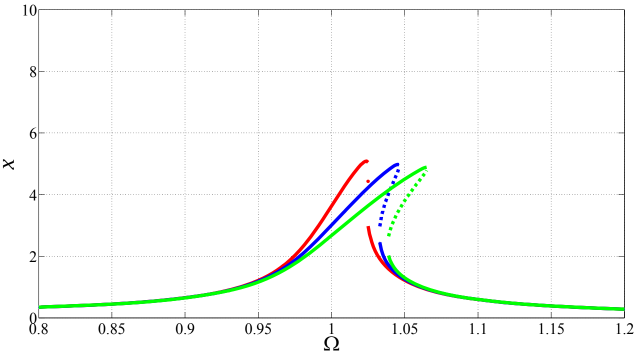

(a)

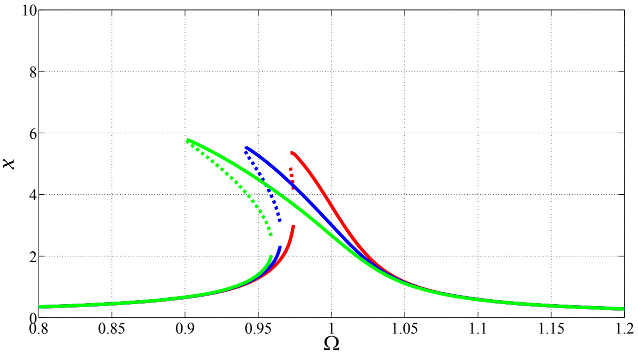

(b)

Figure 3.6: FRCs of systems with: (a) hardening mechanism, and (b) softening mechanism with coefficients' set 4 (red), set 5 (blue) and set 6 (green) as shown in Table 3.1.

The effect of the forcing amplitude

Figure 3.7 shows the effect of the forcing amplitude $\widehat{F}$ on the dynamic responses of systems with hardening and softening mechanisms, respectively, when other coefficients are fixed, which is similar to that of the damping ratio.

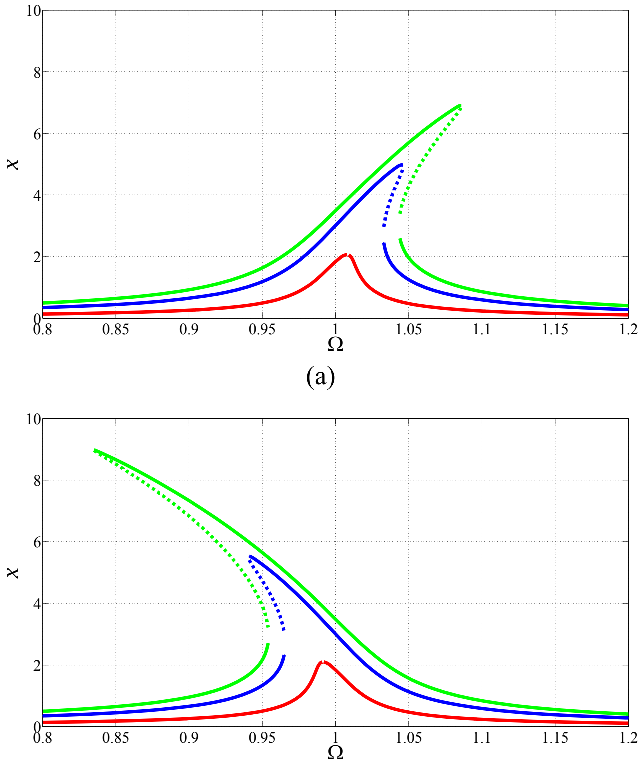

(a)

(b)

Figure 3.7: FRCs of systems with: (a) hardening mechanism, and (b) softening mechanism with coefficients' set 7 (red), set 8 (blue) and set 9 (green) as shown in Table 3.1.

3.1.6 Specific Dynamic Behaviours

The frequency response curve of the system with a hardening mechanism is shown in Fig. 3.8. When the forcing amplitude keeps constant with slowly increasing excitation frequencies, the response displacement increases from point A to Point C. And a jump occurs from point C to point E. If the driving frequency reduces slowly from point D, the other jump happens from point F to point B. Furthermore, it can be observed that the FRC has multiple response displacements between $\Omega 1$ and $\Omega 2$. It may follow BC or EF curve, determined by the initial condition, particularly the initial velocity and displacement. The dynamic responses on BC and EF curves are stable, such as point S1 and point S3, whereas those of FC curve with dash line are unstable, such as point S2 [35].

When $\varsigma = 0$ and $\widehat{F} = 0$ (free vibration), we obtain a graph of the response displacement versus the frequency which is represented by the purple curve known as the 'backbone curve' because of its shape [40]. The corresponding frequency Ω_{Fun} is called the fundamental frequency.

The system with a softening mechanism exhibits identical dynamic behaviors to the system with a hardening mechanism except that the peak tilts towards left.

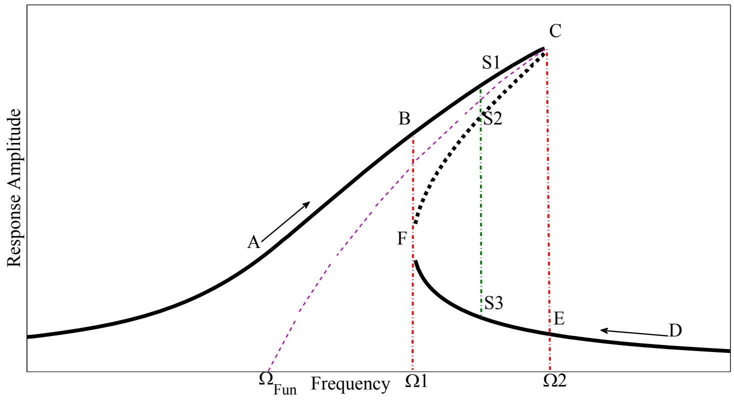

Figure 3.8: A typical FRC of the system with a hardening mechanism

3.1.7 Comparison among the Linear System and Systems with Hardening and Softening Mechanisms

Figure 3.9 shows the FRCs of the linear system and systems with hardening and softening mechanisms with identical damping ratio $\varsigma = 0.012$, non-linear spring constant $\alpha = 0.005$ and forcing amplitude $\widehat{F} = 0.125$. For the linear system, $\widehat{K} = 1$.

As mentioned in Section 2.4.2, the resonance bandwidth of the linear systems is $2\varsigma\omega_n$. Therefore, the resonance bandwidth of the above linear system is 0.024. The corresponding displacement of the starting point of resonance responses is 2.303. The frequency range in which the displacement is larger than or equal to 2.303 is considered as the operation bandwidth of systems with hardening and softening mechanisms hereafter. Therefore, operation bandwidths are 0.060 for the system with a hardening mechanism, and 0.073 for that with a softening mechanism. The respective maximum response displacement of the system with a softening mechanism is X1=5.7 and that for the system with a hardening mechanism is X3=4.9. This is due to the fact that overall stiffness of the softening mechanism is smaller than $\widehat{K}=1$ whereas that of the hardening mechanism is larger than $\widehat{K}=1$ (see Figs. 3.3(b) and 3.4(b)).

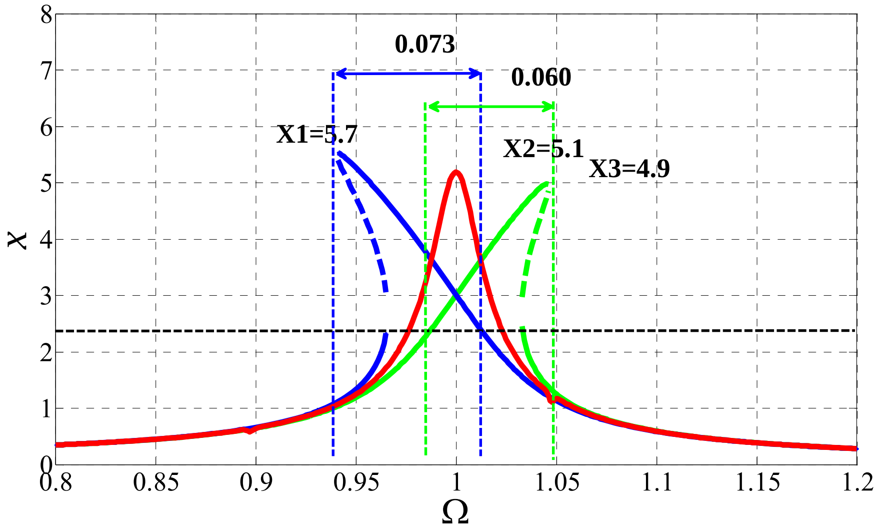

Figure 3.9: FRCs comparison of the linear system – red, systems with hardening (green), and softening (blue) mechanisms for $\varsigma=0.012$, $\alpha=0.005$ and $\widehat{F}=0.125$.

3.1.8 Limitations

System with a hardening mechanism

Due to the extra positive stiffness term introduced by the non-linear spring, the system with a hardening mechanism has lower response displacement than those of the linear system and the system with a softening mechanism when they are subjected to an identical vibration source and have the same non-linear spring constant.

System with a softening mechanism

Recalling Eq. (3.17), the motion equation of a non-dimensional softening Duffing oscillator is

$$x'' + 2\varsigma x' + x - \alpha x^3 = \widehat{F}\sin\left(\Omega\tau\right). \tag{3.20}$$

Using the harmonic balance method, the harmonic solution with the excitation frequency of Eq. (3.20) is [34, 35 and 38]

$$x = \sum_{n=1}^{N} A_n \cos\left(n\Omega\tau + \theta_n\right), \tag{3.21}$$

where N is a positive integer and $N \geq 1$, θ_n the phase angle, and A_n is the amplitude of harmonic terms.

Assuming that there is no super-harmonic response in the non-linear system, i.e., neglecting the higher order harmonic terms, Eq. (3.21) becomes

$$x = A_1 \cos\left(\Omega\tau + \theta_1\right). \tag{3.22}$$

Substituting Eq. (3.22) into Eq. (3.20), A_1 and θ_1 can be determined by the harmonic balance method, resulting in

$$A_1 = \frac{\widehat{F}}{\sqrt{\left(1-\frac{3}{4}\alpha A_1^2-\Omega^2\right)^2+4\varsigma^2\Omega^2}}, \tag{3.23}$$

and

$$\tan\theta_1 = \frac{-2\varsigma}{1-\frac{3}{4}\alpha A_1^2-\Omega^2}. \tag{3.24}$$

A_1 will be maximized when $\left(1-\frac{3}{4}\alpha A_1^2-\Omega^2\right)^2+4\varsigma^2\Omega^2$ is minimized. Hence, let

$$y_{soft}\left(\Omega\right)=\left(1-\frac{3}{4}\alpha A_1^2-\Omega^2\right)^2+4\varsigma^2\Omega^2, \tag{3.25}$$

and expanding the term in the right hand-side, we have

$$y_{soft}\left(\Omega\right)=\Omega^4+\left[4\varsigma^2-2\left(1-\frac{3}{4}\alpha A_1^2\right)\right]\Omega^2+\left(1-\frac{3}{4}\alpha A_1^2\right)^2. \tag{3.26}$$

When

$$\Omega^2=1-\frac{3}{4}\alpha A_1^2-2\varsigma^2, \tag{3.27}$$

the minimum magnitude of $y_{soft}\left(\Omega\right)$ is achieved.

Substituting Eq. (3.27) into Eq. (3.23) and rearranging terms yield

$$-\frac{3}{4}\alpha A_1^4 + \left(1-\varsigma^2\right)A_1^2 - \frac{\widehat{F}^2}{4\varsigma^2} = 0 \cdot \tag{3.28}$$

To ensure that Eq. (3.28) has the real root, there must be

$$\Delta = \left(1-\varsigma^2\right)^2 - \frac{3\alpha\widehat{F}^2}{4\varsigma^2} \geq 0. \tag{3.29}$$

As $0 < \varsigma \ll 1$, $\widehat{F} > 0$ and $\alpha > 0$, Eq. (3.29) can be further simplified to

$$\widehat{F} \leq \left(2\varsigma - 2\varsigma^3\right)\sqrt{\frac{1}{3\alpha}}. \tag{3.30}$$

Since $-\frac{3}{4}\alpha < 0$, the maximum magnitude of A_1 becomes

$$A_{1\max}^2 = \frac{2}{3\alpha}\left(1-\varsigma^2\right), \tag{3.31}$$

or

$$\left|A_{1\max}\right| = \sqrt{\frac{2}{3\alpha}\left(1-\varsigma^2\right)}, \tag{3.32}$$

Hence, the corresponding maximum displacement is

$$\left|x_{\max 1}\right| = \sqrt{\frac{2}{3\alpha}\left(1-\varsigma^2\right)}, \tag{3.33}$$

when $\cos\left(\Omega\tau + \theta_1\right) = 1$.

The FRC of the system with a softening mechanism becomes unstable when $\left|x_{\max 1}\right| > \sqrt{\frac{2}{3\alpha}\left(1-\varsigma^2\right)}$. This is because with the further increase in the response displacement, negative stiffness appears, making the restoring force act along the motion, not against. Hence, the restoring force dominated by negative stiffness affects the dynamic response of the system significantly until

$$\widehat{F_{R2}} = x - \alpha x^3 = 0, \tag{3.34}$$

or

$$\left|x_{\max 2}\right| = \sqrt{\frac{1}{\alpha}}, \tag{3.35}$$

where the time-based displacement response increase infinitely.

Furthermore, The non-dimensional potential energy of the system with a softening mechanism $\widehat{E_{soft}}$ is given by

$$\widehat{E_{soft}} = \int \widehat{F_{R2}} dx = \frac{1}{2}x^2 - \frac{1}{4}\alpha x^4 . \tag{3.36}$$

Figure 3.10 shows the potential energy-deflection curve of the system. It can be noted that the dynamic response of the system escapes from the potential energy well when the displacement exceeds $\left|x_{\max 2}\right|$. The trajectory can diverge to infinite which validates the analysis above. For a system made of known materials, this kind of behaviors has to be controlled when the system with a softening mechanism is used in scavenging devices.

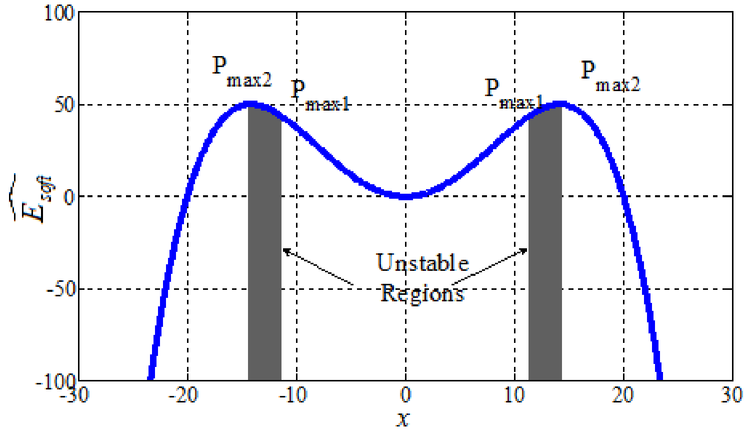

Figure 3.10: Potential energy-deflection of the system with softening mechanism with $\varsigma = 0.012$ and $\alpha = 0.005$, where the grey areas stand for the unstable regions. $P_{\max 1}$ is the point where the dynamic displacement is $\left|x_{\max 1}\right|$, and $P_{\max 2}$ is the point where the dynamic displacement is $\left|x_{\max 2}\right|$.

3.2 Snap-through mechanism

Systems with hardening and softening mechanisms have been analyzed statically and dynamically, which demonstrates that either of them could expand the operation bandwidth, and be practically constructed. However, they are impractical for a vibration energy scavenging device due to the limitations discussed above. Therefore, a snap-through mechanism is proposed with the intention to overcome these limitations.

3.2.1 Typical mechanical system with snap-through mechanism

Figure 3.11 shows a mechanical system of two linear oblique springs connected by a point mass, which will be referred to as T3 hereafter. The restoring force along the symmetry line can be given by

$$F_S = 2k_S\left(\sqrt{y_S^2 + L_{SH}^2} - L_S\right)\sin\varphi, \tag{3.37}$$

where k_S is stiffness of the spring, y_S the vertical deflection from the reference point Y_{ref} where $y_S = 0$, L_{SH} the horizontal length of the spring, L_S the original length of the spring and φ the inclination.

Since $\sin\varphi = \frac{y_S}{\sqrt{y_S^2 + L_{SH}^2}}$, Eq. (3.37) can be rewritten as

$$F_S = 2k_S\left(1 - \frac{L_S}{\sqrt{y_S^2 + L_{SH}^2}}\right)y_S\,. \tag{3.38}$$

Equation (3.38) can be expressed in a dimensionless form as

$$\widehat{F_S} = \left(1 - \frac{1}{\sqrt{x_S^2 + \lambda^2}}\right)x_S\,, \tag{3.39}$$

where $\widehat{F_S} = \frac{F_S}{2k_S L_S}$, $x_S = \frac{y_S}{L_S}$ and $\lambda = \frac{L_{SH}}{L_S}$.

Hence, non-dimensional stiffness of T3 is given by

$$\widehat{K_S} = \frac{d\widehat{F_S}}{dx_S} = 1 - \frac{\lambda^2}{\left(x_S^2 + \lambda^2\right)^{3/2}}\,. \tag{3.40}$$

T3 is considered as a typical mechanical system with a snap-through mechanism which has the restoring force in the form of Eq. (3.39) [35].

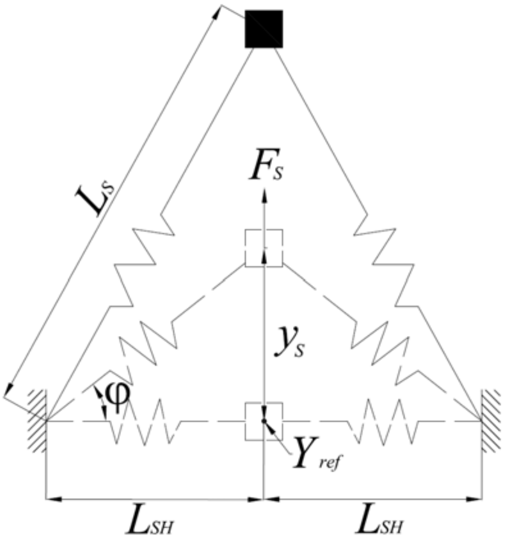

Figure 3.11: T3, where k_S is stiffness of the spring, y_S the vertical deflection from the reference point Y_{ref} where $y_S = 0$, L_{SH} the horizontal length of the spring, L_S the original length of the spring, φ the inclination and F_S the restoring force.

3.2.2 Statics Analysis

Let us consider three cases where $\lambda = 0.1$, $\lambda = 0.5$ and $\lambda = 1$, which are denoted by T3$_1$, T3$_2$ and T3$_3$, respectively. According to Eqs. (3.39) and (3.40), the non-dimensional force vs. deflection and stiffness vs. deflection curves of T3$_1$, T3$_2$ and T3$_3$ can be obtained, which are showed in Fig. 3.12.

For T3$_1$, it can be observed that three equilibrium points A, B and C exist when $\widehat{F_S} = 0$ as shown in Fig 3.12(a).The corresponding deflections can be obtained from

$$\left(1 - \frac{1}{\sqrt{x_S^2 + \lambda^2}}\right) x_S = 0, \tag{3.41}$$

which gives

$$\begin{aligned} x_{S-A} &= -\sqrt{1-\lambda^2} \\ x_{S-B} &= 0 \\ x_{S-C} &= \sqrt{1-\lambda^2} \end{aligned}. \tag{3.42}$$

According to [39], in statics, with the increase in the restoring force or input force, T3_1 follows FD curve and then directly jumps to point G once the restoring force reaches point D. With the decrease in the restoring force, T3_1 follows GE curve, and then jumps to point F as soon as the restoring force reaches point E. Therefore, the region between point D and point E is unstable. The jump phenomenon is called 'snap-through'.

As shown in Fig. 3.12(b), overall stiffness of T3_1 switches sign from positive to negative. In addition, it can be seen that stiffness of T3_1 varies very little and is close to the linear spring constant, i.e., $\widehat{K_S} = 1$, before switching sign from positive to negative.

Furthermore, it can be noted that point D and point E where the jump happens have the identical deflection magnitude to the points where $\widehat{K_S} = 0$. As discussed above, when negative stiffness appears, non-linear systems become unstable. Therefore, the point where stiffness becomes negative is called the critical point hereafter. The corresponding deflection is given by

$$1 - \frac{\lambda^2}{\left(x_S^2 + \lambda^2\right)^{3/2}} = 0. \tag{3.43}$$

which yields

$$\left|x_{S-CRI-ST}\right| = \sqrt{\lambda^{4/3} - \lambda^2}. \tag{3.44}$$

For $T3_2$, it has similar static behaviors to those of $T3_1$ except that its stiffness changes more significantly than that of $T3_1$ before switching sign.

$T3_3$ shows similar static behaviors to a system with a hardening mechanism (see Figs. 3.3 and 3.12), because the two linear springs could be considered as the fixed-fixed beam in T2. In addition, as shown in Fig. 3.12(b), overall stiffness of $T3_3$ remains positive, which means that there will be no unstable region in $T3_3$.

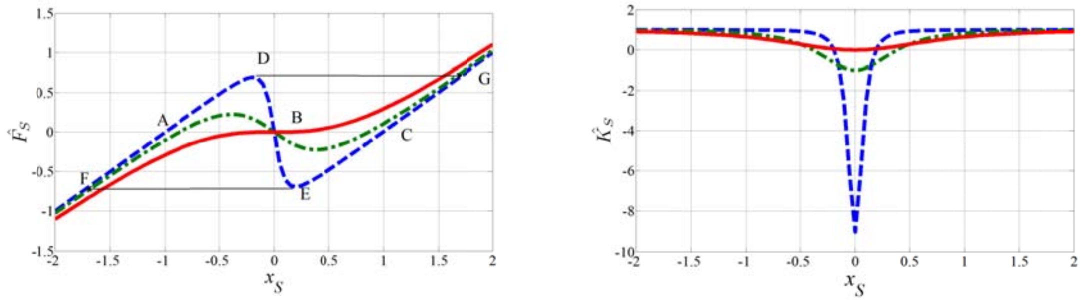

(a) (b)

Figure 3.12: (a) Force vs. deflection and (b) stiffness vs. deflection of $T3_1$ (blue), $T3_2$ (green) and $T3_3$ (red).

3.2.3 Dynamic Analysis

The elastic potential energy of T3 can be written as

$$E_{PS} = 2\left[\frac{1}{2}k_S\left(\sqrt{y_S^2+L_{SH}^2}-L_S\right)^2\right]. \tag{3.45}$$

And the non-dimensional potential energy $\widehat{E_S} = \frac{E_{PS}}{k_S L_S^2}$ is given by

$$\widehat{E_S} = \left(1-\sqrt{x_S^2+\lambda^2}\right)^2. \tag{3.46}$$

Based on Eqs. (3.42), (3.44) and (3.46), the potential energy-deflection curves of the $T3_1$, $T3_2$ and $T3_3$ are shown in Fig. 3.13.

It can be noted that two potential energy wells exist for $T3_1$ as shown in Figs. 3.13(a). Furthermore, since in dynamics the stable response of $T3_1$ is symmetrical about the equilibrium point P_{S-A} or P_{S-C} before the excitation force is large enough to cross the potential energy wells, four critical points P_{S-CRI} and three cross points P_{S-CRO} where $T3_1$ becomes unstable and crosses the potential energy wells exist, respectively [50]. Unlike the system with softening mechanism, the dynamic response of $T3_1$ does not diverge to infinite when the dynamic displacement exceeds the critical point and crosses the potential energy wells at P_{S-A} and P_{S-C}. This is due to the fact that a higher potential energy barrier appears to limit the dynamic response of $T3_1$ as shown in Fig. 3.13(a). The potential energy wells at P_{S-A} and P_{S-C} are called the Stage I potential energy wells hereafter. Furthermore, as discussed in Section 3.1.8, the symmetrical dynamic response at P_{S-A} and P_{S-C} is stable. However, the dynamic response near P_{S-B} or P_{S-CRO} is unstable (see the grey area in Fig. 3.13 (a)) [50].

For $T3_2$, it has similar potential energy-deflection curve to that of $T3_1$ except that the equilibrium points, critical points and cross points are different.

For $T3_3$, it has a unique potential well. Therefore, no critical point or cross point exist. P_{S-B} is the unique stable equilibrium point.

Table 3.2 lists the corresponding displacements of the critical points and cross points of $T3_1$, $T3_2$ and $T3_3$.

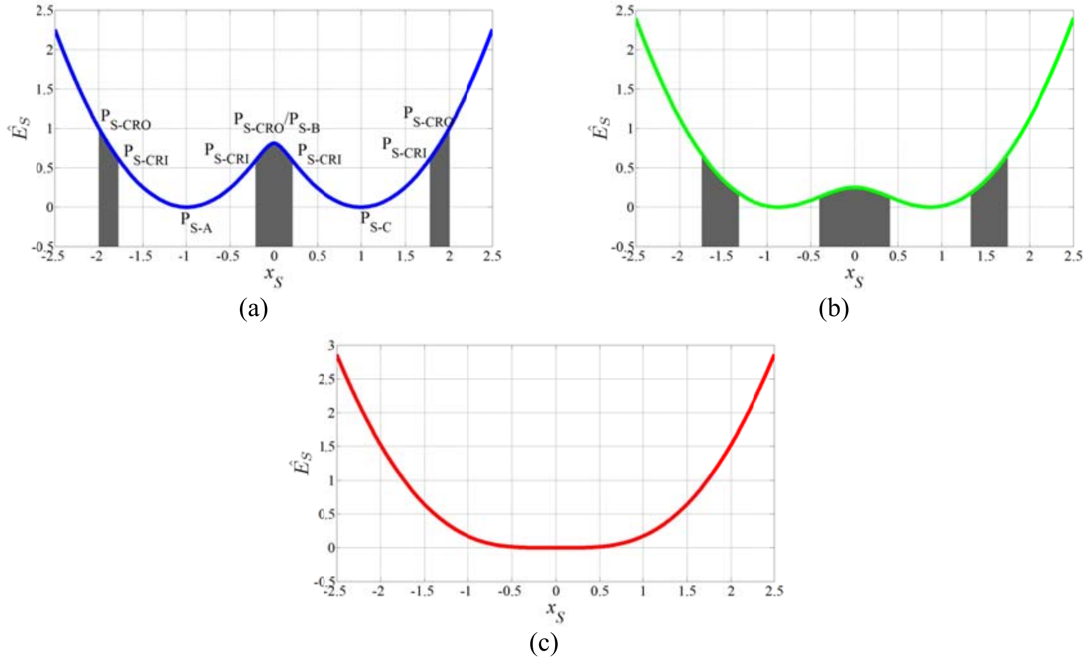

(a)

(b)

(c)

Figure 3.13: Potential energy vs. deflection curves: (a) T3$_1$, (b) T3$_2$ and (c) T3$_3$, where the grey areas stand for the unstable regions. P_{S-A} and P_{S-C} are the stable equilibrium points, P_{S-B} is the unstable equilibrium point which is the same point as P_{S-CRO} in the middle of the curve, P_{S-CRI} is the critical point and P_{S-CRO} is the cross point.

Table 3.2: Displacement values at the critical points and cross points of T3$_1$, T3$_2$ and T3$_3$.

Non-linear system	Critical point displacement 1 $\left\|x_{S-CRI-1}\right\|$	Critical point displacement 2 $\left\|x_{S-CRI-2}\right\|$	Cross point displacement 1 $\left\|x_{S-CRO-1}\right\|$	Cross point displacement 2 $\left\|x_{S-CRO-2}\right\|$
T3$_1$	1.799	0.191	1.990	0
T3$_2$	1.349	0.383	1.732	0
T3$_3$	N/A	N/A	N/A	N/A

To validate the discussion above, T3$_1$ and T3$_2$ are selected for in depth analysis. According to Eqs. (3.17) and (3.39), the motion equation of T3 is

$$x_S'' + 2\varsigma x_S' + \left(1 - \frac{1}{\sqrt{x_S^2 + \lambda^2}}\right) x_S = \widehat{F}\sin\left(\Omega\tau\right). \tag{3.47}$$

The NS method introduced earlier is used to solve Eq. (3.47). Let Ω vary from 0.1 to 2.5 with a step increment 0.0025. Figures 3.14 – 3.16 show the FRCs of T3$_1$ and T3$_2$

when subjected to various $\widehat{F}$ and ς. In the figures, smooth curves represent stable periodic responses, and dispersed points represent unstable chaotic responses. In order to understand the dynamic behaviours of $T3_1$ and $T3_2$ clearly, the corresponding time based displacement responses and phase figures are also given near the fundamental frequencies, which $\Omega_{Fun} = 1$ for $T3_1$, and $\Omega_{Fun} = 0.8$ for the $T3_2$.

Effect of the forcing amplitude

$\underline{\widehat{F} = 0.05}$

For $T3_1$, the FRC leans to the left of the linear resonance frequency $\Omega = 1$ when $\varsigma = 0.04$, which is identical to that of a system with a softening mechanism shown in Fig. 3.14(a). It is because the maximum displacement is 1.895, which exceeds displacement $\left| x_{S-CRI-1} \right| = 1.799$ of the critical point but is below displacement $\left| x_{S-CRO-1} \right| = 1.990$ of the cross point. Therefore, negative stiffness shows up that renders $T3_1$ to a softening mechanism. In addition, unstable chaotic responses can also be observed. It is due to the fact that the dynamic responses of $T3_1$ around the fundamental frequency have entered the unstable regions as shown in Fig. 3.13(a). When $\varsigma = 0.06$ and $\varsigma = 0.08$, the maximum displacements are smaller than 1.799. Stiffness of $T3_1$ is close to the linear spring constant $\widehat{K_S} = 1$ before the dynamic response exceeds the critical point. Therefore, $T3_1$ demonstrates similar dynamic behaviors to that of a linear system (see Figs. 3.14(b) and (c)).

For $T3_2$, the FRC leans to the left of the linear resonance frequency $\Omega = 1$ when $\varsigma = 0.04$, which is identical to that of a system with softening mechanism shown in Fig.

3.14(a). This is due to the fact that the maximum displacement exceeds displacement $\left|x_{S-CRI-1}\right|=1.349$ of the critical point but is below displacement $\left|x_{S-CRO-1}\right|=1.732$ of the cross point when $\varsigma=0.04$. When $\varsigma=0.06$ and $\varsigma=0.08$, the maximum displacements are smaller than $\left|x_{S-CRI-1}\right|=1.349$. However, both FRCs leans to the left of the linear resonance frequency. It is because stiffness of T3$_2$ has a significant decrease before switching sign from positive to negative, similar to that of the softening mechanism shown in Fig. 3.4.

Based on the analysis above, it can be concluded that $\widehat{F}=0.05$ is not large enough to allow T3$_1$ and T3$_2$ to cross the Stage I potential energy wells. This is confirmed by Figs. 3.17 and 3.20 in which the mass keeps oscillating about one of the two stable equilibrium points periodically.

$\underline{\widehat{F}=0.125}$

As shown in Fig. 3.15, T3$_1$ and T3$_2$ show significantly unstable chaotic responses when the excitation frequencies are close to the fundamental frequencies. This is due to the fact that the maximum displacements of T3$_1$ and T3$_2$ for given damping ratio are larger than the corresponding displacements of the critical points, which are 1.799 for T3$_1$ and 1.349 for T3$_2$, but are smaller than those of the cross points, which are 1.990 for T3$_1$ and 1.732 for the T3$_2$. Additionally, because of the relatively large restoring force accompanied by a negative stiffness, response displacements of T3$_1$ are larger than those of T3$_2$ near resonance frequencies. As shown in Figs. 3.18(a) and (c) and 3.21(a), when the excitation frequency is below the fundamental frequency, the mass oscillates about one of the two stable equilibrium points P_{S-A} and P_{S-C} periodically. When the excitation frequency is close to the fundamental frequency, the mass oscillates about the two stable equilibrium points alternately as shown in Figs. 3.18(e) and 3.21(b). In addition, no trajectory that crosses the equilibrium point P_{S-B} can be seen in Figs. 3.18(f) and 3.21(d), which shows that P_{S-B} is unstable. With further increase in the excitation frequency, the response returns to periodical oscillations about a stable equilibrium point (see Figs 3.18(g) and 3.21(e) and (g)).

$\underline{\widehat{F} = 0.2}$

As shown in Fig. 3.16, T3$_1$ still shows significantly unstable chaotic responses around the fundamental frequency even though its maximum displacement has exceeded the corresponding displacement of the cross point. It can be understood with the assistance of Figs. 3.19(c) and (e). In Figs. 3.19(c) and (e), it can be seen that the most of peak displacements in each cycle remain smaller than $\left|x_{S-CRO-1}\right|$. Therefore, T3$_1$ cannot overcome the Stage I potential energy wells completely. When $\Omega = 1.5$, the response returns to periodical oscillation about a stable equilibrium point with the decrease in the displacement (see Fig. 3.19(g)).

In contrast to T3$_1$, when $\widehat{F} = 0.2$, the fundamental frequency of T3$_2$ becomes smaller and is approximately 0.4. When the excitation frequency is close to the fundamental frequency, the jump-up phenomenon followed by the right leaning of the FRCs can be observed. This is because all peak displacements are larger than the corresponding displacement of the critical point (see Fig. 3.22(a)). Therefore, T3$_2$ has crossed the

Stage I potential energy well, and begun oscillating periodically about the equilibrium point P_{S-B} (see Fig. 3.22 (b)). Therefore, $T3_2$ shows similar dynamic behaviors to those of the hardening mechanism when the Stage I potential energy well is crossed. When $\Omega = 0.7$ the dynamic response of $T3_2$ becomes unstable due to the decrease in the response displacement. With the further increase in the excitation frequency, the response returns to periodical oscillation about a stable equilibrium point.

In summary, when $\widehat{F} = 0.2$, a system with a snap-through mechanism with a relatively low nonlinearity, such as $T3_2$, is more likely to cross the Stage I potential energy well and exhibits similar dynamic behaviors to those of a system with a hardening mechanism. This applies to all systems with a snap-through mechanism [50].

Effect of the damping ratio

As shown in Fig. 3.14, the unstable chaotic responses appear when the damping ratio is relatively small, e.g., $\varsigma = 0.04$. If the damping ratio increases, the dynamic response tend to be more settled, which indicates that the increasing damping restricts the oscillation of the mass about one of the stable equilibrium points.

3.2.4 Practical Constraints of the Typical Mechanical System

T3 shown in Fig. 3.11 is difficult to be used directly in a vibration energy scavenging devices because it is hard to be incorporated into the existing transduction mechanisms. This problem can be solved by replacing the two oblique linear springs in T3 with two rectangular beams upon which the piezoelectric transduction mechanism can be attached. But this brings another problem. The beams may buckle which are compressed in practical [40].

3.3 Summary

In the chapter hardening and softening mechanisms were firstly examined both statically and dynamically based on the corresponding typical mechanical systems, T1 and T2. The NS method was used to investigate the effects of the damping ratio, the non-linear spring constant and the forcing amplitude on the dynamic response of these non-linear systems. The main findings are as follows:

- The FRCs of the systems with a hardening mechanism leaned to the right of the linear resonance frequency. The maximum response displacement rises with the decrease in the damping ratio because less input vibration energy was consumed by damping. Moreover, the FRCs leaned over to the right with the increase in the non-linear spring constant. Meanwhile, the response displacement becomes smaller due to increasing overall stiffness introduced by the non-linear spring constant.
- The FRCs of the systems with a softening mechanism leaned to the left of the linear resonance frequency. In contrast to the systems with a hardening mechanism, the response displacement of the systems with a softening mechanism becomes larger with the increase in the non-linear spring constant due to decreasing overall stiffness.

Operation bandwidths of systems with hardening and softening mechanisms are wider than the half-power bandwidth of a linear system when subjected to identical damping and forcing amplitude. Moreover, because of comparatively low overall stiffness, the systems with a softening mechanism exhibit higher response displacements. However, the systems with a softening mechanism become extremely unstable when the response displacement exceeds the maximum displacement allowed where negative stiffness influences greatly the dynamic response.

Therefore, the snap-through mechanism is introduced with the intention to overcome the limitations of hardening and softening mechanisms. The static and dynamic analysis of the typical mechanical system with a snap-through mechanism, T3, shows that:

- With the proper selection of the nonlinearity, T3 exhibits softening dynamic characteristics when the excitation force is relatively small, and hardening dynamic characteristics when the excitation force is large enough to enable the system cross the Stage I potential energy barrier. Thus, the systems with a snap-through mechanism can broaden operation bandwidth.
- T3 overcomes the limitations of both the system with a hardening mechanism, that is, comparatively low response displacement, and the softening mechanism, that is, increasing infinitely when the dynamic response exceeds the maximum displacement allowed.

However, T3 cannot be a suitable design for the vibration energy scavenging device due to practical constrains. Therefore, in Chapter 4, a new mechanical system design based on the snap-through mechanism will be proposed.

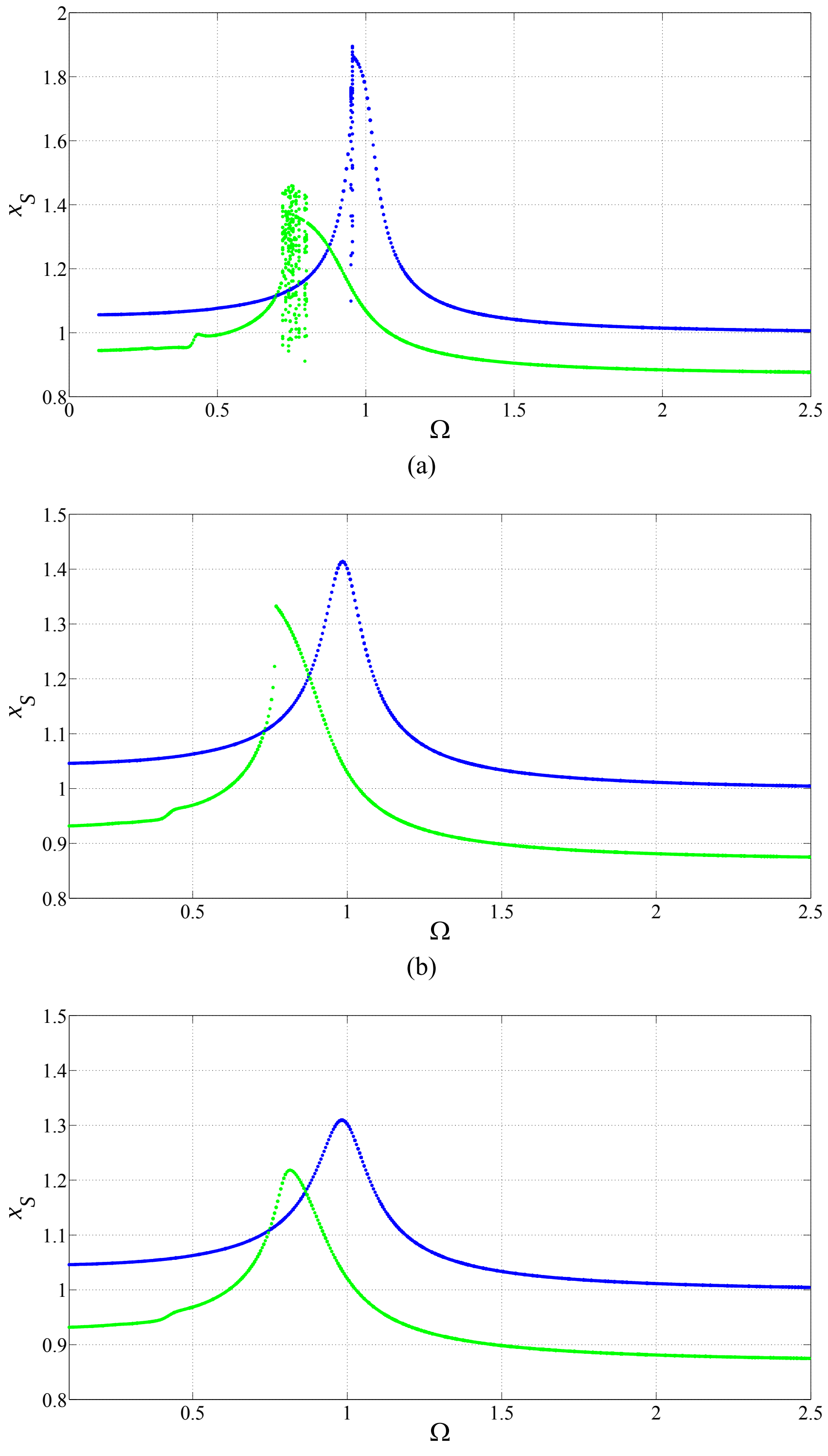

(a)

(b)

(c)

Figure 3.14: FRCs of T3$_1$ (blue) and T3$_2$ (green) when $\widehat{F} = 0.05$ **. (a)** $\varsigma = 0.04$ **, (b)** $\varsigma = 0.06$ **and (c)** $\varsigma = 0.08$ **.**

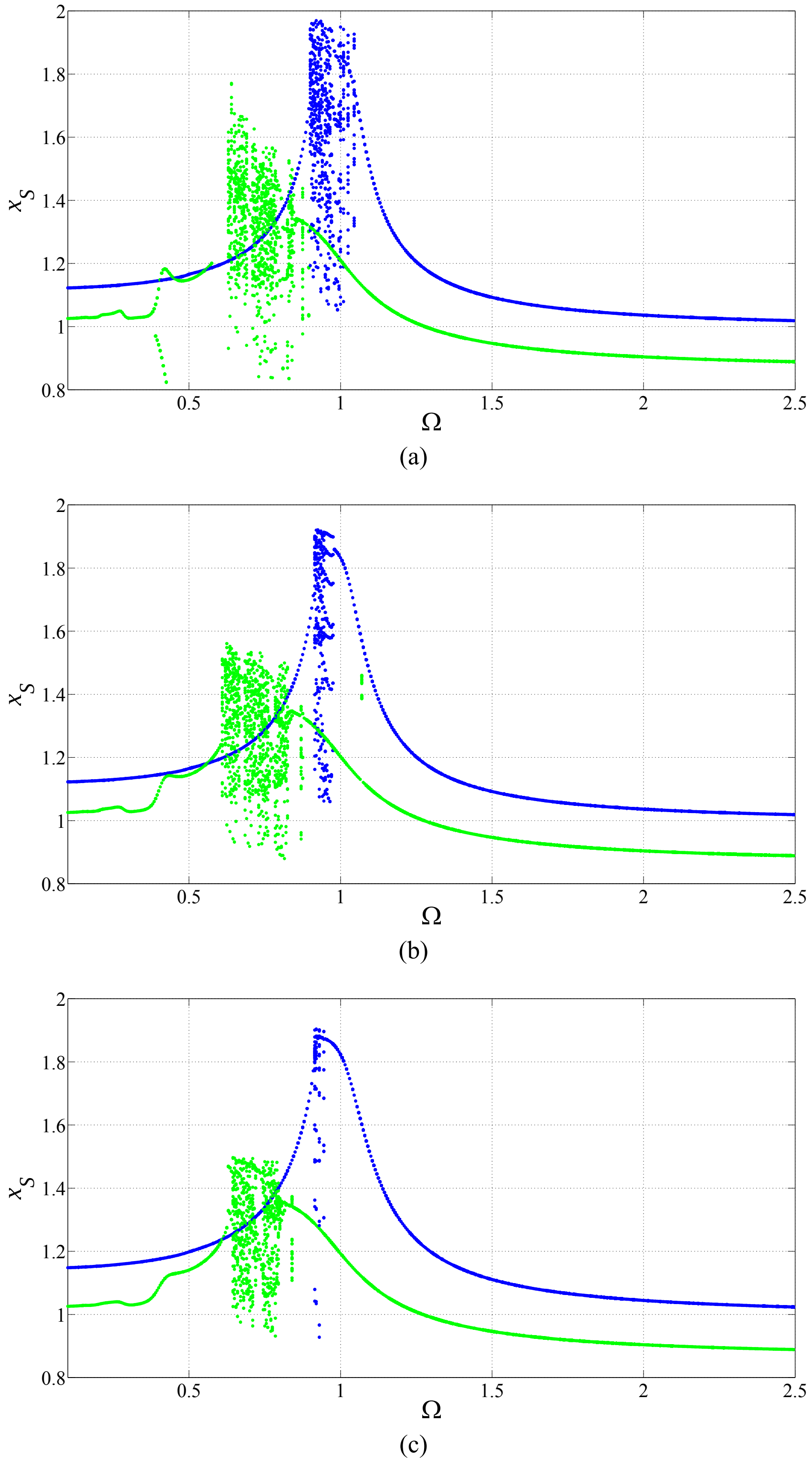

(a)

(b)

(c)

Figure 3.15: FRCs of T3$_1$ (blue) and T3$_2$ (green) when $\widehat{F} = 0.125$ **. (a)** $\varsigma = 0.04$ **, (b)** $\varsigma = 0.06$ **and (c)** $\varsigma = 0.08$ **.**

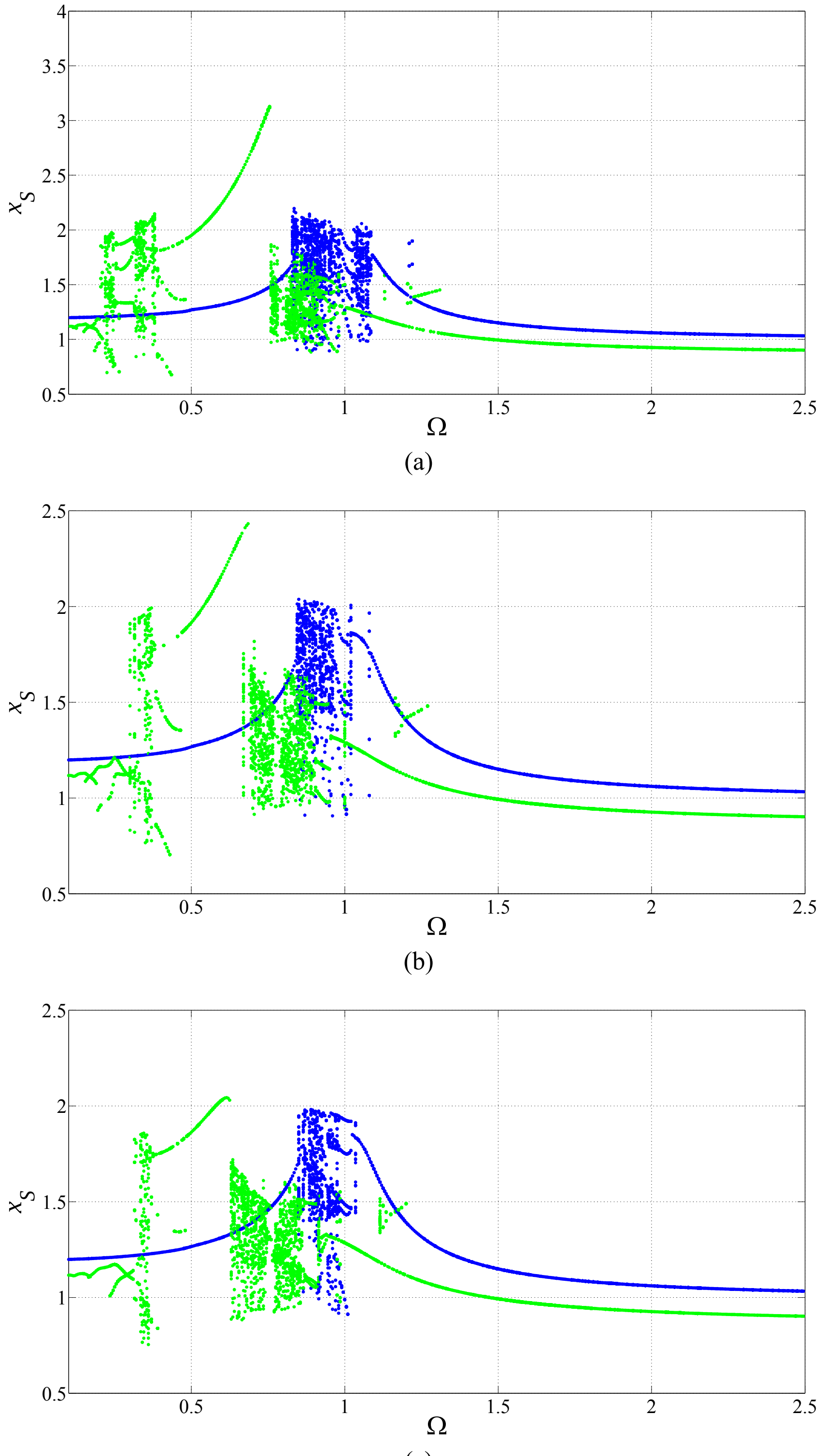

Figure 3.16: FRCs of T3$_1$ (blue) and T3$_2$ (green) when $\widehat{F} = 0.2$. (a) $\varsigma = 0.04$, (b) $\varsigma = 0.06$ and (c) $\varsigma = 0.08$.

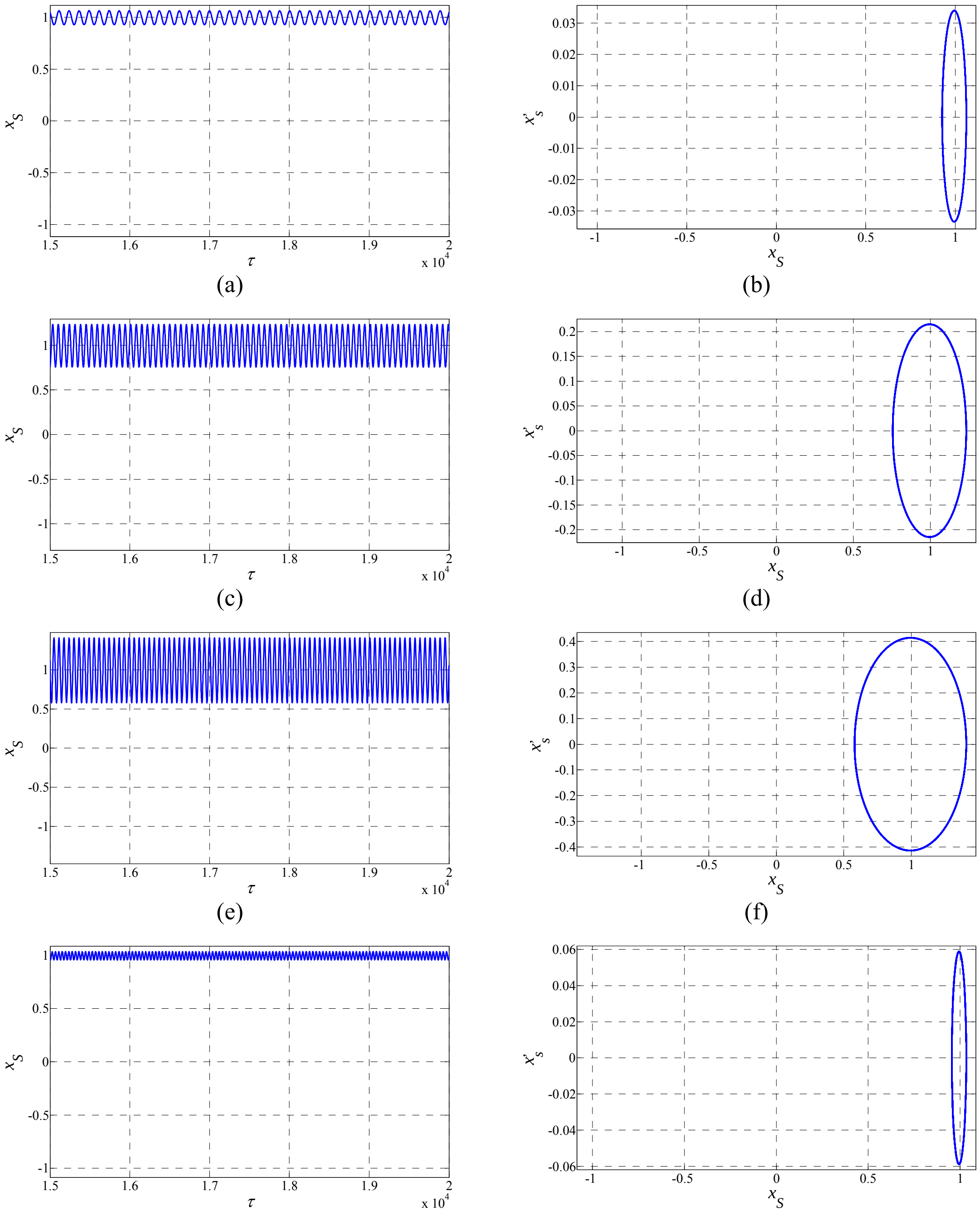
(a) (b) (c) (d) (e) (f) (g) (h)

Figure 3.17: Time-based displacement responses (1st column) and the phase diagrams (2nd column) of T3$_1$ when $\widehat{F} = 0.05$ and $\varsigma = 0.06$. (a, b) $\Omega = 0.5$, (c, d) $\Omega = 0.9$, (e, f) $\Omega = 1$ and (g, h) $\Omega = 1.5$.

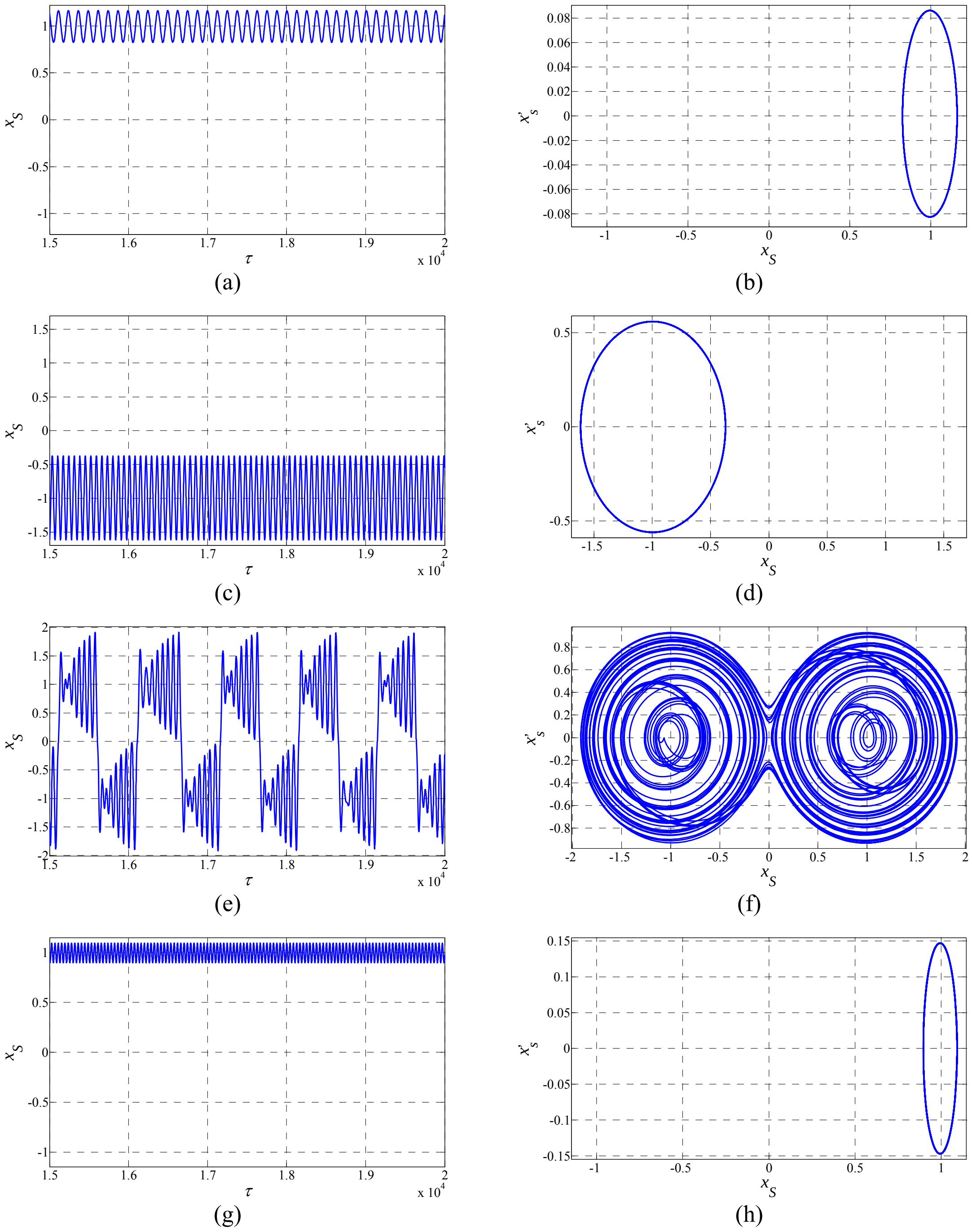

Figure 3.18: Time-based displacement responses (1st column) and the phase diagrams (2nd column) of T3$_1$ when $\widehat{F}=0.125$ and $\varsigma=0.06$. (a, b) $\Omega=0.5$, (c, d) $\Omega=0.9$, (e, f) $\Omega=1$ and (g, h) $\Omega=1.5$.

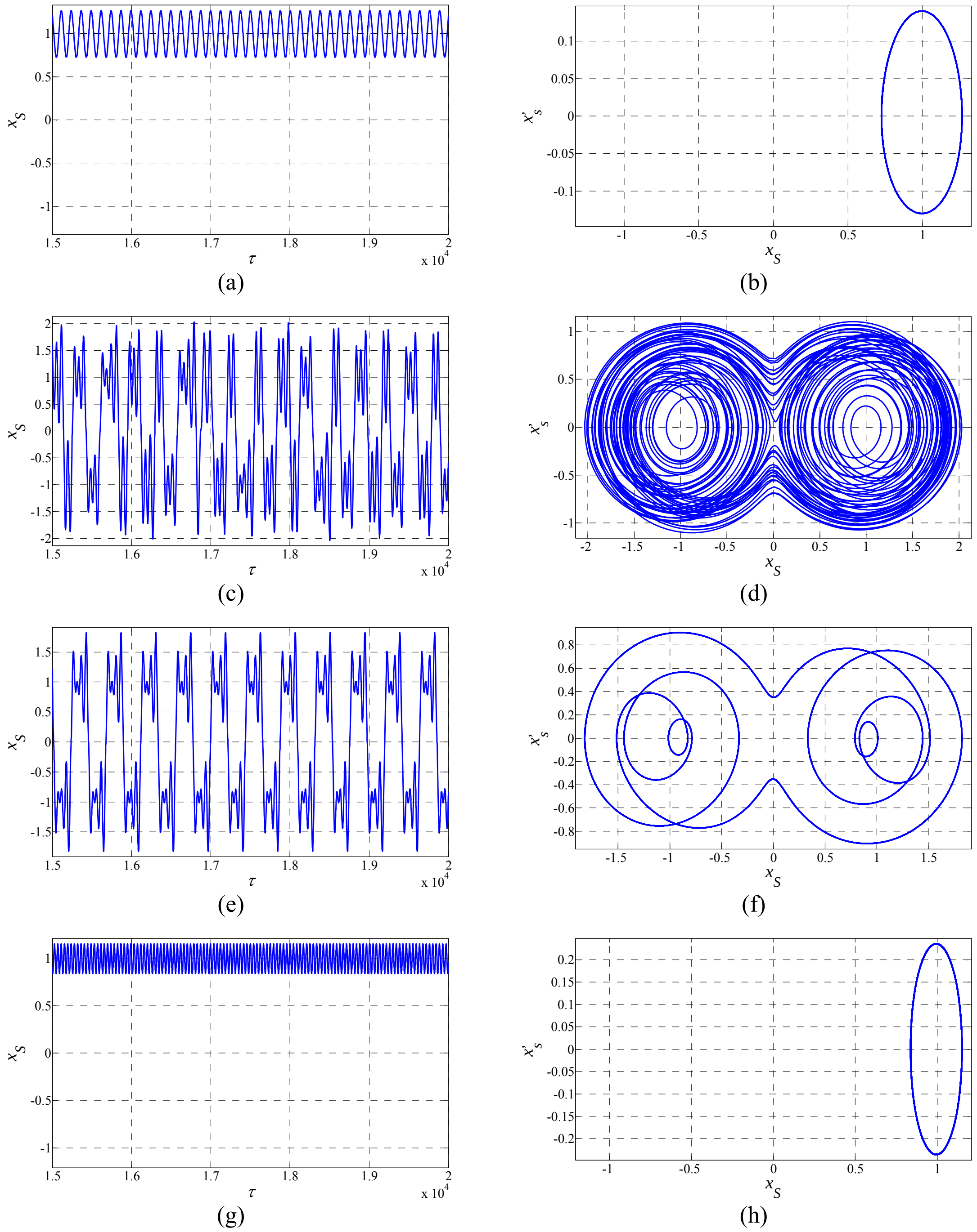

Figure 3.19: Time-based displacement responses (1st column) and the phase diagrams (2nd column) of T3$_1$ when $\widehat{F} = 0.2$ and $\varsigma = 0.06$. (a, b) $\Omega = 0.5$, (c, d) $\Omega = 0.9$, (e, f) $\Omega = 1$ and (g, h) $\Omega = 1.5$.

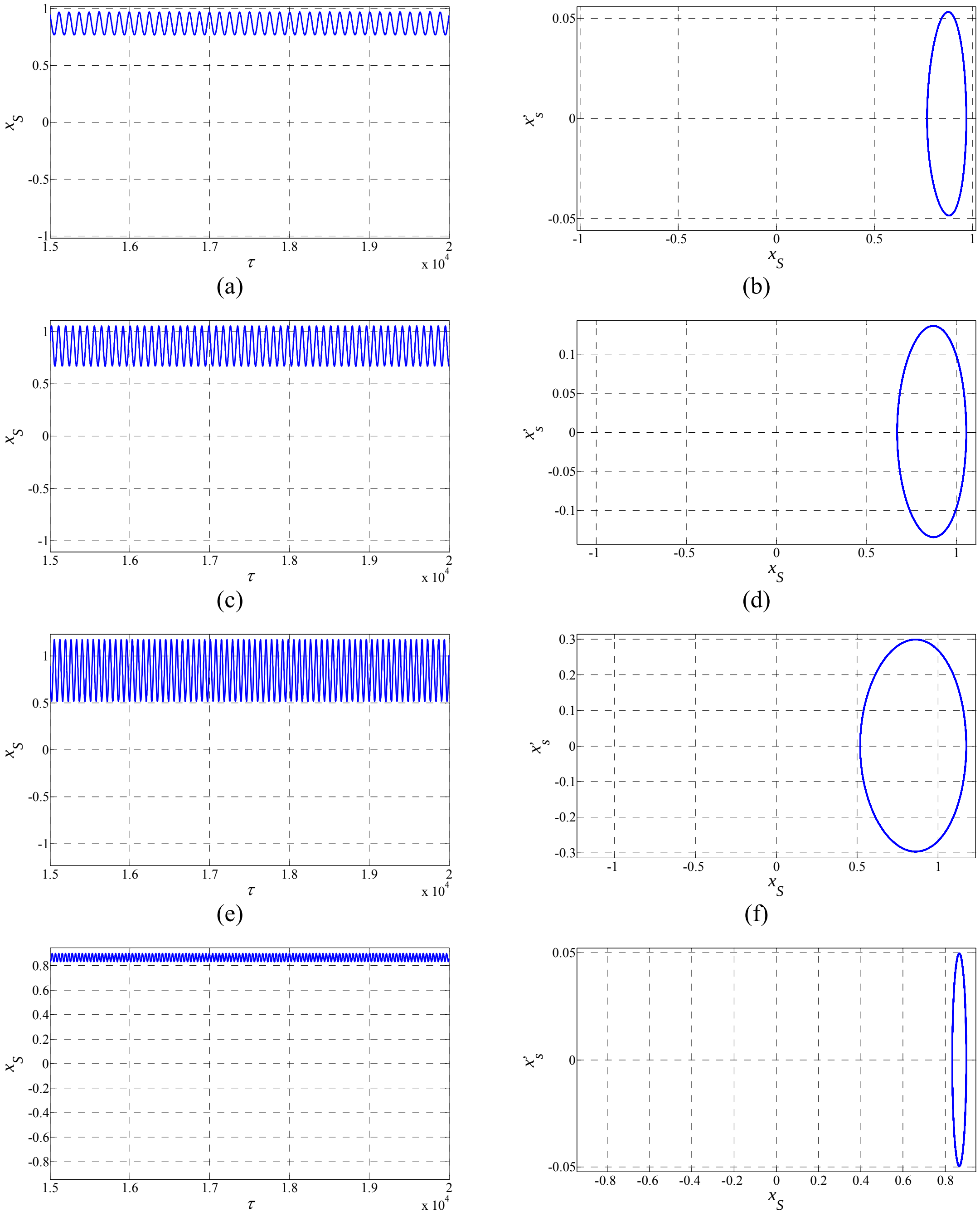

(a) (b)

(c) (d)

(e) (f)

(g) (h)

Figure 3.20: Time-based displacement responses (1st column) and the phase diagrams (2nd column) of T3$_2$ when $\widehat{F} = 0.05$ and $\varsigma = 0.06$. (a, b) $\Omega = 0.5$, (c, d) $\Omega = 0.7$, (e, f) $\Omega = 0.8$ and (g, h) $\Omega = 1.5$.

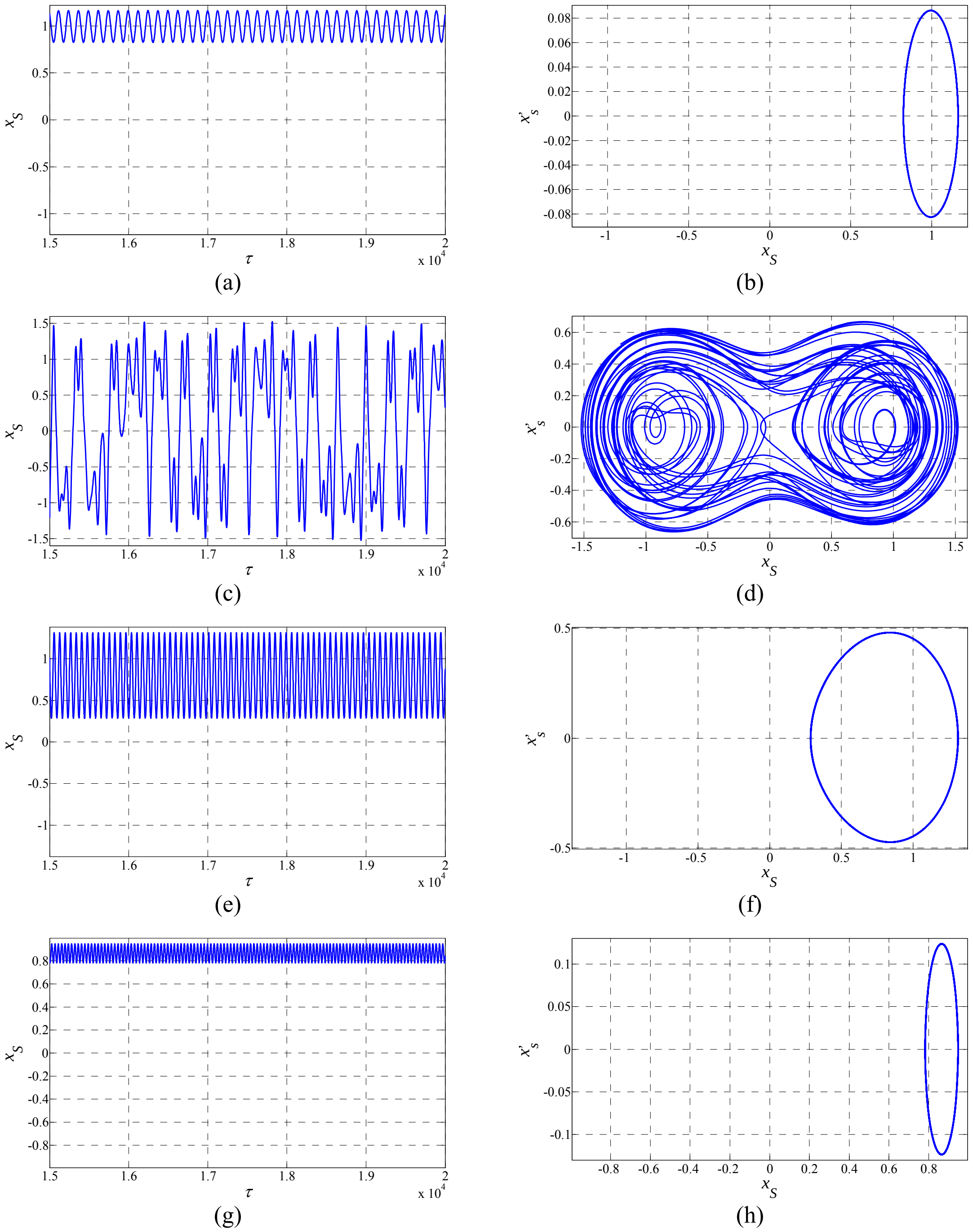

(a) (b) (c) (d) (e) (f) (g) (h)

Figure 3.21: Time-based displacement responses (1st column) and the phase diagrams (2nd column) of T3$_2$ when $\widehat{F} = 0.125$ and $\varsigma = 0.06$. (a, b) $\Omega = 0.5$, (c, d) $\Omega = 0.7$, (e, f) $\Omega = 0.8$ and (g, h) $\Omega = 1.5$.

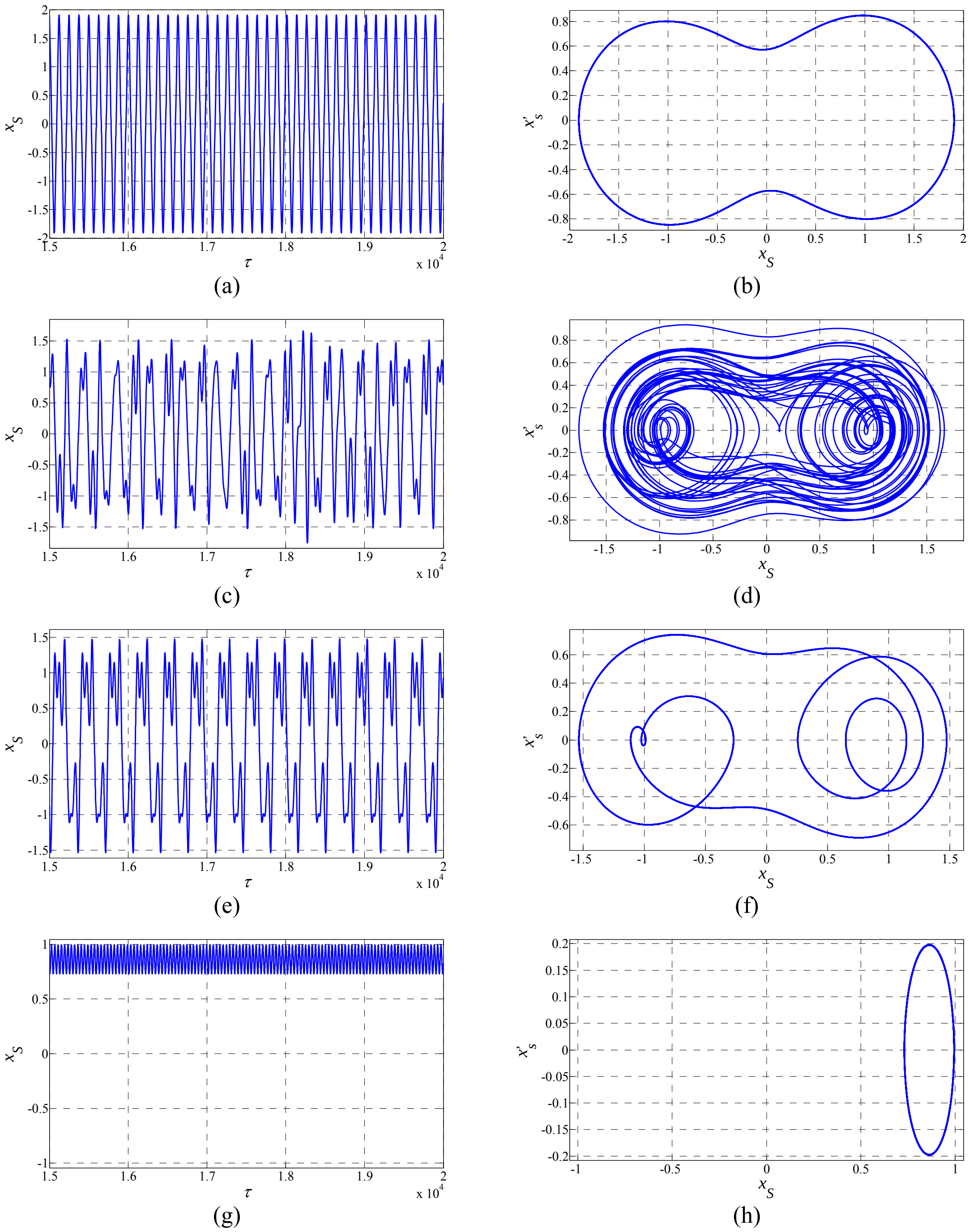

(a) (b) (c) (d) (e) (f) (g) (h)

Figure 3.22: Time-based displacement responses (1st column) and the phase diagrams (2nd column) of T3$_2$ when $\widehat{F} = 0.2$ and $\varsigma = 0.06$. (a, b) $\Omega = 0.5$, (c, d) $\Omega = 0.7$, (e, f) $\Omega = 0.8$ and (g, h) $\Omega = 1.5$.

CHAPTER 4 NEW NON-LINEAR MECHANICAL SYSTEMS

This chapter introduces a new mechanical system based on the snap-through mechanism. The first design is referred to as the N1 hereafter. The dimensional parameters and physical properties of materials in N1 are presented, followed by its static and dynamic behaviors in two geometrical configurations. Experiments have been conducted to verify the accuracy of the simulation result. The discussion on advantages and disadvantages of N1 results an improved structural design known as N2. N2 is subsequently integrated with a piezoelectric transduction mechanism to complete a new piezoelectric non-linear vibration energy scavenging device. This device, known as ND, has then been statically analyzed. A piezoelectric mechanical and electrical domains dynamic coupling model is used to simulate the output voltage and power of ND when subjected to various input accelerations and increasing frequencies. A series of experiments have been conducted to validate the numerical simulation result.

4.1 Design I

4.1.1 Model

Figure 4.1 shows the 3D model of N1 which consists of a beryllium copper shim of thickness $d_{\mathrm{I}1} = 0.3$ mm bonded by two aluminum alloy blocks of depth $d_{\mathrm{I}2} = 5$ mm, which acts like a lumped mass. The central shim has four identical beams of length $L_{DCB} = 35$ mm (see Fig. 4.2). The far end of each beam is rigidly fixed to the enclosure by a column of width $w_{column} = 5$ mm and length $l_{column} = 8$ mm. Six N42 permanent cylindrical magnetic buttons of diameter $\Phi = 15$ mm and thickness $d_{13} = 2$ mm are used in the design, four of which are fixed into the lumped mass. And the rest are attached into the center of the top and the bottom of the enclosure, respectively. The buttons are vertically aligned. Dimensional parameters of the central shim and the alloy block are shown in Fig. 4.2. Physical properties of the corresponding materials are listed in Table 4.1.

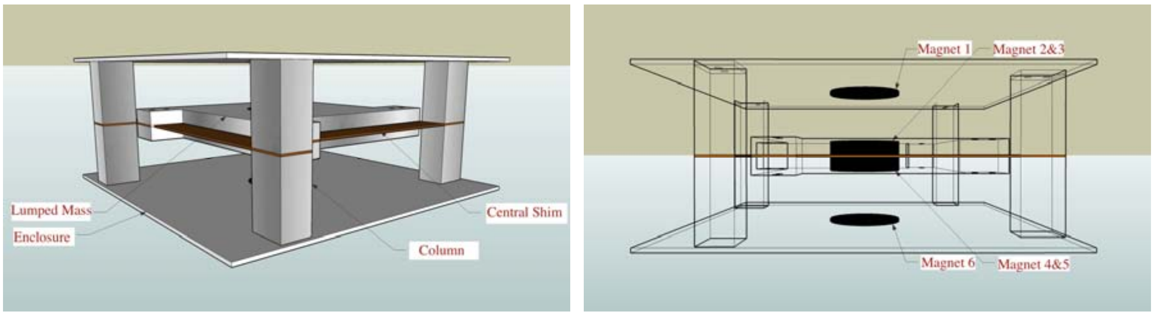

(a) (b)

Figure 4.1: The 3D model of N1: (a) isometric view of N1 and (b) arrangement of magnets.

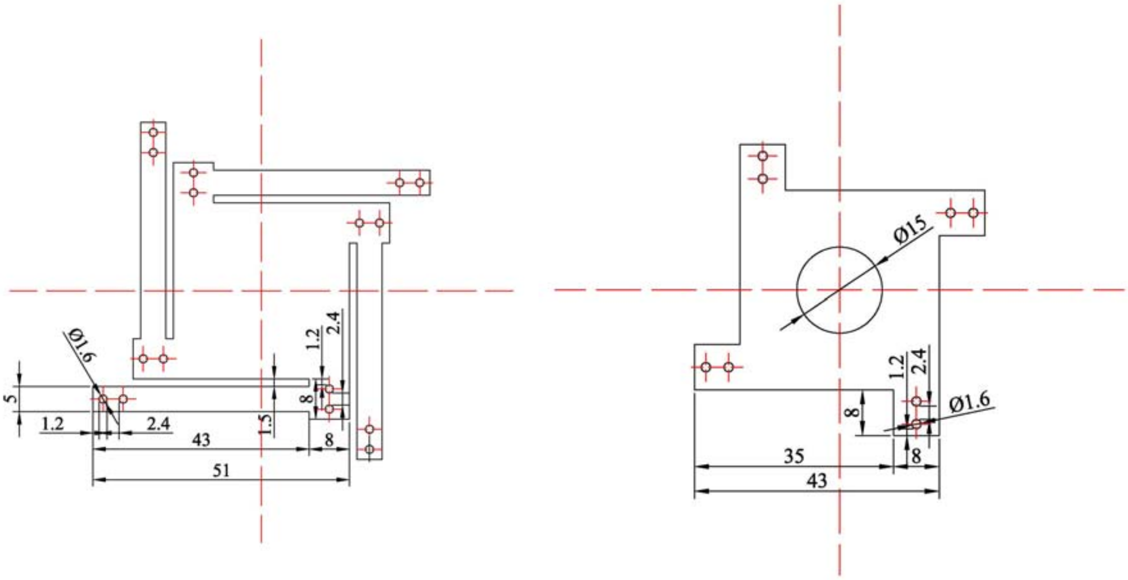

(a) (b)

Figure 4.2: Design of (a) the central shim, and (b) the top and bottom alloy blocks forming the lumped mass in N1. Unit: mm.

Table 4.1: Physical properties of materials

Symbol	Description	Value
B_r	Residual flux density	1.18 T
μ_0	Permeability of intervening medium	1.25×10^{-6} H/m
ρ_m	Density of the magnet	7.5×10^{3} kg/m^3
ρ_b	Density of the beryllium copper shim	8.25×10^{3} kg/m^3
ρ_a	Density of the aluminum alloy block	2.7×10^{3} kg/m^3
E_b	Young's modulus of the beryllium copper shim	1.23×10^{11} N/m^2
σ_b	Yield strength of the beryllium copper shim	8.84×10^{8} N/m^2

4.1.2 Static Analysis

Doubly clamped beams

The beams linking the lumped mass and columns can be treated as fixed-fixed beams, and will be referred to as the doubly clamped beams hereafter. Recalling Eq. (3.8), the relationship between the force and the deflection of each doubly clamped beam can be written as

$$F_{EDCB} = \frac{12E_b I_{DCB}}{L_{DCB}^3} z + \frac{A_{DCB} E_b \pi^2}{16L_{DCB}^3} z^3, \tag{4.1}$$

where I_{DCB} is the second moment area of the doubly clamped beam, A_{DCB} is the cross-section area of the doubly clamped beam, and z is the deflection of the doubly clamped beam.

According to Eqs. (3.6) and (3.7), the force due to tension is

$$F_{EDCB1} = \frac{A_{DCB} E_b \pi^2}{16L_{DCB}^3} z^3, \tag{4.2}$$

and due to bending is

$$F_{EDCB2} = \frac{12E_b I_{DCB}}{L_{DCB}^3} z. \tag{4.3}$$

The total restoring force of N1, F_{IE}, is

$$F_{\mathrm{IE}} = 4F_{EDCB} = \frac{48E_b I_{DCB}}{L_{DCB}^3} z + \frac{A_{DCB} E_b \pi^2}{4L_{DCB}^3} z^3, \tag{4.4}$$

because there are four identical doubly clamped beams.

In order to verify the accuracy of Eq. (4.1), Abaqus FEA 6.7 [41] was used to model the force-deflection behavior of each doubly clamped beam. Figure 4.3(a) shows the comparison between the numerical result of Abaqus and that of Eq. (4.1). It can be seen that both coincide well. It is also found that, with the suitable selection of materials and sectional geometries, tension could dominate the force vs. deflection behavior of the doubly clamped beam, which is the case here (see in Fig. 4.3 (b)).

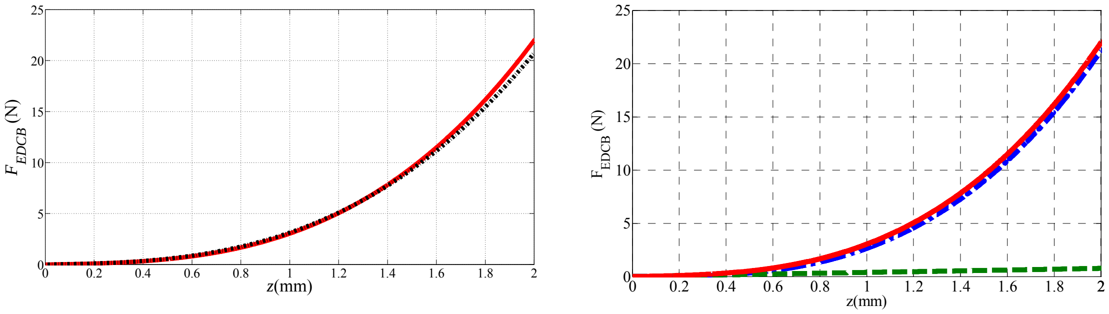

(a) (b)

Figure 4.3: Force vs. deflection diagrams of the doubly clamped beam. (a) Eq. (4.1) and Abaqus simulation, (b) Eq. (4.1), Eq. (4.2) and Eq. (4.3). In the diagrams, Eq. (4.1) (red), Eq. (4.2) (blue), Eq. (4.3) (green), and Abaqus FEA (black).

Magnets and Magnetic Force

The Finite Element Method Magnetic 4.2 (FEMM) [43] has been used to simulate the force-distance relationship between two N42 cylindrical magnetic buttons by adopting the dimensional parameters and physical properties of the circular magnets given above (see Fig. 4.4). The accuracy of FEMM has been verified by the official data posted by the supplier of the N42 circular magnets. Moreover, in order to analyze the dynamic response of N1 through the NS method, SPSS Statics [45] was used to generate the fitting formula, representing the relationship between the magnetic force and displacement, based on the output from FEMM, which can be expressed as

$$F_{TVACM} = A_{TM} - B_{TM} d_{TM} + C_{TM} d_{TM}^2 - D_{TM} d_{TM}^3 , \tag{4.5}$$

where F_{TVACM} is magnetic force between two vertically aligned cylindrical magnets, d_{TM} is the distance between two magnets, A_{TM} , B_{TM} , C_{TM} and D_{TM} are coefficients, 24.191, 16.440, 5.769 and 0.760, respectively.

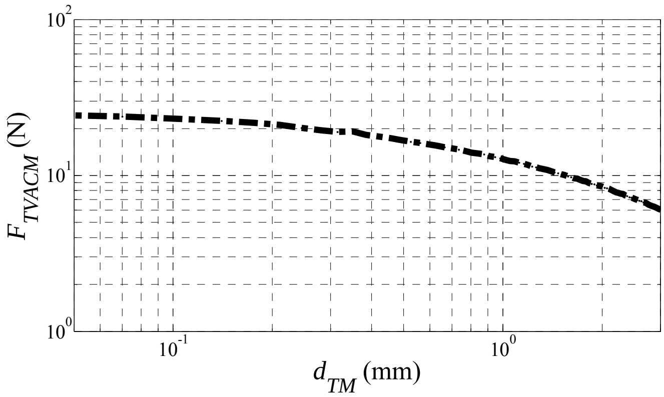

Figure 4.4: Force vs. distance diagrams of two attractive magnets basing on FEMM.

Figure 4.5 shows a simplified model of N1 in which two doubly clamped beams and three magnets are considered. Therefore, the attractive force F_{TVACM1} between the magnets, MAG1 and MAG2 shown in Fig. 4.5, is

$$F_{TVACM1} = A_{TM} - B_{TM} d_{TM1} + C_{TM} d_{TM1}^{2} - D_{TM} d_{TM1}^{3}, \tag{4.6}$$

And the attractive force F_{TVACM2} between the magnets, MAG2 and MAG3 also shown in Fig. 4.5, is

$$F_{TVACM1} = A_{TM} - B_{TM} d_{TM2} + C_{TM} d_{TM2}^{2} - D_{TM} d_{TM3}^{3}, \tag{4.7}$$

in which d_{TM1} and d_{TM2} are

$$d_{TM1} = d_{I4} - z, \tag{4.8}$$

and

$$d_{TM2} = d_{I4} + z, \tag{4.9}$$

where d_{I4} is the distance between magnets when the simplified model of N1 is at rest, which is restricted by $2\ mm \le d_{I4} \le 15\ mm$ because of the prospective displacement and the constraint of the volume of the design.

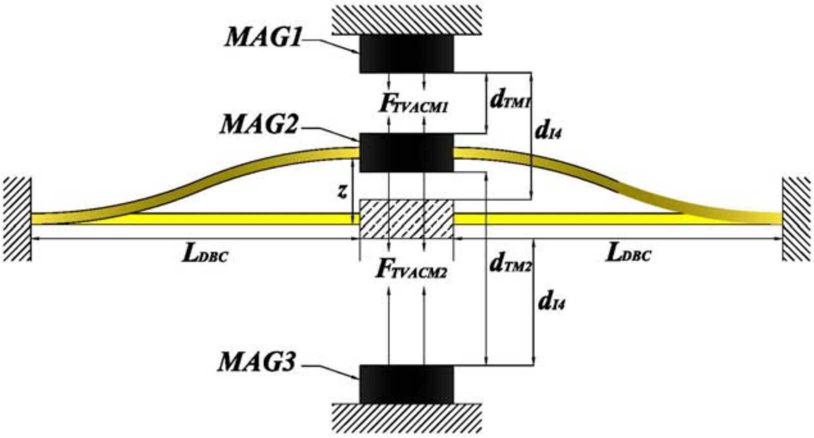

Figure 4.5: The simplified model of N1.

Furthermore, the resultant force of the MAG1, MAG2 and MAG3 can be expressed as

$$F_{\mathrm{IM}} = F_{TVACM1} - F_{TVACM2}. \tag{4.10}$$

Substituting Eqs. (4.6) – (4.9) into Eq. (4.10) and rearranging terms yield

$$\begin{aligned} F_{IM} &= A_{TM} - B_{TM}\left(d_{\mathrm{I4}} - z\right) + C_{TM}\left(d_{\mathrm{I4}} - z\right)^2 - D_{TM}\left(d_{\mathrm{I4}} - z\right)^3 \\ &\quad -\left[A_{TM} - B_{TM}\left(d_{\mathrm{I4}} + z\right) + C_{TM}\left(d_{\mathrm{I4}} + z\right)^2 - D_{TM}\left(d_{\mathrm{I4}} + z\right)^3\right] \end{aligned} \tag{4.11}$$

Rearranging terms yield

$$\begin{aligned} F_{\mathrm{IM}} &= 2B_{TM}z - 4C_{TM}d_{\mathrm{I4}}z + D_{TM}\left(6d_{\mathrm{I4}}^2 z + 2z^3\right) \\ &= z\left(2B_{TM} - 4C_{TM}d_{\mathrm{I4}} + 6D_{TM}d_{\mathrm{I4}}^2\right) + 2D_{TM}z^3, \end{aligned} \tag{4.12}$$

in which

$$2B_{TM} - 4C_{TM}d_{\mathrm{I4}} + 6D_{TM}d_{\mathrm{I4}}^2 > 0, \tag{4.13}$$

and

$$2D_{TM} > 0, \tag{4.14}$$

Because $2\ \mathrm{mm} \le d_{\mathrm{I4}} \le 15\ \mathrm{mm}$ and B_{TM}, C_{TM} and D_{TM} are 16.440, 5.769 and 0.760, respectively .

Hence, the resultant force of the doubly clamped beams and magnets can be obtained by

$$\begin{aligned} F_{\mathrm{RES}} &= 2F_{EDCB} - F_{\mathrm{IM}} \\ &= \left(\frac{24E_b I_{DCB}}{L_{DCB}^3} - 2B_{TM} + 4C_{TM}d_{\mathrm{I4}} - 6D_{TM}d_{\mathrm{I4}}^2\right)z + \left(\frac{A_{DCB}E_b\pi^2}{8L_{DCB}^3} - 2D_{TM}\right)z^3, \end{aligned} \tag{4.15}$$

which provides the evidence that the continuous changing attractive magnetic force can decrease overall stiffness of N1, including stiffness of the linear term and the non-linear term.

Restoring Force and Stiffness of N1

Based on Eq. (4.4) and the fitting formula generated by SPSS Statics, the resultant force exerted on the lumped mass due to the restoring force of the beams and the attractive force of the magnets were obtained. The force vs. deflection and stiffness vs. deflection curves of N1 are shown in Fig. 4.6, in which two values, 12 mm and 15 mm, respectively, have been assigned to the height of the columns separating the top and bottom enclosure covers h_{column}, in order to obtain the optimum design. The resulting systems are named $N1_1$ and $N1_2$, respectively.

As shown in Fig. 4.6, $N1_1$ has similar statics behaviors to those of $T3_1$ and $T3_2$ in Chapter 3 which is a typical system with a snap-through mechanism. $N1_2$ shows as a system with a hardening mechanism. Comparing with $N1_2$, $N1_1$ has a lower restoring force when subjected to an identical deflection (see Fig. 4.6(a)). It is because overall stiffness of $N1_1$ is lower than that of $N1_2$ (see Fig. 4.6(b)). In addition, similar to $T3_1$ and $T3_2$, stiffness of $N1_1$ switches sign from positive to negative. The comparison above indicates that $N1_1$ will demonstrate similar dynamic behaviors to those of $T3_1$ and $T3_2$. The FRC of $N1_1$ will lean to left when the response displacement is lower than the critical point, show unstable chaotic response around the fundamental frequency when the response displacement exceeds the critical point but is lower than the cross point, and lean to the right when the peak displacements around the fundamental frequency crosses the cross point completely. $N1_2$ has no critical and cross point due to uniform positive stiffness. The corresponding displacements of the critical point and cross point of $N1_1$ are given in Table 4.2.

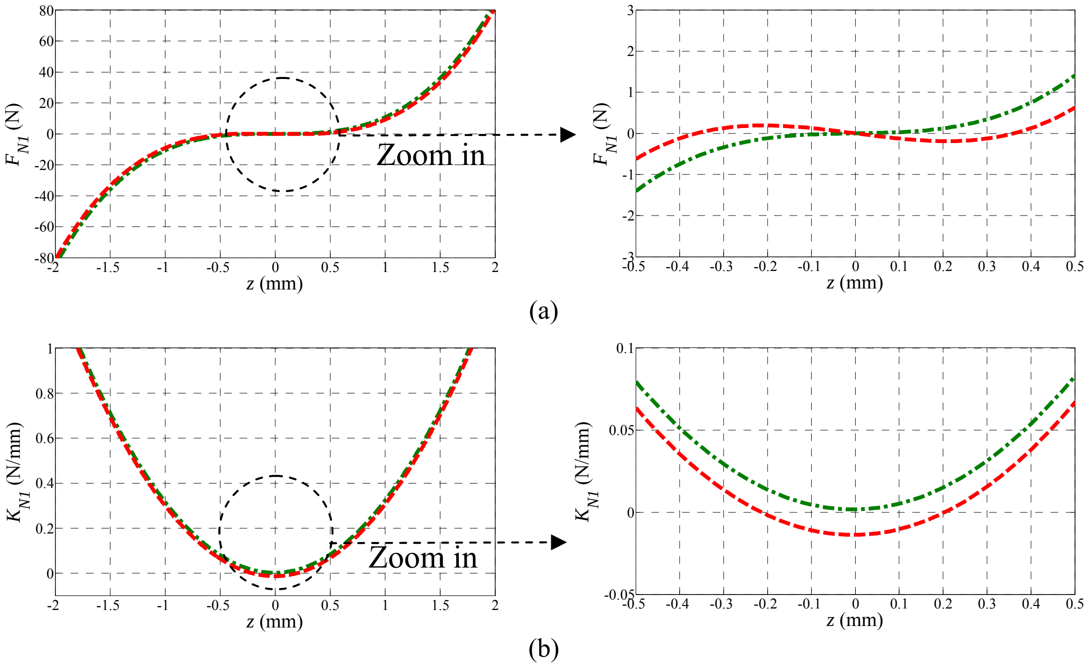

Figure 4.6: (a) Force vs. deflection and (b) stiffness vs. deflection of $N1_1$ (red), and $N1_2$ (green).

Table 4.2: Displacement values of the critical point and cross point of $N1_1$.

Critical point displacement 1 $\lvert z_{N1-CRI-1} \rvert$ (mm)	Critical point displacement 2 $\lvert z_{N1-CRI-2} \rvert$ (mm)	Cross point displacement 1 $\lvert z_{N1-CRO-1} \rvert$ (mm)	Cross point displacement 2 $\lvert z_{N1-CRO-2} \rvert$ (mm)
0.5	0.2	0.7	0

4.1.3 Dynamic Analysis and Experiments

Experimental Apparatus and Procedure

Experiments were conducted to investigate the dynamic behaviors of $N1_1$ and $N1_2$. The prototypes adopted in the experiments were fixed onto an aluminium alloy plate by four bolts. The plate was then connected to the V406 shaker from Bruel & Kjaer UK Limited which was powered by PA100E amplifier. The frequency and amplitude signal inputted into the amplifier were generated by Multi-Instrument 3.2 software package from Virtins Technology through the sound card of a desktop computer. A 355B04 piezoelectric accelerometer from PCB Piezotronics was mounted on the roof of the prototype to measure the acceleration of the driving vibrations. quickDAQ software was used to record the acceleration data acquired by DT9800 Multifunction USB DAQ Modulues from the accelerometer. A Laser interferometric Vibrometer, SP-S LSV from SIOS was fixed on an aluminium alloy base plate which was placed vertically to the top magnet of the prototype. INFAS Vibro Vibrometer Software displayed and recorded the vibration amplitude data through the incremental signal-processing board equipped with vibrometer. The top and bottom cylindrical magnets were replaced by two ring magnets with the diameter $\Phi_R = 15$ mm, the thickness $d_{\mathrm{I3R}} = 2$ mm and the sunk hole diameter $\Phi_r = 3$ mm to allow the laser of the vibrometer to pass through the hole so that the displacement of the lumped mass could be measured. The accelerations of the driving vibration used in these experiments were 1 m/s^2 and 5 m/s^2 with increasing frequencies with a step increment 1 Hz. The entire setup is shown in Fig. 4.7.

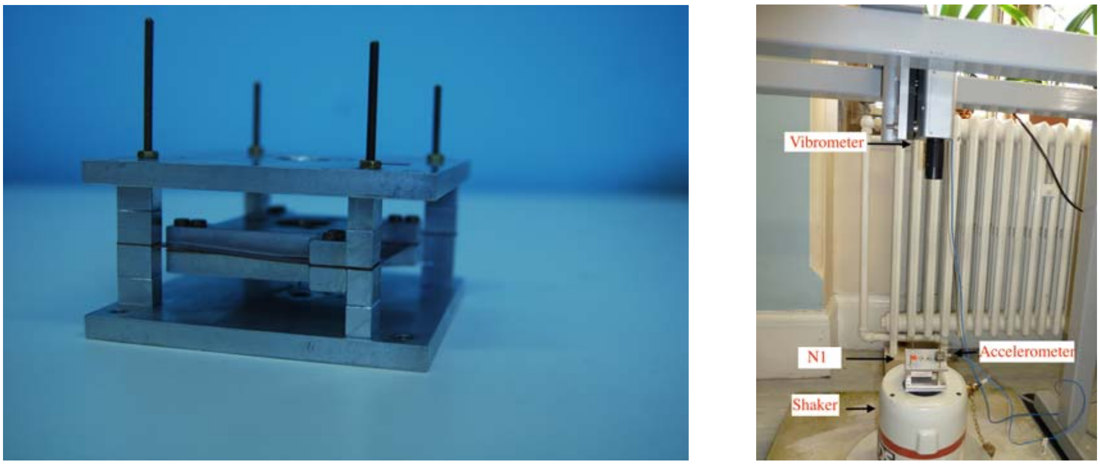

(a) (b)

Figure 4.7: (a) The prototype of N1 and (b) experimental apparatus

Dynamic Analysis

The NS method introduced in Chapter 3 was used to simulate the dynamic responses of $N1_1$ and $N1_2$. To ensure the accuracy of the numerical simulation, the damping ratio of $N1_1$ and $N1_2$ was determined firstly. Several measurements were taken on the prototypes by applying an impulse to the prototypes and measuring the resulting damped harmonic oscillation displacement [17]. The mean value of these measurements was approximately 0.058, which was adopted in the numerical simulation. FRCs of $N1_1$ and $N1_2$ are shown in Fig. 4.7 when subjected to constant acceleration excitations $A_c = 1\ \text{m/s}^2$ and $A_c = 5\ \text{m/s}^2$, respectively.

The approach mentioned in Chapter 3 is used to identify operation bandwidths of $N1_1$ and $N1_2$. To do so, a cantilever beam with an additional mass end which is a typical linear system is considered. The dimensional parameters and physical properties of materials of the cantilever beam are identical to those of the doubly clamped beam in N1. Moreover, the additional mass is equal to a quarter of the lumped mass and magnets inserted in N1. As a result, the natural frequency of the cantilever beam is about 18 Hz. Therefore, the half-power bandwidth is 2.1 Hz by adopting the mean value of damping ratio, 0.058. Furthermore, the displacements when the excitation frequency is 16.95 Hz or 19.05 Hz are 0.19 mm and 0.95 mm when subjected to constant acceleration excitations $A_c = 1\ \text{m/s}^2$ and $A_c = 5\ \text{m/s}^2$, respectively.

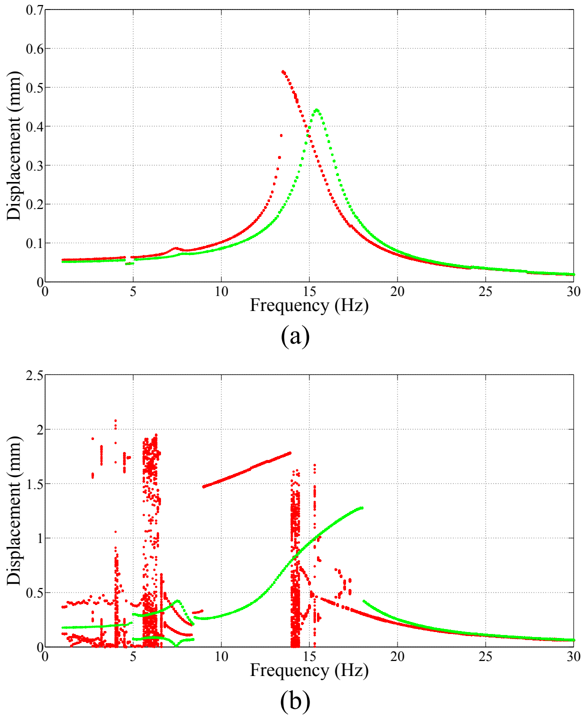

Figure 4.8: FRCs of N1$_1$ (red), and N1$_2$ (green). (a) $A_c = 1$ m/s^2, (b) $A_c = 5$ m/s^2.

$A_c = 1$ m/s^2

Figure 4.8(a) shows that the FRC of N1$_1$ leans to the left in which the inconspicuous unstable chaotic response can be observed around the fundamental frequency. It is because the maximum dynamic displacement exceeds the corresponding displacement of the critical point $\left|z_{N1-CRI\text{-}1}\right| = 0.5$ mm, and is lower than the displacement of the cross point $\left|z_{N1-CRO\text{-}1}\right| = 0.7$ mm. In contrast, the dynamic response of N1$_2$ is similar to that of a linear system due to the fact that the effect of the nonlinearity is insignificant when the displacement is small. The operation bandwidth of N1$_1$ is wider than that of N1$_2$. The operation bandwidth of N1$_1$ is around 4.3 Hz whereas it is 4 Hz for N1$_2$. Additionally, the response displacements of N1$_1$ are higher than those of N1$_2$ due to relatively lower positive stiffness as well as negative. The maximum response displacement reaches 0.54 mm for $N1_1$, comparing with 0.43 mm for $N1_2$.

$\underline{A_c = 5\ \text{m/s}^2}$

As shown in Fig. 4.7(b), a sudden jump-up followed by the right leaning emerges in the FRC of $N1_1$ which indicates that all peak displacements in a cycle of the time-based response around the fundamental frequency overrun the corresponding displacement of the cross point. In addition, significantly unstable chaotic responses can be observed in the frequency ranges of before and after the sudden jump-up. In these frequency ranges, though the maximum displacement in a cycle of the time-based displacement response has exceeded the cross point, most of the peak displacements still stay below the cross point, as discussed in Chapter 3. Therefore, the dynamic response in these frequency ranges is dominated by negative stiffness, which leads to the unstable chaotic response. The FRC of $N1_2$ leans to the right, which behaves essentially like that of a system with a hardening mechanism. The operation bandwidths of $N1_1$ and $N1_2$ further expand due to the right leaning behavior. The operation bandwidth of $N1_1$ is around 6.0 Hz whereas that of $N1_2$ is 4.2 Hz. Furthermore, response displacements of $N1_1$ are still higher than those of $N1_2$. The maximum displacements are 1.78 mm for $N1_1$ and 1.28 mm for $N1_2$. All of these demonstrate that $N1_1$ is superior.

Experimental results and discussion

The data recorded by the INFAS Vibro Vibrometer Software in each frequency was processed to obtain the displacement of the lumped-mass. Comparisons between the experimental data and the simulation data are showed in Fig. 4.9.

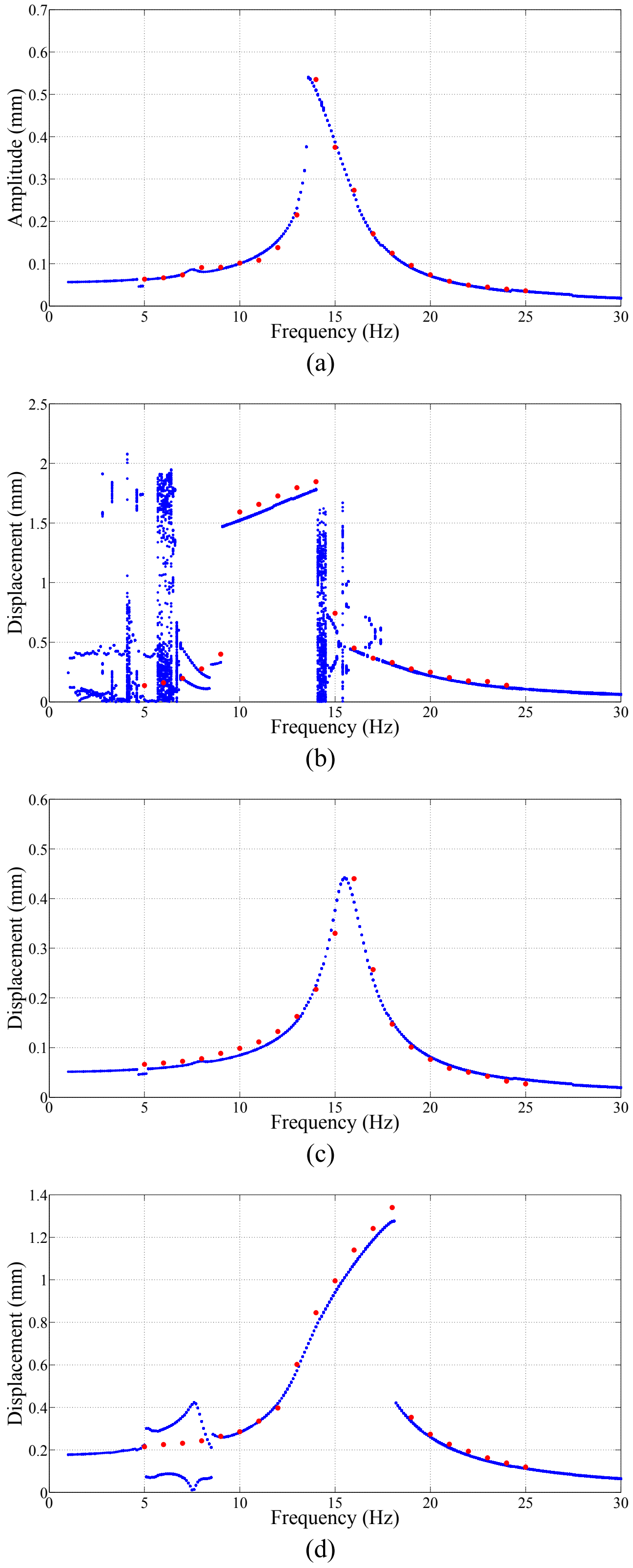

Figure 4.9: FRCs of: (a, b) N1$_1$ and (c, d) N1$_2$, when $A_c = 1$ m/s^2 for a and c, $A_c = 5$ m/s^2 for b and d. Simulation data (blue) and experiment data (red).

The experimental data fits the simulation data of $N1_1$ and $N1_2$ well when $A_c = 1$ m/s^2 (see Figs. 4.9(a) and 4.9(c)). By contrast, differences between the simulation data and the experimental data were observed when $A_c = 5$ m/s^2. Firstly, compared to the FRC generated by the simulation data, no dispersed point could be seen from the FRC of $N1_1$ in accordance with the experimental data (see Fig. 4.9(b)). It was because the laser of the vibrometer had to be focused on the surface of the lumped-mass to read the response displacement. It could not be done properly and rapidly when the lumped-mass had unstable responses. As a result, only average data could be recorded in each frequency. Secondly, due to the twist of the lumped mass, the FRCs of $N1_1$ and $N1_2$ on the basis of the experimental data were higher than those of the simulation data, particularly in the vicinity of the fundamental frequency. Figure 4.10 shows that, when the lumped mass is loaded by a periodic force and starts oscillating in z-direction, the doubly clamped beams of the central shim were subjected to a torque, resulting in a twist of the lumped mass about z-direction and movements in x and y-directions up to the maximum 8×10^{-2} mm. Though the displacement was comparatively small, it caused a decrease in stiffness of $N1_1$ and $N1_2$, leading to an increase in the response displacement. In addition, the input acceleration could not be kept exactly constant during experiments. The true parasitic damping, the real physical dimensions and properties of materials, and fabrication error in the prototypes could not be represented accurately in simulations, all of which could lead to discrepancies.

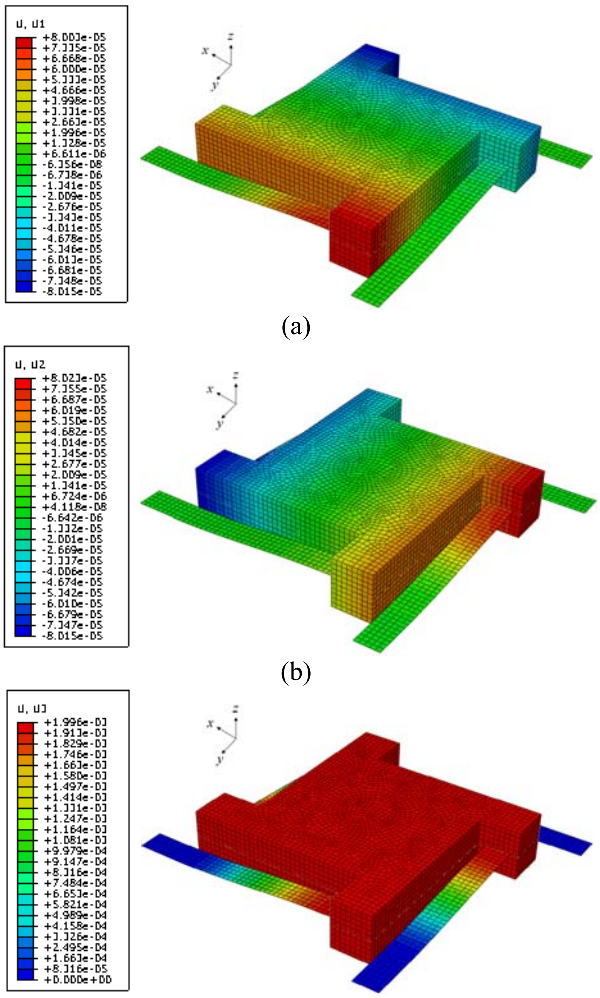

(a)

(b)

(c)

Figure 4.10: Spartial displacement of N1 with $z=2$ mm by Abaqus: (a) x-direction, (b) y-dirction and (c) z-dirction.

4.1.4 Advantages of the Devices and Practical Constraints

Application strengths

Performance of N1_1 shows that a system with a snap through mechanism is superior to systems with hardening or softening mechanisms. The operation bandwidth has been widened. And the response displacement has increased when the excitation is large enough to overcome the energy barrier. Due to the adoption of the magnets, it can avoid the pitfalls of the T3, e.g., buckling of beams when the input force exceeds the critical load. Additionally, the corresponding frequencies of fourth, fifth and sixth modes are much higher than those of the first, second and third modes (see Fig. 4.11). The out-of-plan rocking oscillation in second and third modes which could be induced by lateral excitations can be eliminated by the parasitic damping eventually. Therefore, the first mode can have a much wider off-resonance frequency bandwidth ranging from 29 Hz to 973 Hz.

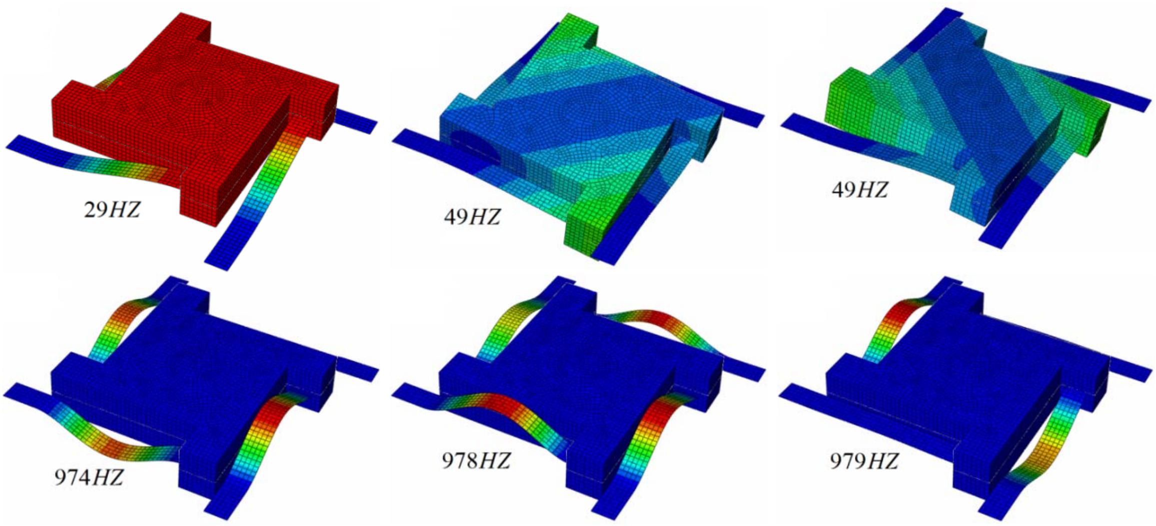

Figure 4.11: First six eigenmodes of N1 free of magnetic force by Abaqus.

Practical constraints

The doubly clamped beams of the central shim could be subjected to a torque when the lumped mass is excited, which makes it difficult to couple N1 with a piezoelectric mechanism. The asymmetric distribution of the strain along the doubly clamped beam could result in a decrease in the electromechanical coupling efficiency of the piezoelectric material as has been reviewed in Section 2.2 [20]. Additionally, some areas of the doubly clamped beam could have relatively high stress due to the torque, which may lead to failure of the piezoelectric material.

4.2 Design II

An improved structural design, namely, N2, is proposed to overcome the drawbacks of N1.

4.2.1 Model

Figure 4.12 shows the 3D model of N2. It has a structural design similar to N1 except that a cross-shaped beryllium copper shim with four identical doubly clamped beams of thickness $d_{\mathrm{II}1} = 0.3$ mm and length $L_{DCB} = 35$ mm is adopted to replace the rectangular shim in N1 (see Fig. 4.13(a)). At the centre, two rectangular aluminum alloy blocks of depth $d_{\mathrm{II}2} = 5$ mm shown in Fig. 4.13(b) are bonded to the beams. In addition, 24 N42 permanent cylindrical magnetic buttons of diameter $\Phi_{\mathrm{II}} = 6$ mm and the thickness $d_{\mathrm{II}3} = 2$ mm are used, 16 of which are fixed into the four corners of the lumped mass. The rest are embedded into the top and bottom of the enclosure, and vertically aligned with the magnets in the lumped mass. Dimensional parameters of the central shim and the alloy block are shown in Fig. 4.13. Physical properties of the materials are the same as those in N1 which are given in Table 4.1.

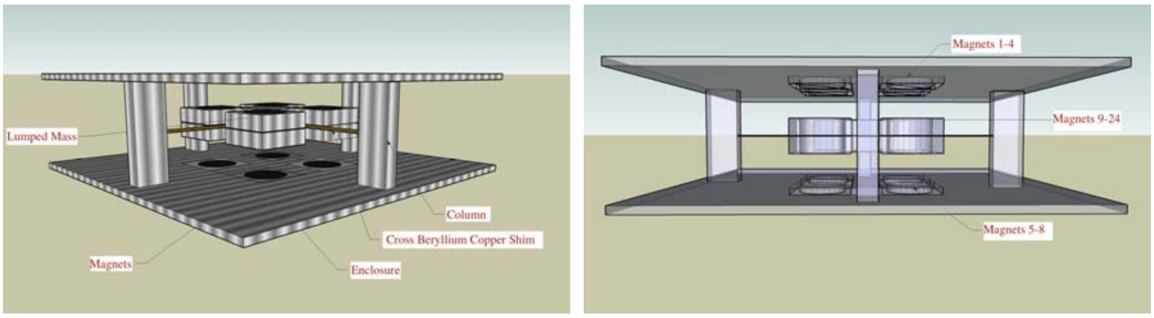

(a) (b)

Figure 4.12: The 3D model of N2: (a) isometric view of N2 and (b) arrangement of magnets.

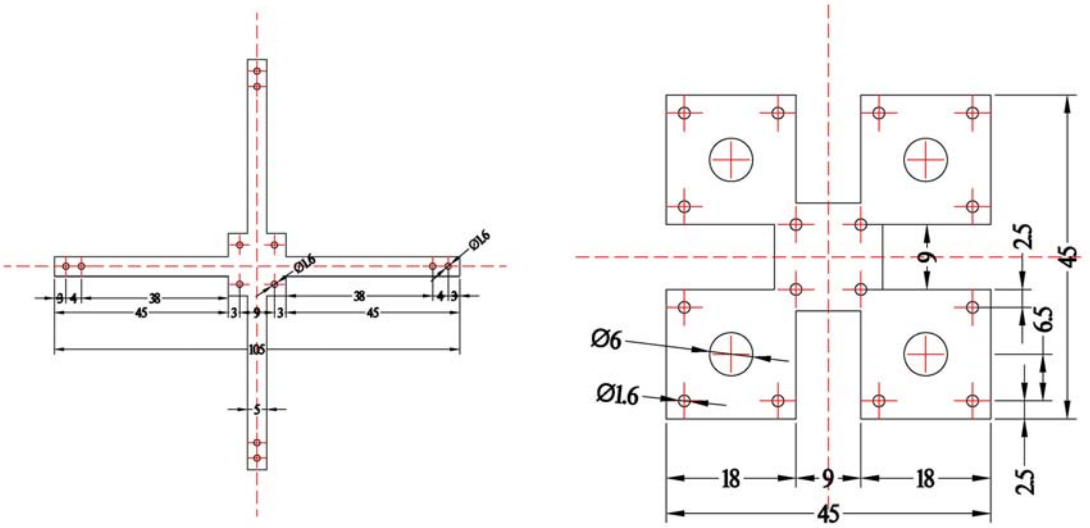

(a) (b)

Figure 4.13: Design of (a) the central shim, and (b) the top and bottom alloy blocks forming the lumped mass in N2. Unit: mm.

4.2.2 The Device

The twist mode vanishes in N2 because the cross beryllium copper shim is used. The piezoelectric transduction mechanism can be readily integrated with N2 to complete a piezoelectric non-linear vibration energy scavenging device, which will be referred as ND hereafter. A PZT-5H piezoelectric ceramic plate, SMPL25W5T15311, supplied by STEMiNC, is bonded to the doubly clamped beam in N2, (see Fig. 4.14). The dimensional parameters and physical and electrical properties are listed in Table 4.3.

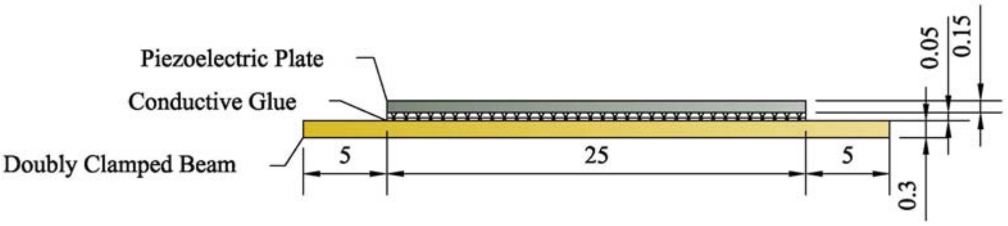

Figure 4.14: Arrangement of the beryllium copper doubly clamped beam, conductive glue and piezoelectric plate. Unit: mm.

Table 4.3: Dimensional parameters and physical and electrical properties of the selected piezoelectric plate

Symbol	Description	Values
l_{piezo}	Length of the piezoelectric plate	25 mm
w_{piezo}	Width of the piezoelectric plate	5 mm
t_{piezo}	Thickness of the piezoelectric plate	0.15 mm
E_{piezo}	Young's modulus of the piezoelectric plate	5.3×10^{10} N/m^2
d_{31}	Strain coefficient of the piezoelectric plate	-270×10^{-12} m/v
k_{31}	Coupling coefficient of the piezoelectric plate	0.38
$\varepsilon_{33}^{T}/\varepsilon_0$	Relative permittivity	3500

4.2.3 Static Analysis

Abaqus FEA 6.7 was adopted to simulate strain on the piezoelectric plate when the lumped mass was subjected various static deflection. The results are displayed in Fig. 4.15. Note that the strain along the piezoelectric plate was symmetry about the median line of the piezoelectric plate. In addition, the central portion of the piezoelectric plate (around 60% of the total length) was uniformly stretched when the deflection reached 2 mm.

Abaqus FEA 6.7 and SPSS Statics were selected to simulate the force vs. deflection and stiffness vs. deflection relationships of ND and the results are shown in Fig. 4.16. ND_1 and ND_2 have the column heights $h_{column}=7$ mm and $h_{column}=12$ mm, respectively. It can be seen that ND_1 has similar static behaviors to those of the system of a snap-through mechanism, while ND_2 is similar to the system of a hardening mechanism. Overall stiffness of ND_1 is lower than that of ND_2 due to the comparatively larger magnetic force, which switches sign from positive to negative. Therefore, we can safely predict that ND_1 and ND_2 will exhibit dynamic behaviors similar to those of $N1_1$ and $N1_2$, respectively. Because $N1_1$ has the greater response displacement and wider resonance frequency bandwidth than those of N1$_2$, ND$_1$ was chosen for further investigation.

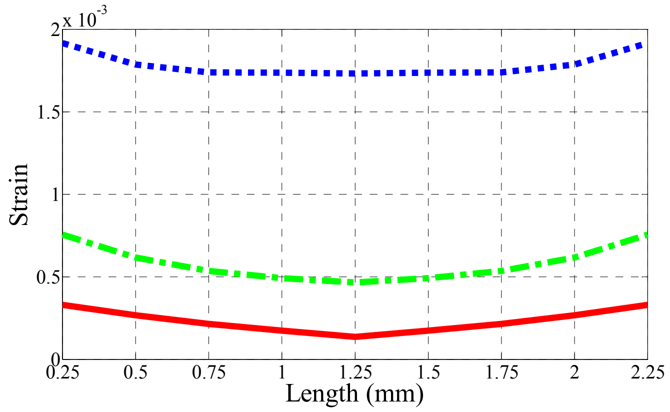

Figure 4.15: Simulations of strain along the piezoelectric plate. $z = 0.5$ mm **(red),** $z = 1$ mm **(green) and** $z = 2$ mm **(blue).**

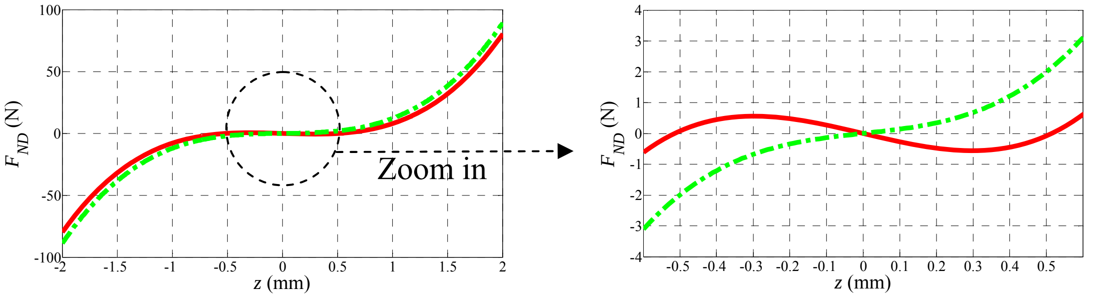

(a)

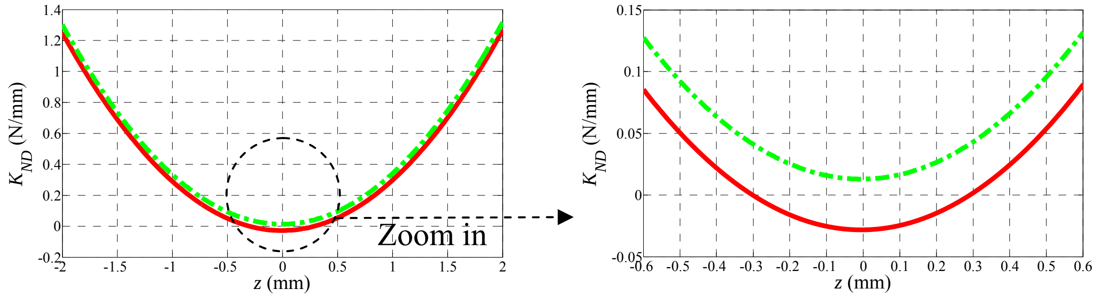

(b)

Figure 4.16: (a) Force vs. deflection and (b) stiffness vs. deflection of ND$_1$ (red) and ND$_2$ (green).

4.2.4 The Coupling Model

An equivalent electrical circuit model of the piezoelectric vibration energy scavenging device was used to estimate the voltage and power generated by ND$_1$ (see Fig. 4.17) [17 and 29]. The model coupled the mechanical system with the piezoelectric transduction mechanism. In the mechanical domain, the through mechanical variable was velocity $\frac{dz}{dt}$. The across mechanical variables were force F_{IN} and F_P. The inertial mass m, the damping coefficient c, and the spring constant (linear and non-linear) $k_{stiffness}\left(z\right)$ were represented as a electrical resistance, inductance and inverse capacitance, respectively. In the electrical domain, the piezoelectric capacitance C_P was explicitly modeled and connected in parallel to an external load resistance R_L.

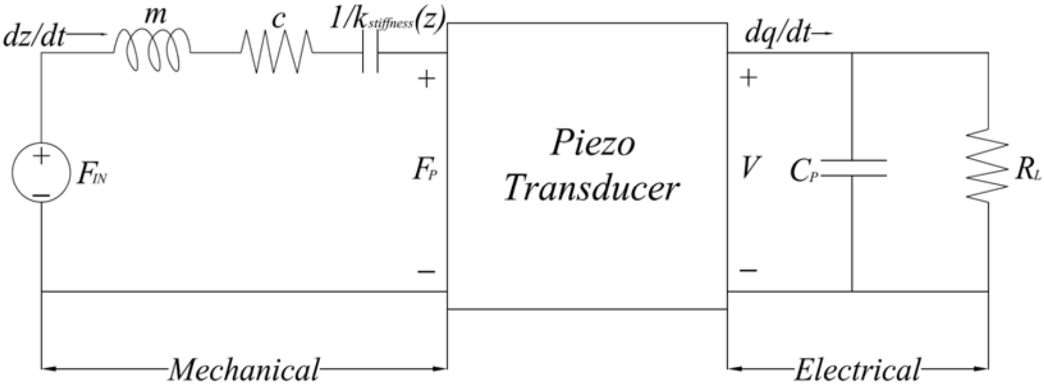

Figure 4.17: Piezoelectric mechanical and electrical domains coupling model.

In comparison with other coupling models [17 and 28], the coupling relationship between the mechanical domain and the electrical domain of the piezoelectric transducer can be successfully captured in this model. The piezoelectric plate when subjected to the mechanical force or stress will generate charge in the piezoelectric capacitor and form electrical voltage across its electrodes. On the other hand, the electrical voltage formed will exert additional mechanical stress which resists the deformation of the piezoelectric plate and restricts the movement of the lumped mass in ND$_1$. Applying Kirchhoff's voltage law to the mechanical domain and Kirchhoff's current law to the electrical domain, the coupled differential equations are

$$m\frac{d^2z}{dt}+c\frac{dz}{dt}+k_{stiffness}\left(z\right)+F_P=F_{IN}, \tag{4.17}$$

and

$$\frac{dq}{dt}-C_P\frac{dV}{dt}-\frac{V}{R_L}=0, \tag{4.18}$$

where $C_P=\frac{n_{piezo}\varepsilon_{33}w_{piezo}l_{piezo}}{t_{piezo}}$ and n_{piezo} is the number of the piezoelectric plate.

It can be noted that Eq. (4.17) is essentially the same as the motion equation of the generic vibration-to-electricity conversion model should except the additional feedback piezoelectric force F_P. F_P represents the backward coupling of the electrical domain to the mechanical domain, which derives from the additional vertical piezoelectric stress formed in response to the presence of the electric field within the piezoelectric capacitance C_P. As has been discussed above, the central portion of the piezoelectric plate in ND$_1$ is uniformly stretched. Therefore the stretched length of a piezoelectric plate can be approximately regarded as the hypotenuse of a triangle whose side is the original length of the plate and end deflection as the orthogonal sides. The additional feedback force F_P is obtained as [29]

$$F_P = 4\frac{5z}{\sqrt{49l_{piezo}^2 + 25z^2}}\sigma_{piezo} w_{piezo} t_{piezo} , \tag{4.19}$$

where $\frac{5z}{\sqrt{49l_{piezo}^2 + 25z^2}}$ is the vertical component factor of the feedback force, and '4' stands for the four piezoelectric plate used in ND_1.

Furthermore, the stress-to-voltage relationship is given by Eq. (2.19) for the piezoelectric plate at zero strain [17]:

$$\sigma_{piezo} = -d_{31} E_3 E_{piezo}, \tag{4.20}$$

and

$$E_3 = \frac{V}{t_{piezo}}. \tag{4.21}$$

Therefore, substituting Eqs. (4.20) and (4.21) into Eq. (4.19), Eq. (4.19) can be rewritten as

$$F_P = \frac{20z}{\sqrt{49l_{piezo}^2 + 25z^2}} w_{piezo} E_{piezo} d_{31} V . \tag{4.22}$$

The current $\frac{dq}{dt}$ in the electrical domain stands for the effect of the piezoelectric charge pump which couples the mechanical domain with the electrical domain [29]. By adopting the electrical displacement-to-stress relationship given by Eq. (2.22) for the piezoelectric plate at zero electric field [17], it can be found that

$$D_3 = d_{31}\sigma_{piezo} = d_{31}\delta_{piezo}E_{piezo}. \tag{4.23}$$

Moreover, the electrical displacement can be related to current using

$$\frac{dq}{dt} = w_{piezo}l_{piezo}\frac{dD_3}{dt}. \tag{4.24}$$

Therefore, substituting Eq. (4.23) into Eq. (4.24) and rearranging terms yields

$$\frac{dq}{dt} = w_{piezo}l_{piezo}E_{piezo}d_{31}\frac{d\delta_{piezo}}{dt} = w_{piezo}l_{piezo}E_{piezo}d_{31}\left(\frac{d\delta_{piezo}}{d\left(\frac{5}{7}z\right)}\frac{d\left(\frac{5}{7}z\right)}{dt}\right). \tag{4.25}$$

The stretched piezoelectric plate length can be approximately considered as the hypotenuse of a triangle with the original length and the deflections the orthogonal sides. Therefore, the strain can be approximated using Pythagoras' Theorem as

$$\delta_{piezo} \doteq \frac{\sqrt{l_{piezo}^2 + \left(\frac{5}{7}z\right)^2} - l_{piezo}}{l_{piezo}}. \tag{4.26}$$

Substituting Eq. (4.26) into Eq. (4.25) yields

$$\frac{dq}{dt} = \frac{25z}{7l_{piezo}\sqrt{49l_{piezo}^2 + 25z^2}}w_{piezo}l_{piezo}E_{piezo}d_{31}\frac{dz}{dt}. \tag{4.27}$$

Now substituting Eqs. (4.22) and (4.27) into Eqs. (4.17) and (4.18), the relationships between the mechanical domain and the electrical domain can be obtained, which are

$$m\frac{d^2z}{dt}+c\frac{dz}{dt}+k_{stiffness}(z)+\frac{20z}{\sqrt{49l_{piezo}^2+25z^2}}w_{piezo}E_{piezo}d_{31}V=-m\ddot{y}, \quad (4.28)$$

and

$$\frac{25z}{7l_{piezo}\sqrt{49l_{piezo}^2+25z^2}}w_{piezo}l_{piezo}E_{piezo}d_{31}\frac{dz}{dt}-C_P\frac{dV}{dt}-\frac{V}{R_L}=0. \quad (4.29)$$

In addition, the voltage generated in the model is an AC voltage. In practical application it will be transferred into a root-mean-square (rms) voltage by the rectifier [46],

$$V_{rms}=\frac{V_{peak}}{\sqrt{2}}, \quad (4.30)$$

where V_{peak} is the peak value of half wave in the AC voltage.

Hence, the rms power transferred to the external resistance load is

$$P_{piezo}=\frac{V_{peak}^2}{2R_L}. \quad (4.31)$$

4.2.5 Dynamic Analysis and Experiments

Experimental apparatus and procedure

A prototype of ND_1 was fabricated. The surfaces of the doubly clamped beams were chemically cleaned upon which the piezoelectric plates were bonded with the conductive glue (see Fig. 4.14). The piezoelectric plates were wired in parallel.

All the setup is identical to that for N1. Additionally, a circuit board was connected with the wired piezoelectric plates, in which variable load resistances could be inserted to find the optimal external load resistance. The NI USB – 6009 was used to read and record the AC voltage across these variable load resistances with the assistance of the LabVIEW 8.0 [47]. The entire setup is shown in Fig. 4.18.

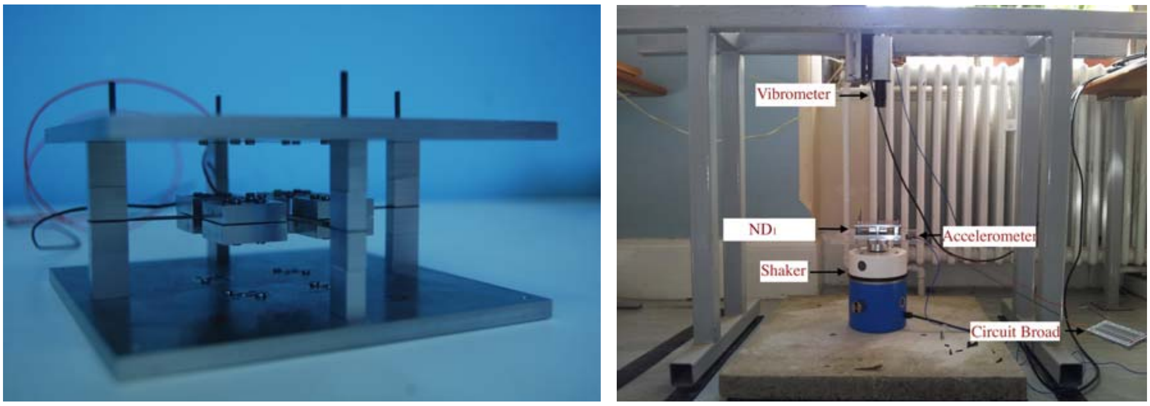

(a) (b)

Figure 4.18: (a) The prototype of ND and (b) experimental apparatus

Dynamic analysis

The NS method was used to simulate the output voltage and power of ND_1 when subjected to constant acceleration and increasing frequencies. To improve the accuracy of the numerical simulation, three coefficients used in the simulation were determined first, i.e., the damping ratio, the effective strain coefficient of the piezoelectric plate, and the external load resistances.

The mechanical damping ratio and effective strain coefficient were experimentally determined. For the mechanical damping ratio, several measurements were taken on the prototype by applying an impulse to the prototype and measuring the resulting damped harmonic voltage oscillation in an open circuit [17]. The mean value of these measurements was near 0.073. For the effective strain coefficient of the piezoelectric plate in Table 6.1, the ideal value of d_{31} is -270×10^{-12} m/v, which was obtained using [17]

$$d_{31}^2 = k_{31}^2\left(s_{11}^E \varepsilon_{33}^T\right), \tag{4.32}$$

in which the ideal electromechanical coupling factor is given as 0.38 (see Table 4.3). As s_{11}^E and ε_{33}^T were constant, d_{31}^2 was linearly proportional to the k_{31}^2. Furthermore, the effective electromechanical coupling factor of ND$_1$ could be determined by measuring the fundamental frequencies in the open circuit ω_{open} and closed circuit ω_{closed} , Eq. (4.33) [49],

$$k_{31-effective}^2 = \frac{\omega_{open}^2 - \omega_{closed}^2}{\omega_{open}^2}. \tag{4.33}$$

Within the open circuit, the NI USB – 6009 was directly connected with the wired piezoelectric plate without the external load resistance. In the closed circuit, the positive and negative terminals of the piezoelectric plates were connected with a 5 Ω load resistance. The Laser interferometric Vibrometer was used to measure the displacement of the lumped mass under these two circuit conditions with increasing frequencies when $A_c = 1$ m/s^2. As a result, the peak frequencies measured in open and closed circuits were approximately 50 Hz and 47 Hz, respectively. Therefore, the effective electromechanical coupling factor was 0.34. Substituting into Eq. (4.32), the effective strain coefficient became -242×10^{-12} m/v.

An external load resistance would be needed to measure ND_1's output against the load as outlined previously. An optimal load resistance, which can maximize the power transfer, can be determined by,

$$R_{opt} = \frac{1}{C_p \omega} \frac{2\varsigma}{\sqrt{4\varsigma^2 + k_{31-effective}^4}}. \tag{4.34}$$

To simplify the simulation and experiments procedures, the frequency of the maximum voltage could be reasonably considered as that of the maximum power harvested [50]. Therefore, to find the corresponding frequency of the maximum voltage and validate ND_1 in the meantime, the dynamic behaviors of the device with increasing accelerations was simulated using the NS method with the damping ratio and effective strain coefficient determined above. The load resistance of 10 kΩ was firstly selected to be the load resistance because it provided a voltage drop large enough to be read by the NI USB – 6009, and has little effect on the dynamic behaviors of ND_1.

$\underline{A_c = 1 \text{ m/s}^2}$

It was found that the FRC of ND_1 leaned to the left (see Fig. 4.19(a)). When the excitation frequency was lower than the fundamental frequency, the dynamic response was stable due to the fact that the maximum displacement was lower than that of the critical point. Furthermore, insignificant unstable responses could be observed around the fundamental frequency. It indicated that the maximum dynamic displacement exceeded the corresponding displacement of the critical point but was lower than the displacement of the cross point. With the further increase in the excitation frequency, the voltage output became stable again with the decrease in the dynamic response.

$A_c = 5\ \mathrm{m/s^2}$

ND_1 exhibited significantly unstable chaotic responses when the excitation frequencies were close to the fundamental frequency, see Fig. 4.19(b). This is due to the fact that the maximum displacements of ND_1 were larger than the corresponding displacements of the critical points but are smaller than those of the cross points. With the increase in the excitation frequency, the dynamic response would become comparatively stable because of the decreasing displacements.

$A_c = 9\ \mathrm{m/s^2}$

The FRC of ND_1 leaned to the right due to the fact that the input acceleration was large enough to ensure the device overcome the Stage I potential energy wells. In addition, significantly unstable chaotic responses can be observed in the frequency ranges after the right leaning. As discussed in Section 3.2.2, in these frequency ranges, most of the peak displacements still stay below the cross point, though the maximum displacement in a cycle of the time-based displacement response exceeded the cross point. Therefore, the dynamic response in these frequency ranges is dominated by negative stiffness, resulting in the unstable chaotic response, which would be stable when the excitation frequency is far from the fundamental frequency.

The analysis has shown that the dynamic behaviors of ND_1 are typical of a system with a snap-through mechanism. Because the FRC of ND_1 demonstrates significantly unstable chaotic response around the fundamental frequency when $A_c = 5\ \mathrm{m/s^2}$, it is difficult to identify the true maximum voltage output. Therefore, the accelerations of the driving vibration used in the experiments were selected as $A_c = 1$ m/s^2 and $A_c = 9$ m/s^2 with a step increment 1 Hz. The effect of the unstable chaotic response on the vibration energy scavenging demands further investigations in the future.

The peak frequencies when $A_c = 1$ m/s^2 and $A_c = 9$ m/s^2 are approximately 45 Hz and 43 Hz, respectively. According to [50], with the change of the load resistance, the peak frequencies could move insignificantly, i.e., 1 to 2 Hz, which has been validated by the numerical simulation. Therefore, 45 Hz and 43 Hz are considered as the frequency where the maximum voltage will be generated, and are substituted into Eq. (4.39). The corresponding optimal load resistances when $A_c = 1$ m/s^2 and $A_c = 9$ m/s^2 are 34 kΩ and 36 kΩ, respectively. In addition, load resistances in the vicinity of these optimal load resistances were chosen from 10 kΩ to 60 kΩ with an interval of 5 kΩ for experiments.

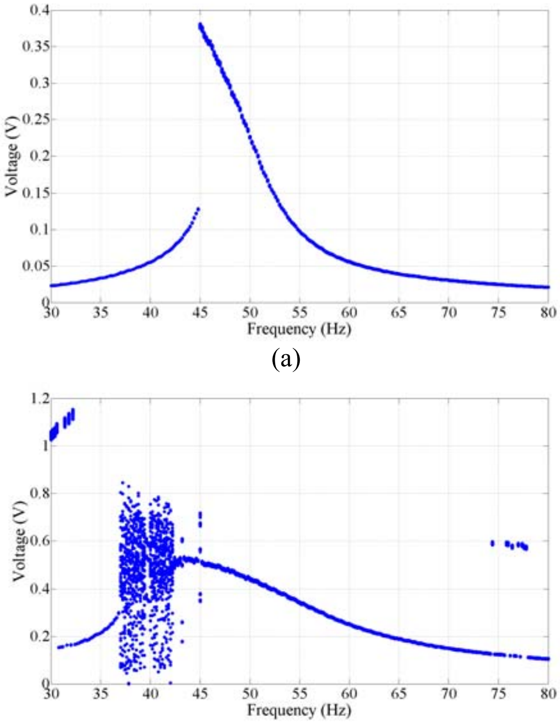

(a)

(b)

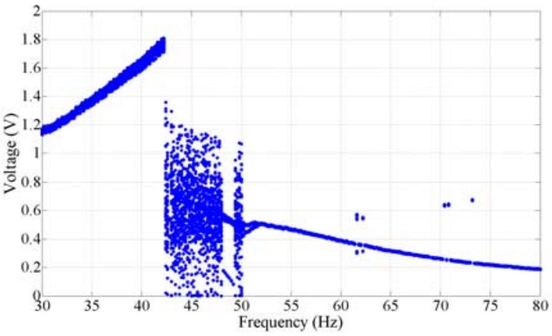

(c)

Figure 4.19: Voltage vs. frequency of ND$_1$: (a) $A_c = 1$ m/s^2, (b) $A_c = 5$ m/s^2 and (c) $A_c = 9$ m/s^2.

Results and discussions

The data recorded by the LabVIEW in 45 Hz and 43 Hz when subjected $A_c = 1$ m/s^2 and $A_c = 9$ m/s^2, respectively, was processed to obtain AC voltage across various load resistances. Comparisons between the experimental data and the simulation data are given in Fig. 4.20.

As it can be seen from Fig. 4.20, the experiment data fits well with the simulation data well, particularly the relationship between voltage and resistance. ND$_1$ can generate up to 2.85 volts and 200 microWatts (see Fig. 4.20(d)), which is large enough to power an existing wireless sensor with the proper circuit design.

However, some mismatches between the experimental and simulation data have also been observed, especially in the vicinity of the optimal load resistance (see Figs. 4.20 (b) and (d)). Explanations for these discrepancies are as follows:

- The input acceleration could not be kept exactly constant during experiments.
- The data read and recorded by the NI USB – 6009 and the LabVIEW 8.0 might not be fully accurate due to the precision of the equipments.

- The mechanical damping ratio and the electromechanical coupling factor used in the simulation were the mean values of several measurements. Therefore, there might be small discrepancies.
- The properties of materials, the bonding method between the doubly clamped beam and piezoelectric plate, the electric conductivity of the glue and doubly clamped beam, the extra load resistances introduced by the electric wires and bonding points, and fabrication errors in the prototypes could not be represented accurately in numerical simulations.

Furthermore, the optimal load resistance when $A_c = 9\ \text{m/s}^2$ is about $1.75\ \text{k}\Omega$, Fig. 4.20(d), which is different from the predicated value of $3.6\ \text{k}\Omega$. Therefore, the corresponding peak frequency will be approximately 88 Hz based on the Eq. (4.33). In Section 3.1.4, we mentioned that FRCs of non-linear systems may follow the upper curve or the lower curve, depending on the initial conditions. In the numerical simulation and experiments, however, it was difficult to determine the suitable initial conditions to ensure the FRC follow the upper curve entirely. Therefore, it can be considered that the frequency 88 Hz is the maximum peak frequency in theory. On the other hand, the frequency 43 Hz is the peak frequency when the initial conditions including the initial velocity and displacement are zero, which is the case here.

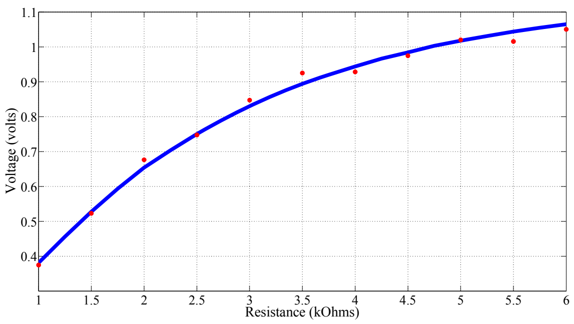

(a)

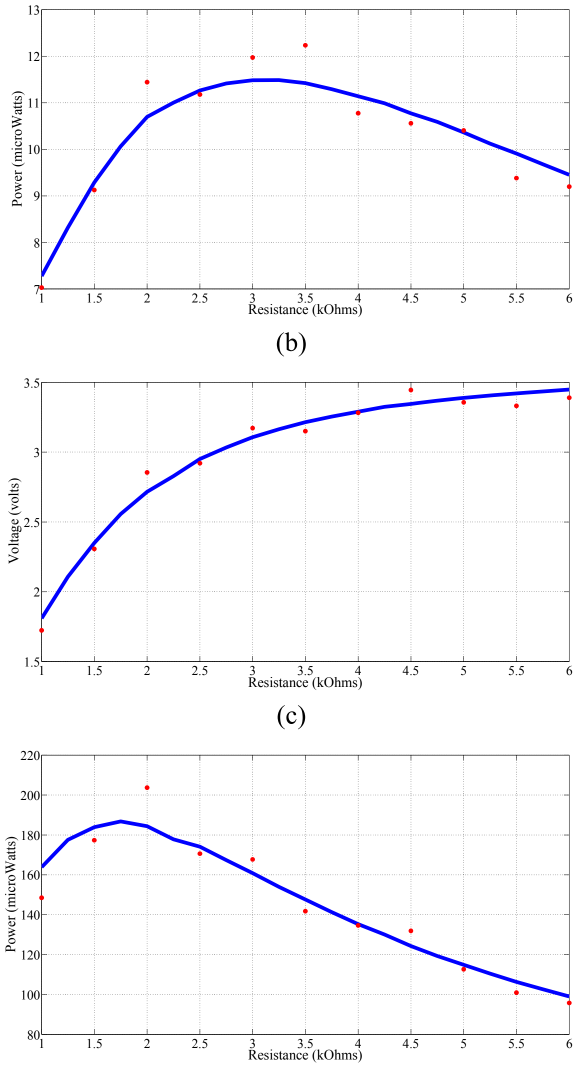

(b)

(c)

(d)

Figure 4.20: Voltage and power output of ND_1 with various load resistances when: (a, b) $A_c = 1\ \mathrm{m/s^2}$ and $\omega = 45\ \mathrm{Hz}$, and (c, d) $A_c = 9\ \mathrm{m/s^2}$ and $\omega = 43\ \mathrm{Hz}$.

4.3 Summary

In this chapter a new mechanical system with a snap-through mechanism N1 was firstly proposed. Two extended models of N1 including $N1_1$ with relatively short columns and $N1_2$ with relatively long columns were considered. Static behaviours of $N1_1$ and $N1_2$ were analyzed. The main findings are as follows:

- $N1_1$ demonstrates similar static behaviors to those of a system with snap-through mechanism.
- $N1_2$ behaves essentially like a system with hardening mechanism.

Subsequently, the dynamic analysis of $N1_1$ and $N1_2$ were carried out when subjected to various constant accelerations and increasing frequencies based on the NS method. The main findings are as follows:

- When the acceleration is relatively small, the FRC of $N1_1$ leans to the left with insignificant unstable chaotic response, which indicates that the maximum displacement in the vicinity of the fundamental frequency exceeds the displacement of the critical point and is lower than that of the cross point. Meanwhile, the FRC of $N1_2$ is similar to that of a linear system due to the insignificant effect of the non-linearity when the displacement is small. In addition, $N1_1$ has a wider bandwidth and higher dynamic responses than those of $N1_2$ due to the lower stiffness.
- With the increase in the acceleration, the FRCs of $N1_1$ and $N1_2$ lean to the right. A sudden jump-up appears in the FRC of $N1_1$ due to the fact that the input acceleration is large enough to ensure the dynamic response of $N1_1$ overcome the Stage I potential energy well. The dynamic responses before and after the jump-up are significantly unstable because most of the peak displacements of $N1_1$ in a cycle of the time-based displacement response stay above the critical point and are lower than the cross point and. Furthermore, $N1_1$ shows advantages in expanding the bandwidth and raising the dynamic displacement over $N1_2$.

The analysis results were validated by experiments. Discrepancies nevertheless could be observed when the acceleration was comparatively large, including:

- When the dynamic response is in chaos, no dispersed point can be recorded by the vibrometer due to its operation limitation.
- The displacements based on the experimental data are higher than those of the simulation data due to the twist of the lumped mass and the decrease in stiffness of $N1_1$ and $N1_2$.

$N1_1$ demonstrates that the system with a snap-through mechanism can overcome the limitation of T3, and has a wider off-resonance frequency bandwidth. However, the design leads to distortion of the lumped mass in vibration, which makes the piezoelectric transduction mechanism unable to be coupled with $N1_1$ efficiently.

As a result an improved structural design N2 has been proposed in which a cross beryllium copper shim is used to replace the rectangular shim in N1. The piezoelectric transduction mechanism can now been effectively coupled with N2 to form a complete piezoelectric non-linear vibration energy scavenging device ND. The simulation analysis for ND shows that the piezoelectric plate can be uniformly stretched when the deflection of the lumped mass is sufficiently large.

Subsequently, two models, namely ND_1 and ND_2, have been statically analyzed. ND_1, which has comparatively short columns, behaves essentially like a system with a snap-through mechanism due to the large attractive magnetic force. Therefore, it has been selected for further investigation. And a piezoelectric mechanical domain and electrical domain coupling model has been used to predict the output voltage and power. The analytical results have been validated by experiments. It has been found that:

- Overall the experimental data matches the numerical data well.
- Some issues have been detected in the experimental data, leading discrepancies between the experimental and simulation data. The reasons could be unstable dynamic responses, the reading and recording errors in equipments, the errors in measurement of the mechanical damping ratio and the electromechanical coupling factor, and the fabrication errors of the prototypes, etc.
- The experimental optimal load resistance is different from the resistance predicated. It is because in the dynamic responses of ND_1 are sensitive to initial conditions but these conditions cannot be guaranteed in experiments.

In summary, ND_1 is a vibration energy scavenging device which could be an alternative design to overcome the drawbacks of existing linear and non-linear vibration energy scavenging devices in certain conditions, e.g., relatively large excitation force required to cross the potential energy barrier and comparatively larger space needed to install the device in comparison with a linear device or a non-linear device with the hardening mechanism with an identical beam of dimensional parameters, etc.

CHAPTER 5 CONCLUSIONS AND FUTURE WORK

5.1 Conclusions

Pervasive networks of wireless sensors and communication nodes have been developed over past decades. Existing powering methods using wiring power and batteries have their own limitations such as expensive setting and high maintenance cost for the former, and limited lifetime for the latter. Technologies that enable a wireless electronic device power itself have been considered as the ideal method to solve the problem, especially the power requirement of the latest wireless sensor has been reduced to below 1 microWatt. The main idea is to integrate the wireless sensor into a device that can harvest energy in ambient environment and convert it into electric power. According to the comparison of the power density of existing self-powered technologies in terms of various ambient energy sources, scavenging technologies of solar energy and vibration energy can meet the power density requirement of existing wireless sensors. This dissertation focuses on developing a novel vibration energy scavenging device to raise the conversion efficiency of the vibration energy.

In this dissertation, existing common vibration sources in ambient environment were reviewed firstly, and then the emphasis was on the vibration energy scavenging devices and their operation vibration range. Subsequently, a generic linear vibration to electricity conversion model, a 2-DOF mass-spring-dampers system, was highlighted based on the analytical method. It has been found that:

- For a vibration energy scavenging device based on a linear mechanical system, the output power can only be maximized when the excitation frequency matches the natural frequency of the device. It falls dramatically when the excitation frequency does not coincide with the natural frequency. Moreover, the output power is inversely proportional to the natural frequency.
- The output power can be optimized when the mechanical damping ratio is equal to the electrically induced damping ratio. In addition, the output is linearly proportional to mass.

Three transduction mechanisms, the electromagnetic, electrostatic and piezoelectric can be used to harvest electrical energy from motions within the vibration energy scavenging device. After reviewing the primary advantages and disadvantages of existing transduction mechanisms, it is decided that the piezoelectric transduction mechanism will be chosen as the primary transduction mechanism for the subsequent design.

In general, the excitation frequencies of vibration sources cannot be predicated correctly, which limits the amount of energy that can be harvested by a linear piezoelectric vibration energy scavenging device. Some improvements have been proposed in the past including altering natural frequencies of linear mechanical systems and adopting non-linear mechanical systems. However, each of them has its own drawback, e.g., external power needed to tune the natural frequency of a linear mechanical system, and comparatively low output displacement of a non-linear mechanical system currently used. To improve that, a detailed analysis of some of the non-linear mechanisms is carried out in Chapter 3.

Three non-linear mechanisms are extensively examined in Chapter 3 in order to identify a suitable one for the design of mechanical systems. The hardening and softening mechanisms are firstly analysed statically and dynamically based on the corresponding typical mechanical systems. The main findings are as follows:

- The FRCs of the systems with hardening and softening mechanisms lean to the right and left of the linear resonance frequency, respectively, which indicate that either of them could have broader the operation bandwidths than the half-power bandwidth of a linear system in an identical vibration source.
- The maximum response displacements of both systems increase with the decrease in the damping ratio because less input energy is consumed by damping.
- The response displacement of the systems with a hardening mechanism becomes smaller with the raise of the non-linear spring constant because of the increase in overall stiffness, whereas becomes larger for the systems with a softening mechanism because of the decrease in overall stiffness.

It has been found that the system with a softening mechanism has higher response displacements and a wider operation bandwidth due to comparatively low stiffness. However, it becomes extremely unstable when the response displacements exceed the maximum displacement allowed.

To overcome the drawbacks of hardening and softening mechanisms, a snap-through mechanism has been looked into. The following has been found through both static and dynamic analysis.

- Overall stiffness switches signs from positive to negative when the deflection exceeds the critical point.
- Two potential energy wells exist in the potential energy vs. deflection curves in which three equilibrium points, four critical points and three cross points are embedded.
- Dynamically when the forcing amplitude is small, the FRC of the system leans to the left of the linear resonance frequency, and is stable. This makes it identical to that of a system with a softening mechanism due to the fact that the maximum dynamic response displacement of the system is smaller than the corresponding displacement of the critical point.
- With the increase in the forcing amplitude, the FRCs of the system becomes unstable, particularly around the fundamental frequency, indicating that the dynamic response of the system has exceeded the critical point but stays below the cross point.
- A jump-up phenomenon emerges from the right leaning FRC of the system when the forcing amplitude is large enough to allow the system to overcome the Stage I potential energy well and oscillate about the middle equilibrium point periodically.
- The increasing damping ratio can restrict the dynamic response of the system, leading the decrease in the dynamic displacements and relieving the chaotic response.

Despite that the system with a snap-through mechanism is advantageous over other systems, it cannot be easily coupled with existing transduction mechanisms. Hence, we have embarked on new designs in Chapter 4.

The first mechanical structure N1 consists of a rectangular beryllium copper shim bonded by two aluminium alloy blocks forming a lumped mass. The mass is connected to the enclosure through four beams. A suitable selection of materials and sectional geometries of the beams allows a tension dominated the force-deflection behaviour for these doubly clamped beams. Additionally six permanent cylindrical magnetic buttons are used in the design to alter stiffness of the system. The attractive force generated by these magnets can effectively reduce overall stiffness of the system. When a suitable distance between the magnets is chosen, N1 exhibits similar behaviours to those of a system with a snap-through mechanism. However, it has been found that the dynamic response displacements on the basis of experimental data were higher than simulation data, particularly in the vicinity of the fundamental frequency. It is because the doubly clamped beams are subjected to a torque when the lumped mass is loaded by a periodic force and starts oscillating in z-direction, resulting a twist of the lumped mass which causes the decrease in stiffness of N1.

In view of this fact, an improved design N2 with a cross beryllium copper shim has been proposed. The piezoelectric transduction mechanism can be effectively coupled with N2 to form a complete piezoelectric non-linear vibration energy scavenging device ND. By numerical simulation and experiments, we are able to show that ND with a snap-through mechanism can generate enough voltage and power to power existing wireless sensors with a proper circuit design, and has wider operational bandwidth in comparison with a linear device, such as, a cantilever beam, with identical dimensional parameters and physical properties. Therefore, ND with a snap-through mechanism can be considered as an alternative design to overcome the drawbacks of existing linear and non-linear vibration generators, when the excitation force is large enough to ensure the dynamic response of ND overcome the potential energy barrier. Furthermore, due to the existence of the frame, the volume of ND is relatively larger than a linear vibration energy scavenging device based on a cantilever beam, or a non-linear vibration energy scavenging device based on a fixed-fixed beam, with an identical beam of dimensional parameters.

5.2 Future Work

5.2.1 Investigations of the Effect of the Chaotic Response on Vibration Energy Scavenging

Unstable chaotic responses can be observed in FRCs of s non-linear system with a snap-through mechanism. Therefore, the effect of the chaotic response on the vibration energy harvesting needs to be investigated by using the NS method and experiments. Firstly, it is known that the dynamic behaviour of a non-linear system with a snap-through mechanism is highly sensitive to initial conditions, e.g., initial velocity and acceleration. Therefore, the Monte Carlo method will be used to study the effects of various initial conditions on chaotic responses. Secondly, the experimental data in periodic stable responses will be compared with that in chaotic responses to investigate the effect of the chaotic response on the vibration energy harvesting. If the amount of energy harvested in chaotic responses is lower than that in periodic responses in the same period and frequency range, it is necessary to find a way to avoid chaotic regions, possibly by increasing damping ratio or by changing nonlinearities of non-linear systems, etc.

5.2.2 Physical Modeling and Experiments

The fabrication process of ND_1 will be further developed with the assistance of the MEMS technology. The method of coupling the MEMS technology with the magnetization material will be investigated. Furthermore, on the basis of more testing results in the laboratory, the device will be installed on a real structure to validate the workability of ND_1.

5.2.3 Optimizations

Based on the experimental results, appropriate adjustments for ND_1 will be made to optimize the energy harvesting function, e.g., the geometric size, the electrical circuit and the transduction mechanism. Furthermore, a three-dimensional mechanical structural design which contains the key dynamic characteristics of ND_1 and is capable of capturing vibrations in all directions will be explored.

REFERENCE

[1] Roundy, S. J., (2003). *Energy Scavenging for Wireless Sensor Nodes with a Focus on Vibration to Electricity Conversion*. PhD dissertation, The University of California, Berkeley.

[2] Rabacy, J. M., Ammer, J., da Silva, J. L., Patel, D., and Roundy, S. J., (2000). PicoRadio Supports Ad Hoc Ultra-Low Power Wireless Networking. *IEEE computer*, Vol. 33, No. 7, pp. 42-48.

[3] Gates, B., (2002). The disappearing computer. *The Economist, Special Issue: The World in 2003*, pp. 99.

[4] Wang, D. E., Arens, T. Webster, and M. Shi, (2002). How the Number and placement of sensors controlling room air distribution system affect energy use and comfort. *International Conference for Enhanced Building Operations*, Richardson, TX.

[5] Hitachi Unveils Smallest RFID Chip. (2003). *RFiD journal*.

[6] Chandrakasan, A., Amirtharajah, Goodman, R. J., and Rabiner, W., (1998). Trends in low power digital signal processing. *Proceedings of the 1998 IEEE International Symposium on Circuits and Systems*, pp. 604-7

[7] Rabaey, J., Ammer, J., Karalar, T., Li, S., Otis, B., Sheets, M., and Tuan, T., (2002). PicoRadios for Wireless Sensor Networks: The Next Challenge in Ultra-Low-Power Design. *Proceedings of the International Solid-State Circuits Conference*, San Francisco, CA.

[8] Shearwood, C., and Yates, R. B., (1997). Development of an electromagnetic micro-generator. *Electronics Letters*, Vol. 33, No. 22, IEE, pp. 1883-4.

[9] Amirtharajah, R., and Chandrakasan, A. P., (1998). Self-Power Signal Processing Using Vibration-Based Power Generation. *IEEE Journal of Solid State Circuits*, Vol. 33, No. 5, pp. 687-695.

[10] Meninger, S., Mur-Miranda, J., Lang, J., Chandrakasan, A., Slocum, A., Schmidt, M., and Amirtharajah, R., (2001). Vibration to electric energy conversion. *IEEE Trans Very Large Scale Integration (VLSI) Syst.,* 9, pp. 64-76.

[11] Glynne-Jones, P., Beeby, S. P., James, E. P., and White, N. M., (2001). The modeling of a piezoelectric vibration powered generator for microsystems. *Transducers 01/Eurosensors XV.*

[12] Ottman, G. K., Hofmann H. F., and Lesieutre, G. A., (2003). Optimized piezoelectric energy harvesting circuit using step-down converter in discontinuous conduction mode. *IEEE Transactions on Power Electronics*, Vol. 18, No. 2, pp. 696-703.

[13] Williams, C. B., and Yates, R. B., (1996). Analysis of a micro-electric generator for microsystems. *Sensors and Actuators A*, Vol. 52, pp. 8-11.

[14] Beeby, S. P., Tudor, M. J., and White, N. M., (2006). Energy Harvesting vibration sources for Microsystems application. *Measurement Science and Technology*, Vol. 17 No. 1, pp.175-195.

[15] Roundy, S., Wright, P. K., and Rabaey, J., (2003). A Study of Low Level Vibrations as a Power Source for Wireless Sensor Nodes. *Computer Communications*, Vol. 26, No. 11, pp.1131-1144.

[16] Nye, J.F., (1957). *Physical properties of Crystals*. Oxford University Press, Oxford.

[17] Roundy, S., and Wright, P. K., (2004). A piezoelectric vibration based generator for wireless electronics. *Smart Materials and Structures,* Vol. 13, No. 5, pp. 1131-1142.

[18] Gonzalez, J. L., Rubio, A., and Moll, F., (2001). A prospect of the piezoelectric effect to supply power to wearable electronic devices. *Proc. 4th Int. Conf. On Materials Engineering for Resources*, pp. 202-207.

[19] Anton, S. R., and Sodano, H. A., (2007). A review of power harvesting using piezoelectric materials (2003-2006). *Smart Materials and Structures*, Vol. 16, No. 3, pp. 1-21.

[20] Verardi, P., Craciun, F., and Dinescu, M., (1997). Characterization of PZT thin film transducers obtained by pulsed laser deposition. *IEEE Ultrasonics Symposium Proceedings*, Vol. 1, pp. 569-72.

[21] Maluf, N., (2000). *An Introduction to Microelectromechanical Systems Engineering*. Artech House, Inc., Norwood, Massachusetts.

[22] White, N. M., Glynne-Jones, P., and Beeby, S. P., (2001). A novel thick-film piezoelectric micro-generator. *Smart Material Structure,* Vol. 10, pp. 850-852.

[23] Glynne-Jones, P., Beeby, S. P., and White, N. M., (2001). Towards a piezoelectric vibration powered microgenerator. *IEE Proc.-Sci. Meas. Technol.,* Vol. 148, pp. 68-72.

[24] Sodano, H. A., Park, G., and Inman, D. J., (2004). Estimation of electric charge output for piezoelectric energy harvesting. *Strain*, Vol. 40, pp. 49-58.

[25] Li, H., Lal, A., Blanchard, J., and Henderson, D., (2002). Self-reciprocating radioisotope-powered cantilever. *Journal of Applied Physics,* Vol. 92, pp. 1122-1127.

[26] Marzencki, M., Basrour, S., Charlot, B., Grasso, A., Colin, M., and Valbin, L., (2005). Design and fabrication of piezoelectric micro power generators for autonomous microsystems. *Proc. Symp. On Design, Test, Integration and Packaging of MEMS/MOEMS DTIP05,* pp. 299-302.

[27] Leland, E. S., and Wright, P. K., (2006). Resonance tuning of piezoelectric vibration energy scavenging generators using compressive axial preload. *Smart Materials and Structures*, Vol. 15, No. 5, pp. 1413-1420.

[28] Challa, V. R., Prasad, M. G., Shi, Y., and Fisher, F. T., (2008). A vibration energy harvesting device with bidirectional resonance frequency tunability. *Smart Materials and Structures*, Vol. 17, No. 1, pp. 10.

[29] Marinkovic, B., and Koser, H., (2009). Smart Sand-a wide bandwidth vibration energy harvesting platform. *Applied Physics Letter*, Vol. 94, pp. 3.

[30] Chopra, A. K., (2001). *Dynamics of Structures: Theory and Applications to Earthquake Engineering*. Prentice-Hall, 2nd edition.

[31] Ferrari, M., Ferrari, V., Guizzetti, M., Andò, B., Baglio, S., and Trigona, C., (2010). Improved energy harvesting from wideband vibrations by nonlinear piezoelectric converters. *Sensors and Actuators A: Physical*, Vol. 162, No. 2, pp. 425-431.

[32] Barton, D. A. W., Burrow, S. G., and Clare, L. R., (2010). Energy harvesting from vibrations with a nonlinear oscillator. *Journal of Vibration and Acoustics*, Vol. 132, No. 2, pp. 021009.

[33] MATLAB, version 2010b, MathWorks, Natick, Massachusetts, USA.

[34] Szemplinska-Stupnika, W., (1986). Bifurcation of harmonics solution leading to chaotic motion in the softening type Duffing's Oscillator. *International Journal of Non-linear Mechanics*, Vol. 23, No. 4, pp. 257-277.

[35] Thompson, J. M., and Stewart, H. B., (2002). *Nonlinear Dynamics and Chaos*. John Wiley and Sons, Chinchester.

[36] Den Hartog, J. P., (1952). *Advanced Strength of Materials*. McGraw-Hill, New York.

[37] Leieutre, G. A., (2009). How membrane loads influence the modal damping of flexural structures. *AIAA Journal*, Vol. 47, No. 7, pp. 1642-1646.

[38] Ravindra, B., and Mallik, A. K., (1994). Role of nonlinear dissipation in soft Duffing oscillators. *Physical Review E*, Vol. 49, No. 6, pp. 4950-4954.

[39] Thompson, J.M.T., and Hunt, G.W., (1973). *A General Theory of Elastic Stability*. John Wiley&Son, London.

[40] Schmidt, G., and Tondl, A., (1986). *Non-Linear Vibrations*. Cambridge University Press, Cambridge.

[41] Abaqus, Version 6.7, SIMULIA Co., Providence, RI, USA.

[42] Challa, V. R., Prasad, M. G., Shi, Y., and Fisher, F. T., (2008). A vibration energy harvesting device with bidirectional resonance frequency tunability. *Smart Materials and Structures*, Vol. 17, No. 1, pp. 10.

[43] Finite Element Method Magnetics, Version 4.2, Dr. David Meeker, USA.

[44] Vokoun, D., Beleggia, M., Heller, L., and Šittner, P., (2009). Magnetostatic interactions and forces between cylindrical permanent magnets. *Journal of Magnetism and Magnetic Materials*, Vol. 321, No. 22, pp. 3758-3763.

[45] IBM SPSS Statistics, Version 16.0, IBM UK Ltd., Feltham, Middlesex, UK

[46] Lander, C. W., (1994). *Power Electronics*. McGraw-Hill Europe.

[47] NI LabVIEW, Version 8.0, National Instruments Corporation, Austin, Texas, US.

[48] Baker, J., Roundy, S., and Wright, P. K., (2005) Alternative geometries for increasing power density in vibration energy scavenging for wireless sensor networks. *Collection of Technical Papers – 3rd, International Energy Conversion Engineering Conference (2005)*, Vol. 2, pp. 959-970.

[49] Erturk, A., and Inman, D. J., (2011). *Piezoelectric Energy Harvesting*. John Wiley & Sons.

[50] Ramlan, R., (2009). *Effects of non-linear stiffness on performance of an energy harvesting device*, PhD dissertation, University of Southampton.

[51] Paolo, M., (2011). *Explanation in Mathematics*. The Stanford Encyclopedia of Philosophy.